

**STUDIES OF X-RAY AND ELECTRON BEAM EMISSIONS FROM
A LOW ENERGY PLASMA FOCUS**

MUHAMMAD ZUBAIR KHAN

**THESIS SUBMITTED IN FULFILMENT OF THE
REQUIREMENTS FOR THE DEGREE OF DOCTOR OF
PHILOSOPHY OF SCIENCE**

**DEPARTMENT OF PHYSICS
FACULTY OF SCIENCE
UNIVERSITY OF MALAYA
KUALA LUMPUR**

2016

ABSTRACT

The results of the investigation of the radiation emission (X-ray and electron emissions) from a 2.2 kJ plasma focus operated in argon are presented. Experiments were carried out using the University of Malaya-Dense Plasma Focus (UM-DPF2) device operated in argon. The charging voltage was 12 kV and the operating pressure was in the range of 0.7–2.5 mbar. Several diagnostics techniques were employed during the project, namely, high-voltage probe, five-channel PIN diode, Faraday cup, X-ray spectrometer, and scintillator–photomultiplier as detectors. In addition, the Lee model code was used to simulate the plasma focus discharge and the corresponding emission in terms of X-ray yield and electron beam fluence were analysed and compared to the measured results obtained. The main goal of our project is to conduct an in-depth investigation on X-ray emission from the UM-DPF2 device within an optimum pressure range, as well as the electron beam emission in the same pressure range. The X-ray yield, electron temperature, and electron beam fluence of argon plasma at 1.5–2.0 mbar were analysed. The charge and density of the electron beam is high at this pressure range of argon gas. The model is used to compare the results of temporal evolution and characteristics of X-ray yield and electron beam for 1.5–2.0 mbar pressure range of argon gas in the plasma focus device. The pressure 1.7 mbar of argon was found to give maximum X-ray yield and electron beam emission. A reliable low-energy plasma focus device with X-ray emission or electron beam could be used as an electron beam source in various technological fields.

ABSTRAK

Keputusan penyiasatan pancaran radiasi (pancaran sinar-X dan elektron) daripada plasma tumpuan gas argon yang bertenaga 2.2 kJ telah dibentangkan. Eksperimen telah dijalankan dengan menggunakan peranti plasma tumpuan University of Malaya-Dense Plasma Focus (UM-DPF2) yang beroperasi dengan gas argon. Voltan pengecasan yang digunakan ialah 12 kV dan tekanan yang digunakan ialah dalam lingkungan 0.7-2.5 mbar. Beberapa kaedah diagnostik telah digunakan sebagai pengesanan di dalam projek ini, iaitu, prob bervoltan tinggi, diod PIN lima saluran, cawan Faraday, spektrometer sinar-X dan penyinar-fotopengganda. Di samping itu, kod model Lee telah digunakan untuk menghitung hasil keluaran sinar-X dan fluens aluran elektron untuk dibandingkan dengan keputusan yang diukur. Matlamat utama projek ini ialah untuk menjalankan penyiasatan secara mendalam mengenai pancaran aluran elektron dan pancaran sinar-X dari peranti UM-DPF2 dalam julat tekanan yang ditetapkan. Hasil sinar-X, suhu elektron, dan fluens aluran elektron plasma argon pada julat tekanan 1.5-2.0 mbar telah dikaji. Caj dan ketumpatan aluran elektron juga adalah tinggi pada julat tekanan gas argon ini. Model teori juga telah digunakan untuk membandingkan keputusan evolusi masa serta keputusan pencirian hasil sinar-X dan aluran elektron bagi julat tekanan argon 1.5-2.0 mbar untuk peranti plasma tumpuan ini. Tekanan gas argon pada 1.7 mbar telah dikenalpasti sebagai tekanan operasi yang optimum untuk menghasilkan pancaran sinar-X dan aluran elektron bagi peranti tumpuan plasma yang dikaji. Peranti plasma tumpuan plasma bertenaga rendah yang andal dengan pancaran sinar-X atau aluran elektron boleh digunakan sebagai sumber aluran elektron dalam pelbagai bidang teknologi.

ACKNOWLEDGEMENTS

All praise be to Almighty Allah, The most Benevolent and Merciful, The creator of the universe who gave me an opportunity to work on this dissertation.

I have the honour to express my deepest gratitude to my supervisors Professor Dr. Wong Chiow San and Dr. Yap Seong Ling for their keen interest in my research work and constructive suggestions regarding many aspects of the research.

I would also like to thank Head of Department of Physics for providing a favorable atmosphere to conduct research work.

I would like to convey my sincere thanks to Federal Urdu University of Arts, Science & Technology (FUUAST) Islamabad Pakistan for giving me the opportunity to pursue m Ph.D. program. I truly appreciate the strong financial support, namely, Faculty Development Program (FDP) Higher Education Commission (HEC) via FUUAST Islamabad Pakistan, and the Research Grant IPPP for material and equipment purchases.

I also wish to recognize the contribution and camaraderie of the members of the Plasma Technology Research Center group, particularly, Mr. Jasbir Singh, Lim Lian Kuang, and Ngoi Siew Kien, L. H. Lim, Nitturi Naresh Kumar, Tamil Money for their much-valued assistance, technical support, experiences shared and friendship.

My special thanks to my beloved wife for her generous time and dedication. Her love has been invaluable, and her patience in guiding me through the “twisters” of the life matters, together with her permanent moral support is unforgettable. My beloved sons (Muhammad Basam Khan, Muhammad Shehram Khan, and Muhammad Farzam Khan) make my study period beautiful in university with their natural activities and learning new things in Malaysia and Pakistan.

I wish to pay my humble thanks to my mother, brother, sisters, and all other family members for their support and prayers and whose blessings I always enjoyed.

Lastly, words are not enough to pay my deepest regards to my late father (Muhammad Sana Ullah Khan). I think it is all due to his prayers and special interest in my education which brought me to this position where I am today. His encouragement and guidance are unforgettable for me in my life.

Finally, it is my pleasure to thank also all my friends back home and in Malaysia for helping me or for just being with me, in one way or another, in the course of my doctoral pursuit.

MUHAMMAD ZUBAIR KHAN

TABLE OF CONTENTS

	Page
ABSTRACT	ii
ABSTRAK	iii
ACKNOWLEDGEMENTS	iv
TABLE OF CONTENTS	vi
LISTS OF FIGURES	xi
LIST OF TABLES	xv
LIST OF SYMBOLS AND ABBREVIATIONS	xvi
CHAPTER 1 INTRODUCTION	
1.1 Introduction	1
1.2 History of the Plasma Focus	2
1.3 Importance of Plasma Focus Device	3
1.3.1 Basic Plasma Physics	5
1.3.2 Technological Applications	5
1.4 X-ray Emission from Plasma Focus Devices	6
1.5 Other X-ray Sources	7

1.5.1	X-Pinch	7
1.5.2	X-ray Emission from Vacuum Spark	8
1.5.3	X-ray Emission from Z-Pinch	9
1.6	Electron Emission from Plasma Focus Devices	9
1.7	Motivation of the Research	15
1.8	Layout of the Dissertation	16

CHAPTER 2 PLASMA FOCUS DYNAMICS AND RELATED PHENOMENA

2.1	Introduction	17
2.2	Dense Plasma Focus Dynamics	17
2.2.1	Breakdown Phase	20
2.2.2	Axial Acceleration Phase	21
2.2.3	Radial Collapse Phase	23
2.2.3.1	The Compression Phase	25
2.2.3.2	The Quiescent Phase	26
2.2.3.3	The Unstable Phase	27
2.2.3.4	The Decay Phase	27
2.3	X-ray Production	28
2.3.1	Free-Free Transitions	29
2.3.2	Free-Bound Transitions	29

2.3.3	Bound-Bound Transitions	31
2.4	Electron Beam Production	33
2.5	Lee Model on Plasma Focus	38
2.5.1	Evolution Process in Plasma Focus	38
2.5.1.1	The Axial Phase	39
2.5.1.2	The Radial Inward Shock Phase	39
2.5.1.3	The Radial Reflected Shock Phase	41
2.5.1.4	The Slow Compression Phase	41
2.5.2	Electrical Properties and Circuit Equations	42
2.5.2.1	The Axial Phase	42
2.5.2.2	The Radial Phase	44
2.5.3	Plasma Resistance	45
2.5.4	Energy and Temperature of the Plasma in Plasma Focus	46
2.5.4.1	Mechanisms of Energy Transfer into the Plasma and Plasma Tube	46
2.5.4.2	Driving Parameter	48
2.5.4.3	Energy Transfer Process	50
2.5.5	Simulation using UM-DPF2 Parameters	51
2.5.5.1	Numerical Calculation Method	52
2.5.5.2	Parameters for UM-DPF2	53

CHAPTER 3 EXPERIMENTAL SETUP AND DIAGNOSTICS

3.1	Introduction	54
3.2	Setup of the Plasma Focus Device	54
3.3	Parameters of UM-DPF2 Device	54
3.4	Plasma Diagnostic Techniques	59
	3.4.1 High Voltage Probe	59
	3.4.2 Rogowski Coil	62
	3.4.3 The PIN Diode Detector	70
	3.4.4 The X-ray Spectrometer	79
	3.4.5 Faraday cup	83
3.4	Data Acquisition and Analysis System	87

CHAPTER 4 RESULTLS AND DISCUSSIONS

4.1	Introduction	88
4.2	Five channel PIN diode for Radiation Measurement	95
4.3	The X-ray Spectrometer for X-ray Spectrum from Target	104
4.4	Scintillator-Photomultiplier Detector for Hard X-rays	112
4.5	Faraday Cup Design for Electron Emission	116
4.6	Plasma Focus Model (Radiative)-Lee Model	125

4.6.1	X-ray yield with the Lee Model	126
4.6.2	The Electron Beam Fluence Determined by the Lee Model Code	130
CHAPTER 5 CONCLUSIONS AND SUGGESTIONS FOR FUTURE WORKS		
5.1	Conclusions	137
5.2	Suggestions for Future Works	139
REFERENCES		143
APPENDIX		157

LISTS OF FIGURES

Figure 1.1:	Sketch of plasma focus device geometry (a) Mather-type and (b) Filippov-type.	4
Figure 2.1:	Schematic of the Mather-type plasma focus device.	19
Figure 2.2:	Bremsstrahlung radiation.	30
Figure 2.3:	Recombination radiation.	32
Figure 2.4:	Line radiation.	34
Figure 2.5:	Simplified model of the pinch formation phases.	40
Figure 2.6:	Equivalent circuit structure of the plasma focus.	43
Figure 3.1:	Schematic of plasma focus device.	58
Figure 3.2:	Block diagram of the experimental setup.	60
Figure 3.3:	Schematic diagram of a typical high voltage probe.	61
Figure 3.4:	A schematic diagram of the Rogowski coil.	63
Figure 3.5:	Equivalent circuit of the Rogowski coil.	65
Figure 3.6:	Typical short circuit signal (25 mbar Argon discharge).	69
Figure 3.7:	Biasing circuit of the BPX65 PIN diode.	73
Figure 3.8:	Design of five PIN diodes.	74
Figure 3.9:	Transmission curves of 23 μm Aluminized Mylar, 23 μm Aluminized Mylar + (20 μm , 30 μm , 40 μm , and 100 μm) Al foil.	78

Figure 3.10:	Theoretical transmission ratios of X-ray as a function of the aluminum filter thickness for temperature of 1 keV to 10 keV. The transmission ratio of Cu-K _α is also shown.	80
Figure 3.11:	XR100CR Connection Diagram.	84
Figure 3.12:	Schematic of Faraday Cup.	86
Figure 4.1:	Typical Rogowski coil signal with high voltage probe.	90
Figure 4.2:	Typical signals of Rogowski coil, high voltage probe, two X-ray diodes with specific Al foils (20μm, 30μm).	94
Figure 4.3:	Variation of average signal intensity recorded by Al foil (20 μm, 30 μm, 40 μm) versus Argon gas pressure.	96
Figure 4.4:	Variation of total X-ray yield in 4π-geometry versus Argon gas pressure at constant applied voltage 12 kV.	97
Figure 4.5:	Images of the lead target (a) before and (b) after interaction with an electron beam in the plasma focus.	99
Figure 4.6:	Calculated absorption curves of Al foils for X-rays from copper plasma at various temperature and Cu K _α X-rays with Argon gas pressure 1.5 mbar, estimated electron plasma temperature 3 keV.	101
Figure 4.7:	Calculated absorption curves of Al foils for X-rays from copper plasma at various temperature and Cu K _α X-rays with Argon gas pressure 1.7 mbar, estimated electron plasma temperature 7 keV.	102
Figure 4.8:	Calculated absorption curves of Al foils for X-rays from copper plasma at various temperature and Cu K _α X-rays with Argon gas pressure 2.0 mbar, estimated electron plasma temperature 6 keV.	103

- Figure 4.9:** X-ray Spectrometer position at top-on of the system with the target (a) and side-on of the system with a target at an angle of 45 degree (b). 105
- Figure 4.10:** X-ray spectrum: X-ray produced by energetic electron beam target effect at an angle of 45° when the spectrometer is at side-on position with typical high voltage and Rogowski coil signal at pressure 1.7 mbar. 107
- Figure 4.11:** X-ray spectrum: X-ray produced by electron beam target effect when spectrometer is at top-on position with typical high voltage and Rogowski coil signal at pressure 1.7 mbar. 108
- Figure 4.12:** X-ray spectrum: X-ray produced by electron beam target (Copper) effect at an angle of 45° when the spectrometer is at side-on position at pressure 1.7 mbar. 109
- Figure 4.13:** X-ray spectrum: X-ray produced by electron beam target (Indium) effect at an angle of 45° when the spectrometer is at side-on position at pressure 1.7 mbar. 110
- Figure 4.14:** Schematic of Photomultiplier tube (PMT) coupled with scintillator. 113
- Figure 4.15:** Typical signals of PMT-scintillator. 114
- Figure 4.16:** Variation of the total radiation intensity with PMT verses Pressure (mbar). 115
- Figure 4.17:** Schematic of the arrangement of Faraday cup with Photo diode. 119
- Figure 4.18:** Typical energetic electron beam signal with the signals of photo diode, high voltage probe and Rogowski coil (at pressure of 1.7 mbar). 120
- Figure 4.19:** Variation of total electron beam charge versus Argon gas pressure. 123

- Figure 4.20:** Variation of electron beam density versus Argon gas pressure. 124
- Figure 4.21:** Current output at 1.70 mbar (1.27 Torr) with 12 kV measured (dashed line (blue line)) vs computed (smooth line (pink line)) current traces. 127
- Figure 4.22:** Some results of output of code at the end of the fitting process. 128
- Figure 4.23:** Experimental and computed (via the Lee model) Y_{sxr} yield of X-ray emission as functions of the pressure from the Ar-operated UM-DPF2. 131
- Figure 4.24:** Measured and computed number of electron per shot as a function of the pressure from Argon UM-DPF2. 134
- Figure 4.25:** Total electron fluence J / m^2 as a function of the pressure from Argon UM-DPF2. 135

LIST OF TABLES

Table 1.1:	Summarised results of electron beam energy in World Laboratories.	14
Table 3.1:	Design parameters with applied specification of the UM-DPF2 device.	56
Table 3.2:	Experimentally measured parameters of the UM-DPF2 device.	57
Table 3.3:	The typical parameters of the BPX 65 PIN diode.	71
Table 3.4:	An array of five PIN diodes exposed with Al foil + Aluminized Mylar (μm).	76
Table 4.1:	The design/calculated parameters of the UM-DPF2.	89
Table 4.2:	The design parameters of the UM-DPF2 for the electron beam.	92

LIST OF SYMBOLS

μ	-	Permeability of Free Space
a	-	Anode Radius
A	-	Constant
b	-	Cathode Radius
B_0	-	Magnetic Field
C_0	-	Capacitor Bank for Energy Storage
C_s	-	Sound Speed
E	-	Electric Field
E_0	-	Capacitor Bank Energy
E_1	-	Initial State Energy
E_2	-	Final State Energy
E_{cr}	-	Critical Electric Field
E_i	-	Ionization Energy
E_k	-	Kinetic Energy
E_x	-	Excitation Energy
f_c	-	Axial Current Factors
f_{cr}	-	Radial Current Factors
$F_{eb\tau}$	-	Electron beam fluence
f_m	-	Axial Mass Factors
f_{mr}	-	Radial Mass Factors
F_{z1}	-	Axial Force on Plasma Sheath
F_{z2}	-	Radial Force on Plasma Sheath
h	-	Plank's Constant
h_L	-	Leakage Resistance in the Plasma Tube
I	-	Discharge Current
I_p	-	Pinch Current
$J \times B$	-	driving Magnetic force
k	-	Boltzman Constant
keV	-	kilo electron volt

L	-	Plasma Inductance
L_0	-	External (stray) Inductance
L_p	-	Changing Plasma Tube Inductance
L_{p2b}	-	Plasma Slug Inductance
m_i	-	Mass of Atom or Ion
n	-	Particle Density
N	-	Linear Density
n_0	-	Atomic Number Density
n_e	-	Electron Density
n_i	-	Density of the Ions
N_i	-	Plasma Ion Density
P_B	-	Magnetic Pressure
Q_{rad}	-	Radiation energy
r	-	Boundary Radius of Curvature
R_0	-	Circuit Resistance
r_{min}	-	Minimum Pinch Radius
R_p	-	Plasma Resistance
r_p	-	Slug external radius
r_s	-	Slug internal radius
S	-	Driving Parameter
T	-	Plasma Temperature
T_e	-	Electron Temperature
t_p	-	Pinch life-time
t_{p-s}	-	Transmission Time
U	-	Internal Energy
V_0	-	Capacitor Voltage
z	-	Axial Position of Sheath
z_0	-	Anode Length
Z_{eff}	-	Effective Ionic Charge
Z_i	-	Effective Charge

γ	-	Specific Heat Ratio
δ	-	Surface Effect Thickness
η	-	Spitzer Plasma Resistance
ρ	-	Mass Density
τ	-	Confinement Time
v	-	Velocity
χ_n	-	Ionization Potential
ω	-	Statistical weight of the ground state of the ion

LIST OF ABBREVIATIONS

CS	Current Sheath
CZT	Cadmium Zinc Telluride
DPF	Dense Plasma Focus
DPO	Digital Storage Oscilloscope
EINP	Energy Input into Plasma
EM	Electromagnetic
HV	High Voltage
HXR	Hard X-ray
MCA	Multichannel Analyzer
PMT	Photomultiplier Tube
PVC	Polyvinyl Chloride
RC	Rogowski Coil
RTD	Rise Time Discrimination
SXR	Soft X-ray
UM-DPF2	University of Malaya Dense Plasma Focus
UNU/ICTP PFF	United Nations University / International Center for Theoretical Physics Plasma Fusion Facility

CHAPTER 1

INTRODUCTION

1.1 Introduction

The middle of 18th century indicated the birth period of plasma physics, particularly of the dense plasma focus (DPF). DPF is a machine that produces short-lived, hot and dense plasma. DPF is a pulsed plasma producing device that combines the features of an electromagnetic (EM) shock tube and a pinch device. This device is used to compress plasma to form high density, high temperature pinch columns. This high density, high temperature plasma columns present a rich source of various phenomena and radiations. For the past several decades, this device [1] has been a popular research subject because of its capability of dealing with most research problems based on plasma focus. This device was invented by Mather [2] in the early 1960s, as well as independently by Filippov *et al.* [3] in 1964.

The gas discharges in coaxial tubes such as linear Z-pinches in deuterium environment led to the detection of emission of neutron [4]. The intense burst of neutrons was recognized to be accompanied by the emission of X-rays [5]. Obviously, X-ray emission indicated that neutrons did not originate from thermonuclear reactions. Then, considerable effort was expended on the study of other driving phenomena occurring in the discharges, such as radiation emission in the microwave to HXR range, ions and electrons emissions, filaments [6], plasma shock after the pinch [7], jet [8] and, among others.

1.2 History of the Plasma Focus

Plasma focus devices are that belong to the group of dynamic Z-pinches. These devices are highly motivating objects of plasma physics.

The specific features of such configurations are as follows:

- Total discharge current flows through a plasma column.
- Plasma column is compressed by the self-magnetic field.

Bennett discovered the conditions for a quasi-stable structure of a current carrying plasma column with finite temperature in 1934 [9]. Tonks [10] investigated the construction of an arc under its own magnetic field, and presented the term Z-pinch. The term “Z” was defined as a plasma column constricts at the z-axis under the influence of a magnetic field, which is induced by the axial current flowing through the plasma.

There were two plasma focus configurations proposed, that were different in geometries for extensive studies on Z-pinches

- A Filippov type geometry with a large radius and short electrodes, which was proposed by Filippov *et al.* [11] of the Kurchatov Institute.
- A Mather type geometry with a small radius and long electrodes, which was proposed by Mather [2] of the Los Alamos Laboratory.

In early 1960s, for Mather- and Filippov-type devices, an accelerated plasma sheath magnetically compressed into a short-lived (50 ns to 200 ns), comparatively dense ($\sim 10^{-19} / \text{cm}^3$), and hot ($\sim 1 \text{ keV}$) plasma column was revealed independently.

Despite their significantly differing geometries, both geometries have similar aspects and results, as shown in Figure. 1. These geometries are composed of two coaxial electrodes parted by an insulator sleeve.

A wide range of investigations has been done on both types of geometries with stored energies ranging from 0.1 J to 1 MJ [12-17]. Noteworthy interest was motivated to plasma focus because of its high $n\tau$ value of the plasma (where n = particle density and τ = confinement time). In addition, the intense burst of neutrons from the plasma focus device that operated in deuterium was believed to be possible results of thermonuclear fusion.

Being a primary source of hot and dense plasma (~ 1 keV), the focus also emits numerous amounts of SXR and HXR, ions, and electrons, especially operated with high-Z gases. This unique feature of the plasma focus distinguishes it from other devices as a major applicant for industrial applications.

In summary, a vast variety of plasma phenomena is readily available from this simply fashioned device, which has managed to its wide-ranging studies in numerous laboratories globally.

1.3 Importance of Plasma Focus Device

The plasma focus device, particularly the low energy type, is compelling devices for the study of basic physics, as well as for potential applications in various industrial fields. Given its abundance of different radiations, the device has drawn the attention of the scientific community since its start. Researchers exert considerable effort to understand the formation of plasma dynamics in this device to be able to identify its appropriate applications in fields ranging from fusion to electronics industries. Decker *et al.* [18] and Moreno *et al.* [19] reported detailed assessments on various aspects of basic.

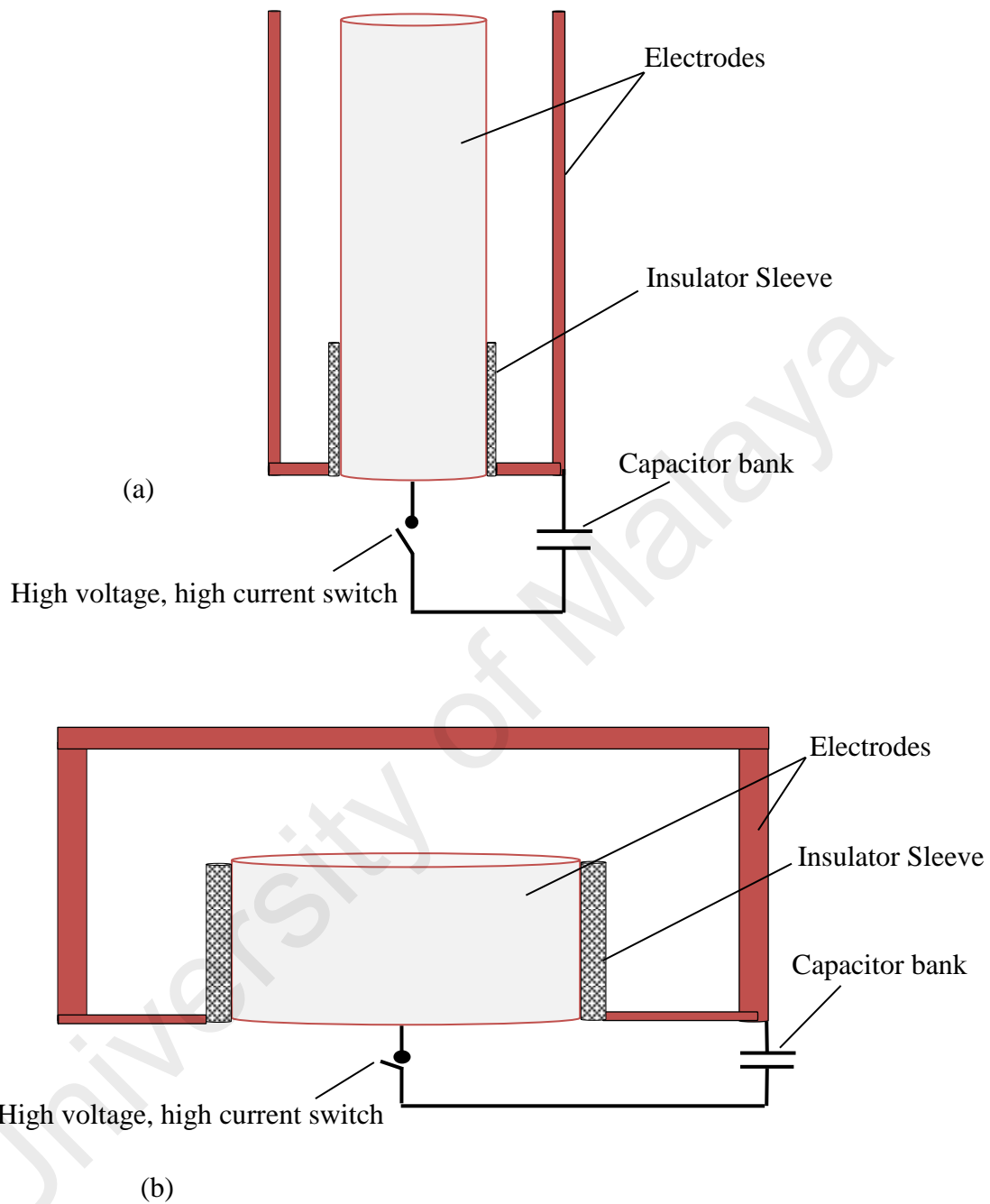


Figure 1.1: Sketch of plasma focus device geometry (a) Mather-type and (b) Filippov-type.

and industrial applications of the plasma focus device. Several points related to its rank in plasma physics and scientific applications are discussed henceforth.

1.3.1 Basic Plasma Physics

As previously stated, plasma focus is an inventive device that produces various compelling plasma phenomena, such as the formation of high energy density plasma state, pinch plasma, the formation of fast-appearing micro-instabilities and turbulence, and formation of short-lived hot spots, filaments, and jets [8, 20], among others. The device is a convenient source of EM radiation ranging from IR to X-ray, charged particles (ions and electrons), and neutrons. Each emission has its own characteristics and allows copious information on their emission mechanism and related physical processes. Lee *et al.* [21] stated that given its simplicity and economical features, plasma focus is an outstanding device for teaching plasma dynamics, plasma nuclear fusion, and thermodynamics. Notably, the acceleration of charged particles in plasma focus shares a certain resemblance with the particle acceleration processes in astrophysical phenomena [22]. The power dependence law of electron beam spectra from plasma focus has been observed to be similar to that of solar flares [23] and cosmic rays. The studies on these plasma phenomena and emissions would not only aid in understanding the basic physical processes but also provides clues for the explanation of several astrophysical phenomena, as well.

1.3.2 Technological Applications

The excellent performance of plasma focus as a device for various applications has been demonstrated by various workers [19, 24-30]. Researchers drive to explore the potential of utilizing the plasma focus device for industrial

use has a number of key points. Those few key points are operational simplicity, compactness, and short processing time. Extrapolating plasma focus as a fusion reactor may be a distant possibility, but the device's attribute as a neutron source may have applications in neutron radiography [31], activation analysis [25], and medical therapy [26]. Plasma focus presents an X-ray source that has applications in diverse fields, such as lithography [32], X-ray microscopy [33], micromachining [27], radiography [28], [34], and others. The poly-energetic ion beams of plasma focus have applications in ion implantation [19], surface coating [29], thin-film fabrication [30], testing material of fusion [35, 36], and others. The electron beam of plasma focus devices has medical applications, for instance, Intra-Operative Radiation Therapy [9] and also in thin film deposition [37], etc.

1.4 X-ray Emission from Plasma Focus Devices

X-ray emission has been stated to originate from several plasma devices, such as tokamak [38], magnetic bottle [39], synchrotron [40], plasma focus [41], X-pinch [42], vacuum spark [43], Z-pinch, and etc.

X-ray emission from plasma focus devices has been studied since 1959 [41]. Paaseen *et al.* [44] studied the X-ray spectrum from plasma focus. Harries *et al.* [45] reported two X-ray emission sources. X-ray is emitted from the focus region with lower energy, whereas the second X-ray originates from the tip of anode with higher energy. The interaction of the electron beam with the target is the mechanism of X-ray emission from the anode region.

Zakaullah *et al.* [46] reported that anode shape, distance from the anode tip and gas pressure are key parameters to yield the X-ray emission from plasma focus. Zakaullah *et al.* [47] revealed that the plasma focus enhances electron and X-ray

emission in the presence of a magnetic probe near the focus region. Zakaullah *et al.* [48] found that soft X-ray emission zone was broadened at low filling gas pressure, and a significant total of X-ray originated from the tip of the anode.

Chee Mang *et al.* [49] found that the electron beam activity on the copper anode is accomplished to originate soft X-ray from plasma. Three pressure regimes were identified, in general. In the first regime, both the plasma X-ray and copper line radiation were weak, while in the second regime, both the emission from plasma and contribution from the copper line were strong. The plasma X-ray was intense in the third pressure regime, whereas the contribution from the copper line was weak.

Beg *et al.* [50] reported the X-ray emission from the plasma of the gases of deuterium, nitrogen, neon, and xenon. The group deduced that gas pressure plays strongly to the X-ray emission from plasma focus. The efficiency of plasma focus is considerably higher than that of a conventional X-ray tube for X-ray production. Thus, the plasma focus device appears to be far superior to other table-top X-ray sources for applications.

1.5 Other X-ray Sources

There are other X-ray sources in detail as follows:

1.5.1 X-Pinch

The X-pinch [42, 51] was first proposed by Ullschmide, at the Lebedev Institute, Moscow in 1981. Early tests were led to investigate constriction at the cross-point. An intense, compact source of soft X-ray was confirmed to be emitted mainly from a localized region nearby the cross-point [52].

X-pinch is similar to Z-pinch. It involves two or more fine wires with the order of micron. It crosses and touches at a single point in the middle of two wires that form the 'X' shape. The 'X' shape of two wires is the load of the high current pulsed power generator. The plasma forms around the wires after their current driven explosion where a complex pinch process occurs at the cross-point. Plasma develops near the original cross-point of the wires by hundreds of micron long Z-pinch. Tiny pinch spots emit short bursts of 1.5 keV to 8 keV radiations. The intense radiation emits in the range of 8 keV to 100 keV, where a small portion of the radiation is associated with micro pinches. In X-pinch, higher energy X-ray emission is observed immediately after the soft X-ray burst. It is attributed to electron acceleration in the gaps that appear in plasma structure.

1.5.2 X-ray Emission from Vacuum Spark

There are many types of X-ray sources in plasma physics, the vacuum spark is one of the old type of source that produces X-rays. In 1930, vacuum spark was introduced to produce X-ray emission from plasma [53, 54]. The current passed through a very small amount of matter is blown off an electrode in vacuum spark device, either spontaneously or in a controlled manner with a laser. Thus producing plasma is of the electrode material in vacuum spark device. It is considered to be the class of transient linear plasma discharges that include Z-pinch. The vacuum spark has been developed as a pulsed X-ray source, as well as stripped ions source [55, 56].

The X-ray spectrum of vacuum spark is considered to be the close resemblance to that of solar flares. In the laboratory, vacuum spark is a source to use to stimulate the solar flares event. A plasma point is known as a hot spot that is assumed to be a small volume of dense plasma. This is an intense X-ray radiation source, which is formed because of the presence of instabilities in the compression phase. The high voltage is

applied between two electrodes to obtain the electron temperature, electron number density and radial phases of discharge in the vacuum spark [57].

The existence of tiny micro pinches is due to the low inductance discharges of vacuum spark that consists of anode material. Those vacuum spark discharges are powerful emitters of X-ray radiation in vacuum spark [58]. The production of electrons and HXR from the vacuum spark plasma is the result of the sausage instability that develops by high E-field in the direction away from anode [59].

1.5.3 X-ray Emission from Z-Pinch

The Z-pinch device is the simplest geometry that consists of plasma column with a large current flowing along its Z-axis. The plasma confines by pinch effect due to the self-generated azimuthal magnetic field B_θ occurs due to the axial current J_z . A $J \times B$ force acting in the radial direction constricts plasma toward the Z-axis. This plasma constriction toward the center increases plasma density and confines the plasma for a sufficient time length to achieve Lawson criterion for successful thermonuclear reaction. Z-pinch is used for X-ray applications among others. The micro-lithography and microscopy are the application of X-ray emission from Z-pinch [60].

1.6 Electron Emission from Plasma Focus Devices

At present, a plasma focus device is a proficient system in plasma physics research and applications. The electron beam emission from plasma focus is an important event in plasma physics research because numerous scientists are attempting to understand the correlation with other parameters of the plasma phenomena. The device is compact and reliable and offers performances in terms of intensity and of time

< 100 ns [61]. Previous reports presented time correlations studies on neutron emission with respect to HXR emission and other charged particles, but remarkably few reported electron beam emission correlation with time-resolved studies.

Choi *et al.* [62] observed X-ray emission from plasma focus at 60 kV/28 kJ to be closely related to characteristics of the electron beam emission. The electron beam emission occurs in two periods. The first period of electron beam emission showed initial statistics of pinched plasma, which terminates with the disruption of the plasma column, whereas the second period is generated after the collapse of the focused plasma. They found a relativistic electron beam during the first period of compression of stable plasma from machines with similar energies at lower voltages.

Favre *et al.* [63] investigated the temporal and spatial characteristics of X-ray emission in a 3 kJ plasma focus, which was operated in an admixture of hydrogen plus argon. The group used a multichannel system of PIN diodes with filters (Ti, Cu, Al, and Mo) of different thicknesses in axial and radial positions to detect the X-ray emission from the focus. They identified two X-ray emission periods, one from electron beam activity while other from dense plasma in the process of plasma focus. They discussed the plasma focus dynamics on the basis of those X-ray emission characteristics.

Wong *et al.* [64] studied the temporal, spatial, and spectral evolution of X-ray emission from a small 3.3 kJ Ar plasma focus device. A five channel PIN diode X-ray Spectrometer (DXS) and X-ray pinhole imaging system were used as diagnostics. DXS was used to investigate the spectral evolution of X-ray emission from focused plasmas. The pinhole camera was used to provide information on the structure of X-ray emission regions during plasma focus discharge. Two periods of X-rays emission were observed during the focus discharge; the first period of X-ray emission occurred during radial compression, whereas the second period occurred after maximum compression at a time

of 200 ns. The first period of X-ray emission was emitted from hot Ar plasma with an electron temperature of approximately 1.5 keV, whereas X-ray emission with Cu-K α line radiation was observed in the second period. A possible mechanism for the production of X-ray emission burst was the compression of copper vapor ejected from the anode, which is due to electron beam bombardment.

Zakaullah *et al.* [48] studied the measurements of the electron beam, ion beam, X-ray, and HV probe signals using low Ar filling pressure of 0.25 mbar energized by a 32 μ F, 15 kV capacitor. The soft X-ray emission zone was broad, and a significant amount of X-rays originated from the tip of the anode at low Ar filling pressure. The X-ray emission zone was contracted to pinch the filament at the axis with increasing Ar gas pressure. The intensities of the X-ray, electron beams, and ion beams signals were found to be mutually correlated, as well as with HV probe signal intensity.

Serban *et al.* [65] presented an analysis and detailed description of electron beam emission from a 3 kJ/14 kV plasma focus operated in the range of 1.5 mbar to 5.5 mbar of the operating gas, neon. A fast derivative Rogowski coil (RC) coupled to an appropriate RC passive integrator to measure electron beam current. The diagnostics were used to measure X-ray emission in the range of 0.5 keV to 40 keV and photon energies exceeding 70 keV, as well as to capture X-ray images of the focusing area. The group reported several periods of electron emission and demonstrated optimal electron beam production at an operating pressure of 4 mbar Ne.

Zakaullah *et al.* [66] investigated the X-ray emission from Mather-type plasma focus with Ar filling gas. Attention was paid toward determining the pressure range for the highest Ar K-series line emission. The Ar line radiation yield was the highest at 1.5 mbar, and the emitted energy in 4π geometry was found to be about 30 mJ. The highest X-ray emission and the radiation yield were found to be 3 keV and 0.7 J at the pressure

of 0.5 mbar filling pressure, respectively. This radiation emission was mainly due to the bombardment of energetic electrons with the anode.

Pouzo *et al.* [67] measured electron beams into a hollow anode of a 2 kJ/4 μ F small plasma focus device. A small RC was used into a cavity found in the hollow anode. The electron beam energy was calculated through time-of-flight of electrons between the probe and anode top. Electron beam pulses of about 10 ns width were determined in small plasma focus. HXR signals were obtained by using a scintillator–photomultiplier system. The electron beam energy was found in the range of HXR energy.

Grusdev *et al.* [68] studied the application of electron beam device as a source of heat energy for modification of material properties. The group designed a plasma electron source (PES) to study the surface properties of materials. PESs allow for the creation of electron beams with different cross-sections with minor changes in their design. The creation of electron beam with large cross section used the working pressure of up to 10^{-2} mbar in PES. High stability of electron beam parameters was achieved in the special configuration of electric and magnetic fields in the electron extraction portion.

Jakubowski and Sadowski [69] reported pulsed electron beams within plasma focus type facilities. The pulsed electron beams were conducted to give the formation of high-temperature plasma micro-regions, and instabilities of current filaments. The pair studied selected X-ray spectrum lines in correlation with pulsed electron beams. The pulsed electron beam emitted perpendicularly to the discharge axis, as well as in the upstream direction.

Neog *et al.* [70] investigated electron beam emission from a 2.2 kJ plasma focus. The group used a Faraday cup and RC assembly to measure the current. The electrons

were collected on the Faraday cup and optimized the pressure at 0.3 Torr of N₂. The electron emission occurred in multiple bunches that strongly dependent on operating pressure. The maximum electron beam charge and density were found to be 7.5 mC and $4.5 \times 10^{16} \text{ m}^{-3}$, respectively at optimized pressure. The team measured electron energy distribution in the electron beam by using the self-bias technique. They found a wide range of energies approximately from 10 keV to > 200 keV in the electron beam originating from plasma focus.

Neog *et al.* [71] provided valuable information on the time evolution of various radiations (SXR, HXR, electron beam, and ion beams) from 2.2 kJ plasma focus, as well as their interdependence. The estimated effective HXR photon energy, ~ 110 keV, proved to be consistent with the electron beam energy distribution. The emission of high energy electron beam and HXR photon was indicative of the presence of a high accelerating field inside the pinch column.

Numerous results of electron beam energy in the world laboratories reported by different authors are summarised in Table 1.1. The last one row was introduced to demonstrate results obtained in our laboratory. The last row concentrates the electron emission results offered in this thesis.

Researchers studied to identify the exact mechanism of the electron beams emitted from the plasma focus, however, the results are inadequate. In additional, it is reported that strongly influenced by the type of detectors used and by the methods employed to extract the physical information from the experimental data. The plasma focus devices can be used as potential applications.

Table 1.1: Summarised results of electron beam energy in World Laboratories.

Device Name	Laboratory Country Name	Capacitor Bank		EB Energy (keV)	Author Ref.
		Voltage (kV)	Energy (kJ)		
F	Lebedev /Russia	27	50	100	Gribkov [20]
M	NASA/USA	25	25	50	Harries [72]
M	Stevens/USA	15	5	300	Bostick [73]
M	Gunma/ Japan	30	24	<300	Hirano [8]
M	Illinois/USA	25	12.5	27	Stygar [7]
M	Maryland/USA	17	3	27-280	Rhee [74]
M	Stuttgart/Germany	60	28	50, >180	P. Choi [75]
M	NTU/Singapore	10	1.6	>10	P. Lee [76]
M	NTU/Singapore	14	3	30-660	Patran [77]
M	CPP/India	25	2.2	80-110	Neog [70]
M	PTRC/Malaysia	12	2.2	50-586	Khan*[78]

*Electron beam energy from the plasma focus device (UM-DPF2) in University of Malaya.

*F stands for Filippov and M stands for Mather.

1.7 Motivation of the Research

To broaden the value of plasma focus for applications, a better understanding of the fundamental processes in hot plasma is crucial, as well as optimizing a certain device for a specific application. The energy and the maximum output for X-ray photons are dependent on electrical parameters, gas composition, and filling conditions. A strong electron beam can be used for experiments concerning material ablation, pulsed lithography, or pulsed laser pumping.

The current project was to inspect the electron beam emission from a compact 2.2 kJ plasma focus operated in Ar. The electron and time resolved X-ray recorded data were correlated with the operating parameters of the device, the EM characteristics of the discharge, and with other diagnostics.

Several diagnostics techniques were successfully implemented during the project, namely, high voltage probe, five-channel PIN diode, Faraday cup, XR100CR X-ray spectrometer, and PMT with scintillator as detectors, as well as the Lee model code for calculating electron beam fluence for comparison with the measured electron beam fluence obtained from the low energy plasma focus device.

The main goal of our project was to conduct an in-depth investigation on the electron beam emission from the UM-DPF2 device within a specific pressure range, as well as on the X-ray emission in the same pressure range. The findings are extremely important, not only for academic studies but also as a foundation for future direct applications of the electron beam emitted by low energy plasma focus devices.

1.8 Layout of the Dissertation

The thesis is organized as follows:

Chapter 1 (Introduction) gives some introductory and historical elements of the plasma focus. This is followed by the arrangement of the layout of this thesis.

Chapter 2 (Plasma Focus and Related Phenomena) is devoted to the description of the plasma focus and emission of the radiation. The first part describes the dynamics of the dense plasma focus discharge while the last part of the chapter illustrates the updated results of the theoretical and experimental works performed by other researchers in the area of electron and X-ray emission from the plasma focus. The Lee Model is also presented in detail.

Chapter 3 (Diagnostic Technique and Experimental Setup) describes in detail the diagnostic techniques in this work. It also provides the details of plasma focus facility-University of Malaya dense plasma focus (UM-DPF2), together with the specific arrangements and experimental setup employed in this project.

Chapter 4 (Experimental Results and Discussion) presents the experimental results and provides a detailed discussion on the interpretation of data.

Chapter 5 (Conclusions and Suggested Future Work) contains the conclusions of this present work and proposes some practical directions for the future investigations of the focus phenomena.

CHAPTER 2

PLASMA FOCUS DYNAMICS AND RELATED PHENOMENA

2.1 Introduction

Plasma focus is a simple way to achieve thermonuclear conditions for controlled fusion applications. A plasma focus device is a magneto-hydro-dynamic coaxial plasma accelerator [79]. The magnetic energy is stored behind the moving current sheath (CS). This energy is converted into plasma energy during the rapid collapse of the CS toward the axis beyond the end of the central electrode. CS compression occurs at the end of the electrodes when the plasma column has high temperature and density. The use of plasma focus is advantageous over other facilities because of its less complicated operation and simple conventional capacitor bank design.

The study of plasma radiation provides an excellent analysis to understand the plasma focus phenomenon involved. This project attempts to investigate the X-ray and electron beam emissions from the focus region when the present device is operated with Argon as the filling gas.

2.2 Dense Plasma Focus Dynamics

The dense plasma focus device is a magneto-hydro-dynamic coaxial plasma accelerator that generates dense and hot plasma through a self-generated magnetic field. The two well-known geometries of plasma focus devices were developed independently by Filippov in the USSR and by Mather in the USA in the early 1960s. The behavior of the Filippov- and Mather-type devices is almost identical in terms of radiation emission

from the focused plasma region besides the different aspect ratios. The Filippov [80] geometry has an anode aspect ratio (diameter/length) larger than one (>1), whereas the Mather [2] geometry has an anode aspect ratio (diameter/length) smaller than one (< 1). The plasma focus device under investigation at the Plasma Technology Research Center, University of Malaya is a Mather-type plasma focus device shown schematically in Figure 2.1.

Filippov was working on a linear Z-pinch device. He replaced the glass vessel with a metallic chamber and inserted an insulator sleeve between the anode and metallic chamber to overcome the influence of the glass vessel used to introduce the impurities into the plasma. The discharge was observed across the insulator sleeve at the breach of the electrode assembly, whereas a non-cylindrical pinch plasma column was formed near the anode terminus. Mather's geometry was developed based on a coaxial plasma accelerator. The discharge develops initially across the insulator. The CS accelerates to the open end and then collapses in front of the anode face.

The central electrode in a plasma focus device is usually kept at a positive polarity to the other electrode. The neutron and X-ray yield decreases by an order of magnitude when the polarity of the electrode is reversed in the device operation. Decker *et al.*, [81] investigated the effects of polarity on dense plasma focus operation. The electrons play a dominant role in gaseous breakdown because their mass is much smaller than the ions' mass. Free gas charges are accelerated toward the electrodes and insulator sleeve by applying the high voltage because of the image force.

When the central electrode is positive, the electric field lines help to concentrate the electrons toward the insulator sleeve surface. This condition helps in the prompt initiation of the low inductance breakdown. The electrons move outward and provide no help in CS formation when the central electrode is negative, thus delaying the breakdown.

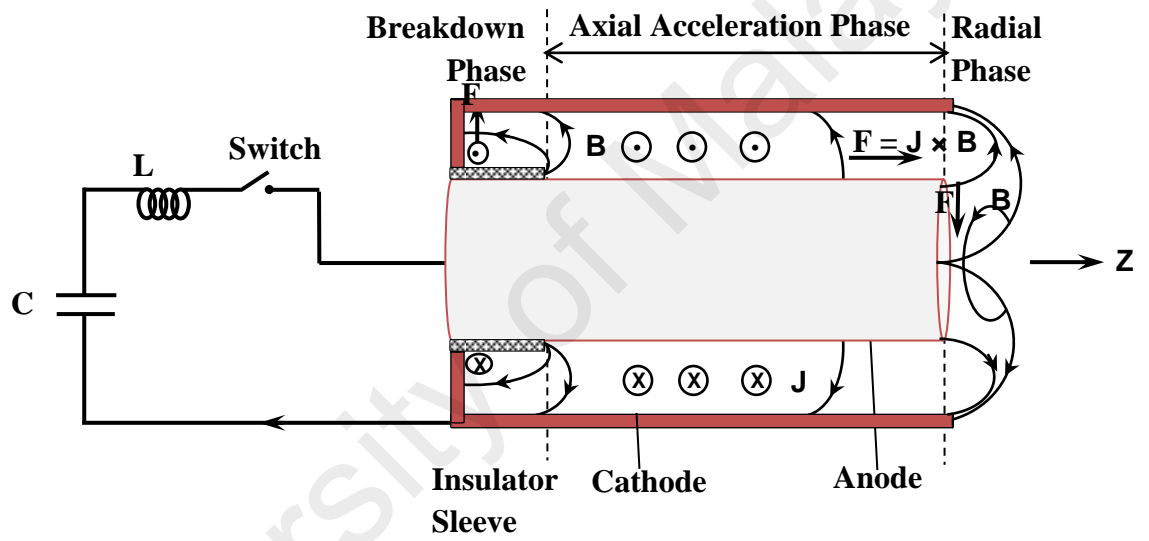


Figure 2.1: Schematic of the Mather-type plasma focus device.

The neutron source size because of the beam target mechanism decreases in this fashion, so the contribution of X-rays by the electron beam impact at the anode surface is eliminated.

Plasma focus dynamics can be divided into three steps, namely, the breakdown, axial acceleration, and radial phases; also more phases after the pinch, axial shock, and jets [8, 82, 83]. These phases are described in the following sections.

2.2.1 Breakdown Phase

The breakdown phase is defined when a high voltage pulse (12 kV in our case) is applied between the two co-axial electrodes of the plasma focus device with an appropriate working gas pressure. The breakdown phase starts along the surface of the insulator cylindrical tube because of surface capacitance. The free electrons in the vicinity of the insulator tend to create a negative potential at the insulator surface because of the dielectric constant of the material and high surface resistivity. The delay time between the high voltage application and breakdown is approximately a fraction of a few nanoseconds [84]. This time delay is almost independent of the voltage applied within a reasonable range but depends strongly on the initial pressure of gas [85]. More electrons are created by field emission from metallic edges and ambient gas ionization during this period. A sliding discharge develops along the insulator. A discharge is usually initiated at the edge of the outer electrode because of the appearance of a high electric field. The CS in this phase creates a path that enables the current to move from the anode to the cathode. It ends when the CS starts to move upwards because of the $\mathbf{J} \times \mathbf{B}$ force. Small magnetic probes, image converter pictures, fast voltage dividers, and Rogowski coils have been used as diagnostic tools for the breakdown phase. A more

detailed investigation can be achieved using high-resolution imaging techniques such as Schlieren and Interferometric.

The development of the high current discharge within the plasma focus system depends on the electrode geometry [46, 86, 87], the solid insulator sleeve [84, 88-90] and the initial gas conditions [84, 88]. A suitably selected length of the anode and insulator sleeve improves CS uniformity that leads to good CS compression.

Contamination of the insulator sleeve is also a very important factor [91]. It needs a minimum contamination level of for the prompt breakdown of the current, whereas the maximum contamination level promotes too much current loss that may give rise to multiple focus evidence. The frontal section of the CS that is attached to the inner electrode remains temporarily immobile during the breakdown phase. When the uniform CS is formed, the focus formation process enters the axial acceleration phase.

2.2.2 Axial Acceleration Phase

The electromagnetic (EM) force $\mathbf{J} \times \mathbf{B}$ begins to lift the CS off from the insulator in the inverse pinch manner when the CS is developed. This phase starts when CS leaves the insulator sleeve surface and ends when it reaches the anode terminus. The $\mathbf{J} \times \mathbf{B}$ force has $1/r$ dependence and drives the CS in radial and axial directions. The radial component $(\mathbf{J} \times \mathbf{B})_r$ is in an outward direction, whereas the axial component $(\mathbf{J} \times \mathbf{B})_z$ is in an upward direction. The CS moves faster near the anode surface compared with near the outer electrode as a result of the $1/r$ dependence of the force, which provides the CS with a parabolic. Magnetic probe measurements confirm that the CS velocity near the anode surface is higher than near the outer electrode (cathode). This CS parabolic shape has been verified by image converter photography.

The following factors ensure the importance of this phase:

First, the CS should arrive at the axis at an instant near the first maximum of the discharge current. This factor is a common requirement for all pinch devices, which shows the energy optimization from the capacitor bank to the pinch plasma. Optimization studies provide the time difference between the maximum current and end of the axial acceleration phase for an optimum energy transfer under the set of operating parameters for each device.

Second, the structure and (r, z) profile of the plasma sheath should have certain characteristics for a good focusing effect. This factor needs an axial symmetry, smooth (r, z) profiles, and a thin uniform CS structure.

No significant tangential stress exists within the CS because the forces acting on it are normal to the surface everywhere. Thus, CS evolution must be conceived as a type of swelling balloon rather than a rigid piston. The mean free path for all collisions involving ions and atoms is very small for the normal gas pressure range. A gas dynamical shock is produced by this fast moving structure. This shock heats and compresses the neutral gas in front of it. Therefore, the sheath will have a complex structure with a compressed and hot ionizing region.

The pattern of the driving current defines the complete CS structure: the more uniform the pattern, the smoother the sheath. An azimuthal filament pattern produces a filamentary-structured sheath [92, 93].

Different diagnostic techniques, such as magnetic probe measurements, the Schlieren method, shadowgraphy, interferometric investigations, image converting cameras, and other light detecting systems, are used for the axial acceleration phase. The measured sheath speed is from $1.5 \text{ cm}/\mu\text{s}$ to $15 \text{ cm}/\mu\text{s}$, and the sheath thickness is

between 2 cm and 4 cm [94, 95]. A large fraction (50 %) of the current going into the device flows behind the CS for large plasma focus devices.

One end of the CS sweeps around the open end of the anode at the end of this phase. The outer end of the CS continues to move along the tube, sweeping with it the larger portion of the accumulated plasma in the axial direction. Only a fraction of the plasma at the end of the axial acceleration phase contributes to the final focus.

2.2.3 Radial Collapse Phase

This phase deals with the rapid convergence of the CS to form a hot and dense plasma column beyond the inner electrode (usually anode) and finally collapse because of the inward $\mathbf{J} \times \mathbf{B}$ force. The $\mathbf{J} \times \mathbf{B}$ force causes 2D (r, z) convergence of the CS through the pinch effect. The column length increases as the compressed column reaches the minimum radius. The speed of the imploding CS is approximately 4×10^7 cm/s to 6×10^7 cm/s, which depends on the electrode geometry, initial gas pressure, CS structure, and electrical characteristics of the device [96]. Theoretical calculations reveal that ions can obtain speeds of approximately 7×10^7 cm/s to 9×10^7 cm/s in the last moments of this collapse phase. The ions and electrons are imploded at the same speed to form a hot plasma.

Only 10 % of the gas in front of the CS is converted near the anode tip. The focus is formed at a distance of ~1 cm to 1.5 cm beyond the central electrode tip, which lasts for approximately 50 ns to 300 ns depending on the device characteristics. The focus plasma volume has been estimated to be $\sim 15 \text{ mm}^3$ with a plasma number density of $n_e \sim 2 \times 10^{19} / \text{cm}^3$ to $n_e \sim 3 \times 10^{19} / \text{cm}^3$. The plasma column size is less than 1 mm in diameter with an electron temperature of a few keV. The pinch column length and its

minimum radius attained a scale to the central electrode radius [97, 98]. This plasma column is momentarily stable for a few tenths of ns in a small energy device to hundreds of ns in a large device. This process is similar to the Z-pinch phenomenon with enhanced compression and plasma heating. The expansion occurs in two directions, namely, axial and in radial directions. The axial expansion is unhindered that results in the formation of an axial shock-front, whereas the radial expansion is hindered by the confining magnetic pressure.

The plasma is heated by the shock heating effect, which depends on the gas speed, during the expansion. Joule-heating becomes the main heating mechanism after the plasma column formation, so the plasma column is further compressed adiabatically to form the final plasma focus. The Rayleigh–Taylor instability is set before the end of the axial collapse phase and dampened with diminishing radial velocity. Sausage instability ($m = 0$) develops rapidly because of the increasing electron temperature at the end of this phase. Therefore, pinch life-time (t_p) can be defined as the time between the first compression and the instant when the $m = 0$ instability occurs.

The magnetic field in this phase starts to diffuse into the plasma column, which results in an anomalous high plasma resistance and increase in the system inductance [99]. The sharp voltage spike and current dip measured by the high voltage probe and Rogowski coil are typical features of a discharge because of the large surge of the plasma column impedance. The high frequency oscillations at the beginning of signals and during the radial compression phase are due to the transmission line directly connected to the capacitor bank and electrodes [100].

Most of the magnetic energy stored behind the CS must be converted to plasma energy for a good focus. This condition is obtained by synchronizing the CS time of flight from the breech to the anode tip.

The rapid change of plasma inductance in the axial collapse phase results in an electric field in the plasma column, but the discharge current is almost constant. The induced electric field is provided by an equation.

$$E = I \frac{dL}{dt} \quad (2.2)$$

Where I is discharge current and $\frac{dL}{dt}$ is the rate of change of plasma inductance.

This electric field (E) accelerates the ions and electrons in opposite directions. The relative drift velocity builds up between the ions and electrons and approaches the increasing electron thermal velocity. This phase is the most important phase because of its extremely high energy density and transient character, as well as the emission of intense radiation, high energy particles, and copious nuclear fusion products.

The radial collapse phase may be sub-divided into four phases based on reported experimental data, namely, the compression, quiescent, unstable, and decay phases.

2.2.3.1 The Compression Phase

The compression phase is the first sub-divided phase, wherein the pinch plays a crucial role in plasma focus. This radial phase starts with the rapid collapse of the azimuthally symmetrical but non-cylindrical, funnel-shaped plasma sheath toward the axis under the influence of the inward $\mathbf{J} \times \mathbf{B}$ force. The radial implosion ends when the plasma column reaches the minimum radius with the plasma density at its maximum value of $\sim 10^{19} / \text{cm}^3$. This instant is the time reference when $r = r_{min}$, $t = 0$.

The main heating mechanism occurs inside the plasma before the front of the CS meets along the Z-axis. Therefore, the ~ 300 eV ions are much more significant than the

~ 100 eV electrons [101]. Joule heating becomes the main heating mechanism after the plasma structure is transformed into a plasma column [92].

The plasma column is compressed adiabatically for the formation of the final focus. The magnetic field starts diffusing very fast into the plasma column at the end of the sub-divided part of the collapse phase; it is associated with a sharp increase in the plasma anomalous resistivity [99]. A sharp voltage spike and a dip in the current are observed for a typical plasma focus discharge because of the large increase in the plasma column impedance.

Spectroscopy [44], interferometry [102], laser scattering [92], and several other methods are used to calculate the maximum value of the electron and ion temperatures. The final electron temperature can approach the range of 1 keV to 2 keV [37].

Assuming the Bennett equilibrium in this phase, the final temperature should only depend on the current I and linear density N (i.e., $T \approx I^2/N$); the lower the linear density, the higher the temperature. Therefore, the electron temperature is independent of the minimum radius ($r = r_{min}$) of the pinch plasma column.

A plasma column is formed at the end of the compression, and it stagnates for a brief time period. The column length of a few cm and column diameter is of the order of 1 mm, which depends on the dimensions of the central electrode radius [103]. The plasma density is $\sim 10^{19}$ /cm³ at this stage.

2.2.3.2 The Quiescent Phase

A plasma column is formed at the end of the compression phase and stagnates for a brief time period. The quiescent phase indicates the beginning of the plasma column expansion in the axial and radial directions after stagnation. The confining

magnetic pressure hinders the expansion rate in the radial direction. However, the plasma column expands unhindered in the axial direction because of the so-called “FOUNTAIN-like” geometry of the CS. Thus, an axial shock front is formed. Instabilities start to expand during this stage.

2.2.3.3 The Unstable Phase

This phase is richest in associated phenomena such as fusion reaction, neutron, proton, HXR, and SXR, fast deuterons, and electrons emission. The rapid change in inductance during this phase results in an induced E-field in the plasma column ($V = I \frac{dL}{dt}$), where I is the discharge current and $\frac{dL}{dt}$ is the rate of change of inductance. Given the sausage instability, this induced E-field expands. It accelerates the electron toward the anode and the ion away from the anode. Axial ionization was reported at the same time. The measured peak velocity of this front is 120 cm/ μ s. The ionizing front overtakes the axial shock front because of the axial expansion of the plasma column [82, 104]. The beginning of this ionizing front coincides with the development of hard X-ray and neutron pulse.

The electron velocity during this phase increases faster than the electron thermal velocity, which causes a high electron temperature (4 keV–5 keV). This phenomenon results in a large amount of measured bremsstrahlung radiation.

2.2.3.4 The Decay Phase

The decay phase is the last phase of the radial collapse and last stage of interest of plasma dynamics. A very large hot and thin plasma cloud is formed during this phase

because of the complete breaking of the plasma column. A large amount of bremsstrahlung radiation is emitted, and the SXR emission and neutron pulse reach their peaks. In the end, the plasma column breaks and decays, and the high E-field induced during this period result in the emission of an energetic electron and ion beams.

2.3 X-ray Production

The plasma emits EM radiation at a high temperature in the wavelength ranging from microwave to infrared, visible, ultraviolet, and X-rays. These radiation types arise from the interaction of electrons, ions, atoms, and molecules, as well as the interaction of these particles with the EM field.

The radial compression phase in DPF devices basically emits EM radiation in the energy range of 0.1 keV to 500 keV. Most studies were conducted using hydrogen or its isotopes (i.e., deuterium & Tritium) to mainly investigate neutron emission with a minor focus on X-ray emission. Cost-effective, compact, and high power X-ray sources for various technological applications have led to more intensive studies on X-ray emission from the plasma focus in recent years. The soft X-ray emission [105] in plasma focus is due to thermal processes such as free-free transition (Bremsstrahlung), free-bound transition (recombination), and bound-bound transition (de-excitation). High energy X-ray emission is due to non-thermal processes [106], which indicates the interaction of a high energy electron beam to the metallic anode surface.

X-rays emission mechanisms are explained in the following sections.

2.3.1 Free-Free Transitions (Bremsstrahlung Radiation)

Charged particles can be accelerated or retarded when they move in the electric field of other charges (Figure 2.2). This event radiates energy according to classical EM theory. This radiation type is known as Bremsstrahlung radiation.

When the electron velocity distribution is a Maxwellian distribution, the classical expression provides the frequency dependence of the free-free transition as $\exp[-h\nu/kT_e]$. The emission intensity is proportional to $n_e n_i (Z_i)^2 (T_e)^{-1/2}$, where n_e is the electron density, n_i is the density of the ions of effective charge Z_i , and T_e is the electron temperature.

The emission per unit frequency interval is

$$\frac{dE_{ff}}{d\nu} \sim \sum_i n_e n_i Z_i^2 \frac{\exp\left(-\frac{h\nu}{kT_e}\right)}{(kT_e)^{\frac{1}{2}}} \quad (2.3)$$

In terms of emission / unit length interval, $\frac{dE_{ff}}{d\lambda}$ shows a maximum given by

$$\lambda_{\max} = \frac{6200}{kT_e} \text{ (\AA)} \quad (2.4)$$

where kT_e is in eV.

The free-free emission has another property wherein the spectrum for short wavelengths is strongly dependent on T_e , whereas the spectrum for long wavelengths is independent of T_e . The analysis of this emission type is particularly suited for the estimation of the plasma electron temperature.

2.3.2 Free-Bound Transitions (Recombination Radiation)

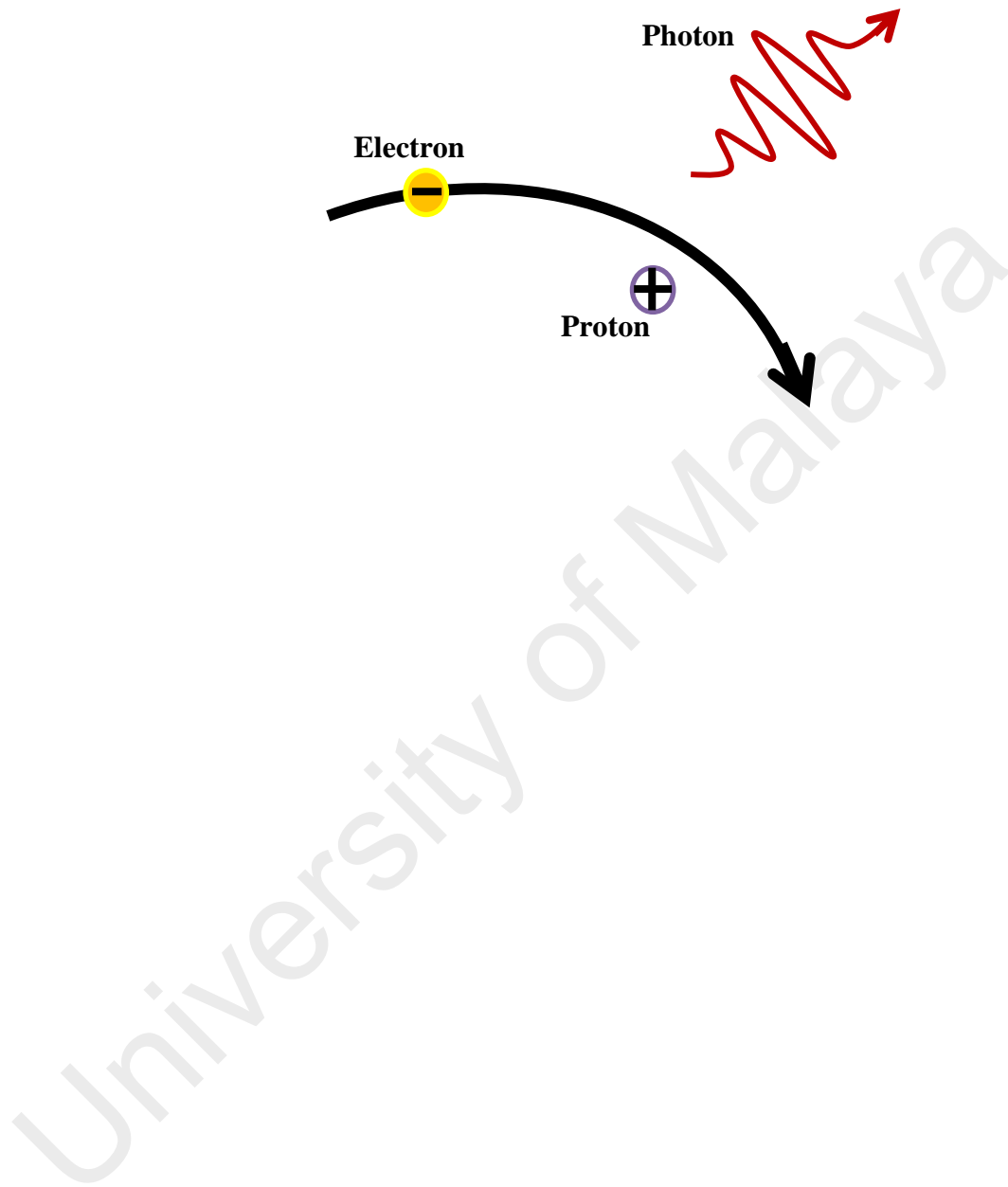
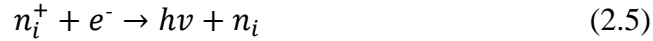


Figure 2.2: Bremsstrahlung radiation.

A free electron recombines with an ion and forms a neutral atom to emit photon energy $h\nu$ in a recombination process (Figure 2.3).

Therefore, the emission of energy radiation produces a continuous spectrum of radiation. This expression can be written as follows:



The frequency dependence of the recombination radiation for this process is written as follows:

$$\frac{dE_{bf}}{d\nu} \sim n_e n_i Z_i^4 \frac{\exp\left(-\frac{(h\nu - \chi_n)}{kT_e}\right)}{kT_e^{\frac{3}{2}}} \quad (2.6)$$

Where, n_i = the number of ions of charge i and χ_n = the ionization potential of the n th state of the atom or ion.

Thus, the frequency dependence of the free-bound emission shows that electron capture in a completely stripped ion appears similar to the free-free emission. The exceptions are the discontinuities in the emission at frequencies corresponding to the ionization potential (χ_n) of the final state because the intensity is proportional to Z_i^4 rather than Z_i^2 . Thus, the continuum radiation from plasmas is dominant at short wavelengths by recombination radiation.

2.3.3 Bound-Bound Transitions (Line Radiation)

An ion, atom, or molecule transitions to the ground state through stimulated or spontaneous emissions when it is in the excited state. The emitted photon energy is provided by the difference of the energies of the initial state E_1 and final states E_2 . Thus, the emitted photon energy can be written as follows:

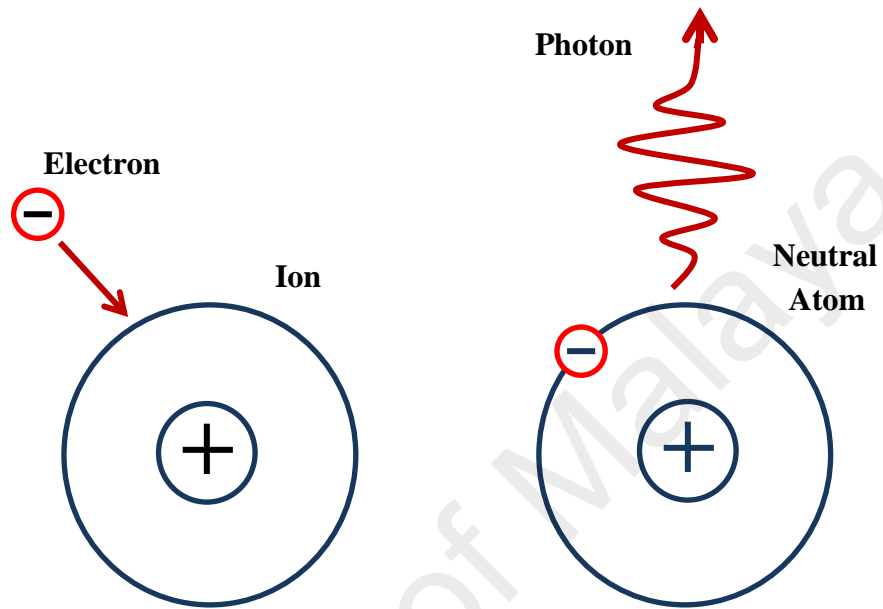


Figure 2.3: Recombination radiation.

$$h\nu = E_1 - E_2 \quad (2.7)$$

These radiation types are called line radiation as shown in Figure 2.4.

These radiation types are also known as characteristic radiation because of the characteristic properties of the emitting ion, atom, or molecule. The bound-bound transition appears as a discrete packet of energy or lines. The characteristic X-ray spectra are correlated with a definite series of lines called the *K*, *L*, *M*, *N*, ... series. Given that the K-series belongs to the spectra, it arises from the transition from higher states ($n = 2, 3, 4, \dots$) to the *K* state similar to other series.

2.4 Electron Beam Production

In the early experiments, electron beam emission from the pinch area was observed in the plasma focus devices [18, 77, 107, 108]. The electron beam interaction with the metallic electrode was the source of the HXR emission [96], [109].

The observed energy was mainly in excess of the discharge voltage. The electron beam production had to be associated with ion production. Few acceleration mechanisms for these energetic particle beams were discussed and proposed [109].

The increase in the amount of energy gained by an electron between two interactions with the ion population (due to different acceleration mechanisms) leads to an increasing average speed, which in turn decreases the interaction cross-section. When the electric field along the plasma column becomes higher than the critical E_{cr} corresponding to the existing plasma conditions and geometry, the electrons with higher-than-average energies start to “*escape*” from

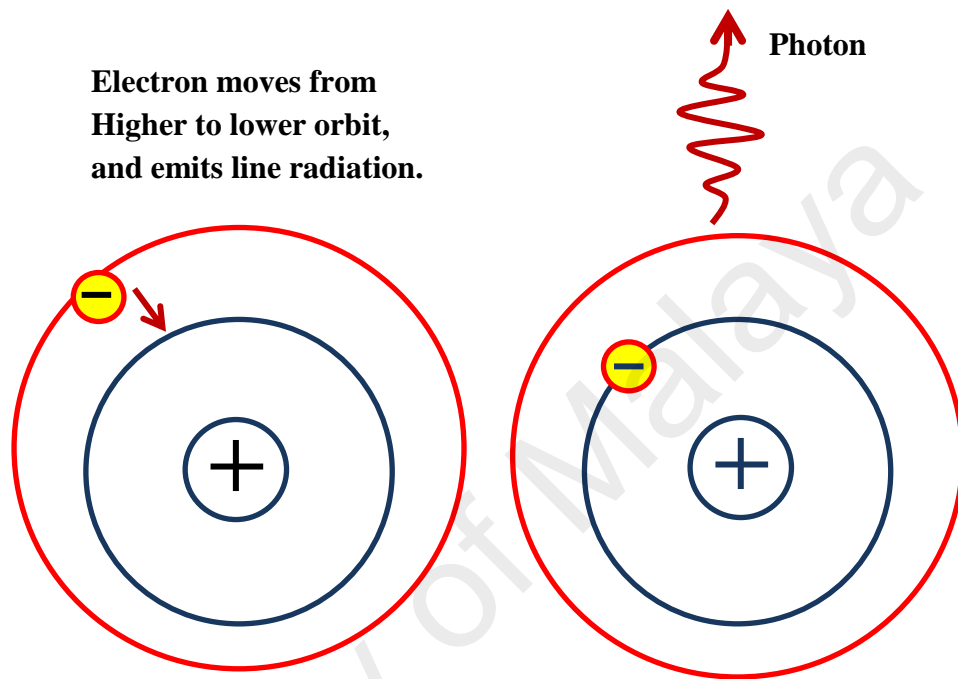


Figure 2.4: Line radiation.

the pinch area, are called “*runaway electrons*”. Generally, this process is named as the runaway process [110].

Two noticeable points of this process have demonstrated as the current flows along the shock front and the cylindrical shock collapse on the axis within the free region of magnetic field.

It is a highly complicated mechanism to produce the pure and mono energetic electron beam from the plasma focus device. The electron beam starts with the runaway electrons emission under special local plasma conditions. These electrons interact with the plasma and also change the energy balance. Therefore, the local conditions are self-modifying [111].

Several processes have been offered to define the electron beam acceleration up to energies of more than 100 times higher than the applied voltage [77], in general. The general phenomena are considered to be the rapid local changes in the magnetic flux that account for the high electric field in the plasma. This process starts once the plasma starts being compressed by the Lorentz force [112]. The electrons are enhanced more efficiently, and the sausage instability can again arrange suitable conditions for this phenomenon to occur.

The electron beam can extract from plasma through noticeable three electron groups for measurement, as follows:

1. low energy electrons;
2. higher energy electrons; and
3. Very high energy electrons

The measurement of the electron beam is not very simple. The detectors are not able to detect the *low energy electrons* from focus because of mostly

trapped by the strong magnetic field, whereas the *higher energy electrons* from focus interact strongly with the filling gas and then vanished. The group of *very high energy electron* did not experience any significant interactions with the plasma, electrode system or the filling gas, but are lying to interact among themselves.

The direct measurement of the electron beam is very difficult because of the existence of the filling gas in the plasma focus device. It is very dangerous to make the direct coupling with scope in the presence of high voltages. For the measurement of the electron beam, we use the X-ray emission from a target, which could be the anode itself. In most experiments, direct parameters have also been obtained with the use of Faraday cups [23, 113].

The peak energy is neither related to the charging voltage of the capacitor nor the stored energy of the capacitive pulsar in the case of measurements of both electron and ion beams [88].

Pure, mono-energetic electron beam emission is impossible to directly design a plasma focus device. However, the electron beam emission can enhance for a specific device under few operating conditions.

The most important factor is operating pressure that affects the amount of the electrons emitted from the plasma focus. The HXR yield emitted because of anode bombardment increases as the gas operating pressure is lowered [114]. The experiment reproducibility is decreased by the gas operating pressure decreases [113].

The pressure change is an important factor from others factors.

1. As the pressure decreases, the emitted electron energy increases. The

low pressure enhancement can only be observed down to a certain value, beyond which the focus column is poorly formed and the emission intensity decreases [115].

2. As the pressure increases, the beam-plasma interactions inside the pinch become more effective. The electron emission from the pinch and bombardment decrease. The X-ray emission intensity related to these phenomena also decreases [116].

A poor electron beam current was detected at 50 ns before the first compression in high energy machines (Filippov-type and Mather-type). The electrons emitted during the first compression was correlated with the symmetry and quality of the collapsing sheath [88, 117].

Above both situations can be structured by a suitable high voltage operation [118] as follows:

1. Improve the quality of the breakdown;
2. Produce a uniform CS with lower energy losses; and
3. Decrease impurity ablation from the insulator.

The EM parameters of the plasma focus device are directly controlled the electron beam emission. The efficiency of the electron beam emission can improve by increased values of the magnetic field produced by the pinch current.

Different results of the energy of electron beam reported by different authors in the world. Many groups attempted to find the mechanism of the electron beam emission from the plasma focus, but the results are insufficient.

The additional study reports that electron beams are strongly influenced by the type of detectors used and the methods used to extract physical

information from the experimental data. Expensive laboratories use electron beam generators within a large range of energies, and plasma focus can be used with potential applications.

2.5 Lee Model on Plasma Focus

Experiments were performed along with the development and implementation of the physical model. Some experimental results were used as code input parameters. The numerical simulation results can be used to support the experiments. A comparison of the numerical simulation with the experimental results is presented in Chapter 4.

2.5.1 Evolution Process in Plasma Focus

The plasma focus dynamic process is usually divided into three phases, namely, the breakdown, axial rundown, and radial collapse phases. The radial phase contains compression, quiescent, unstable, and decay sub-phases as mentioned in the plasma focus dynamic process.

The related evolution processes (axial phase to radial phase) were simplified to develop and implement the computational model as shown in Figure 2.5.

This approach was based on and summarizes the works by Lee [119]. Lee's model was a basic magneto-dynamic code, but further developments [120] was proposed and incorporated. The processes were treated as four phases in early modeling: axial phase, radial phase (radial inward shock phase), reflection phase (radial reflected shock phase), and slow compression phase (radial slow

compression phase). Presently, the Lee model (RADPF5.15FIB) was configured to operate as the UM-DPF2.

The features of these phases are as follows:

2.5.1.1 The Axial Phase

This phase begins after the breakdown phase, which is not considered in this model. The up-moving (Figure 2.5a) plasma layer is simplified as a flat annular conductive sheath that connects the anode to the cathode. It sweeps from the anode bottom to the top and accumulates a fraction f_{m1} of all the encountered mass of the working gas. The axial position of the sheath is z , where the z -axis is pointing upwards in the direction of the open end of the electrode system.

The axial phase begins at $z = 0$ and is considered as a back wall insulator that ends at $z = z_0$, where z_0 is the anode length. Therefore, the mass of the plasma sheath at z is $f_{m1} n_0 m_i z \pi (b^2 - a^2)$, where n_0 is the atomic number density of the filling gas, m_i is the atomic mass of the filling gas, a is the anode radius, and b is cathode radius.

2.5.1.2 The Radial Inward Shock Phase

This phase is divided into three sub-phases, namely, radial inward shock, radial reflected shock, and slow compression phases. The plasma is treated as a slug with the piston position as outer radius r_p , shock front as inner radius r_s , and height z_f measured from the open end of the anode (Figure 2.5b). The slug is

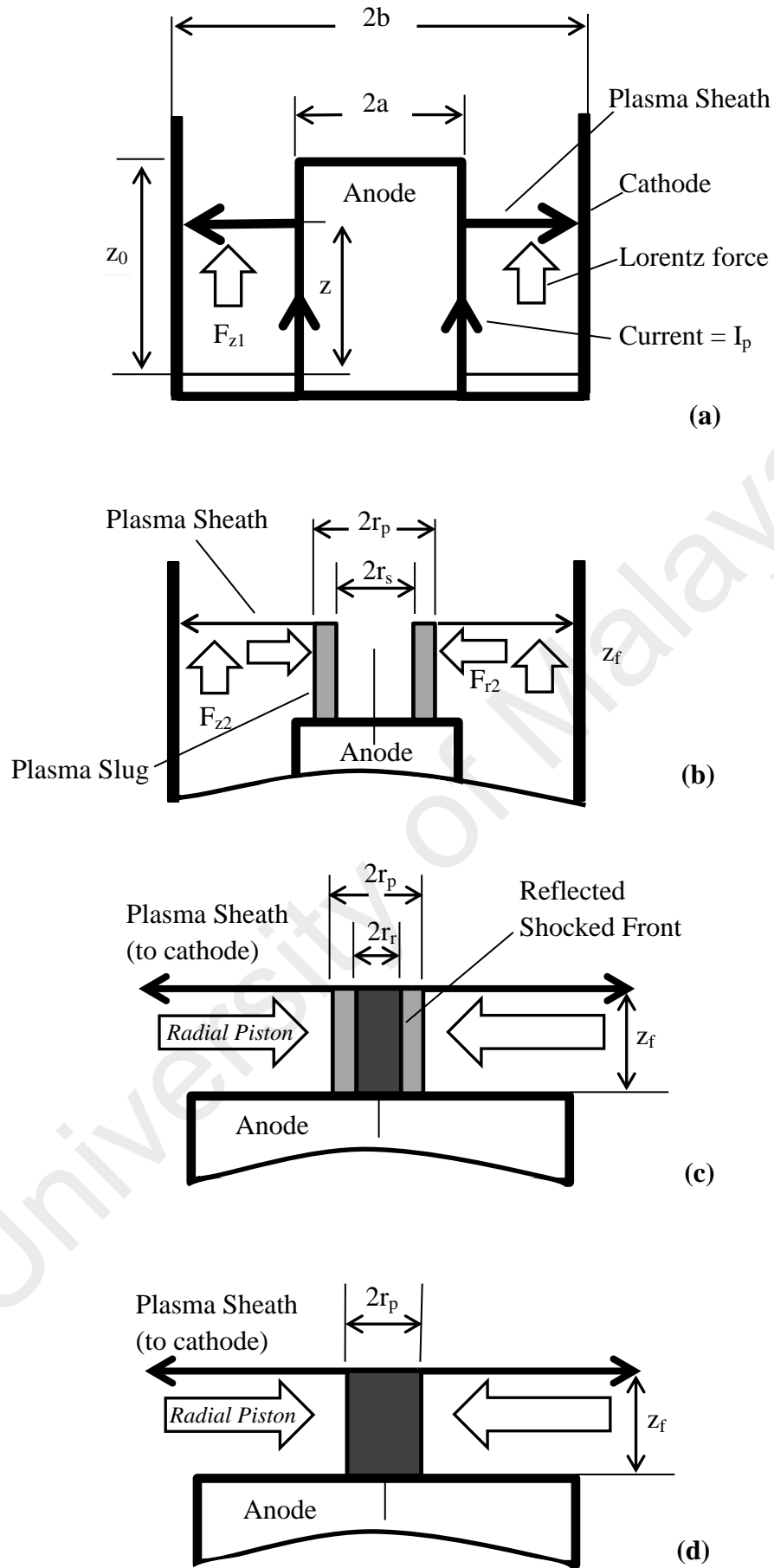


Figure 2.5: Simplified model of the pinch formation phases.

compressed radially inward by the radial magnetic piston. The gas fraction f_{m2} in the path is collected into the slug. The inward shock phase begins at $r_p = r_s = a$ and ends at $r_s = 0$ when the shock front meets the axis center.

2.5.1.3 The Radial Reflected Shock Phase

When the shock front reaches the axis, the particles in the slug convert a maximum of their kinetic energy into plasma internal energy by collisions. This event significantly increases the plasma temperature and the plasma density at the center. This process is called the reflected shock phase.

The plasma in this phase is separated into the central part of the relatively stationary hot and dense plasma column; and the outer part of the fast compressing plasma slug with lower temperature and density (Figure 2.5c). The boundary that separates the hot and dense center column with the outer plasma slug is defined as the reflected shock front. The reflected phase ends when all the particles join the center plasma column, that is, the reflected shock front and magnetic piston meet at a certain radial position ($r_r = r_p$).

2.5.1.4 The Slow Compression Phase

The slow compression phase follows the reflected shock phase. This phase is also known as the radiative phase where the pinch emits X-ray photons only for this part. The plasma column continues to compress until it is disassembled by the instabilities. The height z_f and radius r_p of the plasma column are the geometrical plasma parameters, as shown in Figure 2.5(d).

2.5.2 Electrical Properties and Circuit Equations

The plasma focus can be replaced by its equivalent electrical components for the modeling. The equivalent plasma focus electrical circuit during the discharge is illustrated schematically in Figure 2.6 [121].

The discharge loop is treated as an LCR circuit. C_0 is the capacitance of the energy bank, whereas R_0 is the circuit resistance and R_p is the plasma resistance. The circuit inductance contains the fixed circuit inductance L_0 and the charging plasma tube inductance L_p . The leakage resistance h_L in the plasma tube is directly related to the current leakage along the insulator surface.

The energy bank is primarily charged to a high voltage V_0 . The equation of this circuit can be written according to Kirchhoff's law.

$$\frac{1}{C_0} \int_0^t Idt - V_0 + R_0I + \frac{d}{dt}(L_0I) + R_pI_p + \frac{d}{dt}(L_pI_p) = 0 \quad (2.8)$$

And the tube voltage (voltage across the points A and B) is

$$V = V_0 - \frac{1}{C_0} \int_0^t Idt - R_0I - \frac{d}{dt}(L_0I) = R_pI_p + \frac{d}{dt}(L_pI_p) \quad (2.9)$$

The electrical parameters of the plasma tube and circuit equations in each phase can be explained for the simplified plasma geometry as follows:

2.5.2.1 The Axial Phase

The configurations of the plasma tube and plasma sheath are simplified in the axial phase as shown in Figure 2.5(a). The current conductor is composed of the electrodes (conductive cylinder) and plasma sheath at position z measured from the anode bottom. This electrical system is a cylindrical coaxial conducting

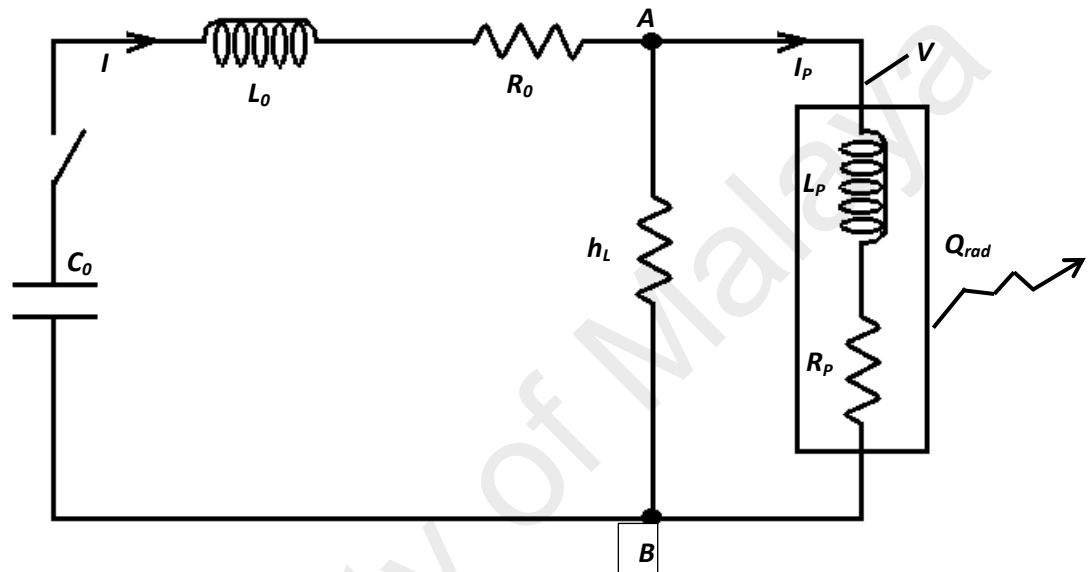


Figure 2.6: Equivalent circuit structure of the plasma focus [121].

tube with height z , outer radius b , and inner radius a .

The induced magnetic field between the electrode is

$$B_0 = \frac{\mu}{2\pi} \times \frac{I_P}{r} \quad (2.10)$$

Where $I_P = f_c I$ is the current through the plasma, and f_c is a current shedding factor.

The resulting $\mathbf{J} \times \mathbf{B}$ force on the plasma sheath is directed axially upward to the open end of the anode.

The force exerted by the magnetic piston to drive the plasma sheath is

$$F_{Z1} = \int_a^b I_P \times \frac{\mu I_P}{2\pi r} dr = \frac{\mu I_P^2}{2\pi} \ln\left(\frac{b}{a}\right) \quad (2.11)$$

The tube inductance is

$$L_{P1} = \frac{\mu}{2\pi} z \ln\left(\frac{b}{a}\right) \quad (2.12)$$

By substituting this expression into the general circuit equation (2.8), the circuit equation for the axial phase is

$$\frac{dI}{dt} = \frac{V_0 - \frac{1}{C_0} \int_0^t I dt - (R_0 + f_c R_P) I - \frac{\mu}{2\pi} f_c I \ln\left(\frac{b}{a}\right) \frac{dz}{dt}}{L_0 + \frac{\mu}{2\pi} f_c z \ln\left(\frac{b}{a}\right)} \quad (2.13)$$

2.5.2.2 The Radial Phase

Figure 2.5(b) shows that the current flows through the anode (radius a , height z_0), plasma slug (radius r_p , height z_f), plasma sheath ($r_p \rightarrow b$ at position z_f), and back to cathode (radius b) in the radial phase. The induced magnetic field can also be expressed by Equation 2.3.

The $\mathbf{J} \times \mathbf{B}$ force on the plasma slug directed radially inwards is given by

$$F_{r2} = \int_0^{z_f} I_p \times \frac{\mu I_p}{2\pi r_p} dz = \frac{\mu I_p^2 z_f}{2\pi r_p} \quad (2.14)$$

This force is exerted by the magnetic piston compressing the plasma slug. The force on the plasma sheath that connects the slug to the cathode pointing axially upwards is written as follows:

$$F_{z1} = \int_{r_p}^b I_p \times \frac{\mu I_p}{2\pi r} dr = \frac{\mu I_p^2}{2\pi} \ln\left(\frac{b}{r_p}\right) \quad (2.15)$$

The entire plasma inductance is composed of two parts, namely, the conductive cylinder of the electrodes of height z_0 and the plasma slug of height z_f and outer radius r_p .

$$L_{P2} = \frac{\mu}{2\pi} \left[z_0 \ln\left(\frac{b}{a}\right) + z_f \ln\left(\frac{b}{r_p}\right) \right] \quad (2.16)$$

From equations (2.16) and (2.8), the circuit equation for the radial phase as follows:

$$\frac{dI}{dt} = \frac{V_0 - \frac{1}{C_0} \int_0^t I dt - (R_0 + f_c R_p) I + \frac{\mu}{2\pi} f_c I \left[\frac{z_f}{r_p} \frac{dr_p}{dt} - \ln\left(\frac{b}{r_p}\right) \frac{dz_f}{dt} \right]}{L_0 + \frac{\mu}{2\pi} f_c \left[z_0 \ln\left(\frac{b}{a}\right) + z_f \ln\left(\frac{b}{r_p}\right) \right]} \quad (2.17)$$

2.5.3 Plasma Resistance

The plasma resistance in our plasma focus devices can be expressed by Spitzer [122] using Spitzer's resistivity.

$$\eta = 1.033 \times 10^{-4} \times \ln \Lambda \times \frac{Z_{eff}}{(T_{eV})^{3/2}} \quad (\Omega \cdot m) \quad (2.18)$$

where, $\ln \Lambda = 29.27 + 1.5 \ln T_{eV} - 0.5 \ln[(1 + Z_{eff}) \times N_i]$, T_{eV} is the plasma

temperature expressed in eV , N_i is the plasma ion density and Z_{eff} is the effective ionic charge.

Therefore, the Spitzer resistance of the plasma slug during the radial phase is obtained using Equations (2.17) and (2.18):

$$R_{slug} = \frac{1.033 \times 10^{-4} \times \ln \Lambda \times Z_{eff}}{(T_{eV})^{3/2}} \times \frac{z_f}{\pi (r_p^2 - r_s^2)} \quad (2.19)$$

where r_s is the inner radius of the plasma slug.

The current is uniformly flowing in the slug, although it should be concentrated on the slug surface because of the skin effect. The surface effect

thickness is estimated to be $\delta \sim \sqrt{\frac{2\eta}{\mu\omega}}$.

2.5.4 Energy and Temperature of the Plasma in Plasma Focus

There is the following description in detail:

2.5.4.1 Mechanisms of Energy Transfer into the Plasma and Plasma Tube

The whole energy comes from the electrical energy stored initially in the energy bank in the plasma focus system, which is written as follows:

$$E_{total} = \frac{1}{2} C_0 V_0^2 \quad (2.20)$$

The tube voltage is expressed by equation (2.9), the power input into the whole plasma system is

$$P_{total} = I_P V = I_P L_P \frac{dI_P}{dt} + I_P^2 \left(R_P + \frac{dI_P}{dt} \right) \quad (2.21)$$

The energy stored in the tube inductance is $\frac{1}{2}L_p I_p^2$, the power transferred into plasma is;

$$P_{plasma} = P_{total} - \frac{d}{dt} \left(\frac{1}{2} L_p I_p^2 \right) = I_p^2 \left(R_p + \frac{1}{2} \frac{dL_p}{dt} \right) \quad (2.22)$$

Equation (2.22) presents the two terms. The first term is induced apparently by the joule heating that heats the plasma directly. The second term is the power contributed to the system dynamics, such as kinetic energy, thermal energy, and ionization energy. The term $\frac{1}{2} \frac{dL_p}{dt}$ is a form of plasma dynamic resistance [119].

Therefore, the total energy transferred into the plasma is as follows:

$$EINP = \int_0^t I_p^2 \left(R_p + \frac{1}{2} \frac{dL_p}{dt} \right) dt \quad (2.23)$$

From equation (2.12), (2.16) and equation (2.23), EINP is written as follow:

$$\text{Axial Phase: } EINP_1 = \int_0^t I_p^2 \left(R_p + \frac{\mu}{4\pi} \ln \left(\frac{b}{a} \right) \frac{dz}{dt} \right) dt \quad (2.24)$$

$$\text{Radial Phase: } EINP_1 = \int_{t_{20}}^t I_p^2 \left(R_p + \frac{\mu}{4\pi} \ln \left(\frac{b}{r_p} \right) \frac{dz_f}{dt} - \frac{\mu}{4\pi} \frac{z_f}{r_p} \frac{dr_p}{dt} \right) dt \quad (2.25)$$

Where t_{20} is the initial radial phase time.

The work performed is calculated by the magnetic piston. The force on the plasma sheath in the axial phase is expressed in Equation (2.11), which is in the Z-direction. The work performed W_1 by the axial magnetic piston F_{z1} is as follows:

$$W_1 = \int_0^z F_{z1} dz = \int_0^z \frac{\mu I_p^2}{2\pi} \ln \left(\frac{b}{a} \right) dz = \int_0^t I_p^2 \frac{dL_{p1}}{dt} dt \quad (2.26)$$

Similarly, the work performed in the radial phase is given by F_{z2} and F_{r2} from equations (2.14) and (2.15).

$$W_2 = \int_0^{z_f} F_{z2} dz_f + \int_0^{r_p} F_{r2} dr_p = \int_{t_{20}}^t \frac{\mu I_p^2}{2\pi} \left(\ln\left(\frac{b}{r_p}\right) \frac{dz_f}{dt} + \frac{z_f}{r_p} \frac{dr_p}{dt} \right) dt$$

$$W_2 = \int_{t_{20}}^t I_p^2 \frac{dL_{P2}}{dt} dt \quad (2.27)$$

Comparing equation (2.23) with equations (2.26) and (2.27), the second EINP term in equation (2.23) is only half of the work performed by the magnetic piston, whereas the other half is stored in the tube inductance. Therefore, the two mechanisms for energy coupling into plasma are joule heating and magnetic piston.

The magnetic piston pushes the plasma in both the axial and the radial directions in the radial phase. Only the radial direction is of interest because the radial compression finally develops the plasma slug into a hot and dense plasma column.

The radial work is considered to be the energy into plasma slug when comparing equation (2.25) and (2.27).

$$EINP_{slug} = \int_{t_{20}}^t I_p^2 \left(R_{slug} - \frac{\mu}{4\pi} \frac{z_f}{r_p} \frac{dr_p}{dt} \right) dt \quad (2.28)$$

This expression is identical with that derived by S. Lee [119].

2.5.4.2 Driving Parameter

The concept of driving parameter was proposed [103, 123] to describe the intensity of the driving force in plasma focus. The driving parameter S is nearly

constant at $90 \text{ kA}/(\text{cm.torr})^{1/2}$ for the optimized operation of deuterium over a wide range of machines, from a small machine (50 J) to a large machine (1 MJ) [103]. The driving parameter is defined as

$$S = \frac{I/a}{\sqrt{\rho}} \quad (2.29)$$

This parameter has been observed experimentally to be a measure of speed, which has an optimum value for each working gas. It can also be a measure of the drive magnetic pressure per unit density or drive magnetic energy per unit mass, i.e., $P_B = \frac{1}{2\mu} \left(\frac{\mu I_p}{2\pi r_p} \right)^2$.

Therefore, any model based on either the snowplow or slug model will have the driven speeds primarily dependent on the factor S . Quickly estimating the plasma state or required working condition in plasma focus, as well as any other EM-driven plasma system, is a valuable parameter.

Equation (2.22) deduces the drive parameter from the energy input viewpoint. The discharge current is constant in the radial phase, and the energy input by joule heating is omitted. The energy in the radial phase can be estimated as follows:

$$EINP_2 \sim \frac{1}{2} I_p^2 \int_{t_{20}}^t dL_p = \frac{1}{2} L_{p2b} I_p^2 = \frac{\mu}{4\pi} I_p^2 z_f \ln \left(\frac{b}{r_p} \right) \quad (2.30)$$

where L_{p2b} is the plasma slug inductance, which is the second term in equation (2.16).

The energy in the plasma slug can be considered as a certain portion of $EINP_2$ given that, other part is stored in the plasma sheath. The mass in the column is measured by $a^2 z_f$. Thus the energy per unit mass in the final plasma

column can be expressed as follows:

$$\frac{EINP_{slug}}{mass} \sim const \times \frac{\frac{\mu}{4\pi} I_p^2 z_f \ln\left(\frac{b}{r_{min}}\right)}{\rho \pi a^2 z_f} \sim const2 \times \frac{I^2}{\rho a^2} = const2 \times S^2 \quad (2.31)$$

where r_{min} is the final column radius. Here $\ln\left(\frac{b}{r_{min}}\right)$ varies at a very slow rate compared to a^2 , and can be considered constant.

Equation (2.31) clearly shows that the drive parameter can be directly correlated with the energy density in the final plasma column. Therefore, the current can be increased or decrease the anode radius and gas pressure to increase the energy density (and consequently the plasma temperature).

2.5.4.3 Energy Transfer Process

The plasma focus energy balance is very important in its behavior analysis. The energy goes into the plasma focus tube by three ways: inductive impedance, piston work, and joule heating.

The inductive impedance represents the change in the energy stored in L_p by the change in the discharge current. The piston work is the main path to transfer energy into the plasma focus tube. Half of the piston work is increased by pushing the conductive plasma sheath, which then increases the energy stored in L_p . The other half converts into plasma energy. Joule heating is induced by the plasma resistance R_p and its current flow. This process directly heats the plasma.

The energy stored in the tube inductance E_l is determined by both the inductance and current. Notably, this energy is not dissipative; if the current drops, it acts as an energy source to the output energy.

The energy in the EINP plasma is composed of two parts, namely, joule heating and half of the piston work. Plasma energy exists in four forms: kinetic energy E_k , internal energy U , ionization and excitation energies E_i and E_x , respectively, and radiation energy Q_{rad} .

The plasma temperature can be calculated from its internal energy by using all the values of energies in the plasma as follows:

$$T = \frac{U}{\frac{5}{2}Nk} = \frac{EINP - E_k - E_i - Q_{rad} - E_x}{\frac{5}{2}(1+Z_{eff})N_{ion}k} \quad (2.32)$$

If the piston pressure changes, then $P_p = P_p(t)$ and the parameters in the shocked gas region also change with time and location (Figure 2.5b). The pressure, density, and temperature of the shocked gas as a function of location and time should be written as $P(x, t)$, $\rho(x, t)$, and $T(x, t)$, respectively.

Assuming that the signal of the changing P_p propagates in the shocked gas region with a speed C_s (sound speed in the gas), then the transmission time from piston to shock front is $t_{p-s} = \frac{(x_p - x_s)}{C_s}$, where the sound speed in the gas can be calculated.

$$C_s = \sqrt{\frac{\gamma(1+Z_{eff})kT}{m_i}} \quad (2.33)$$

If the time scale is comparable with the changing piston speed, the effect of changing piston pressure must be considered for calculation.

The plasma temperature is evaluated using equations (2.32) and (2.33).

2.5.5 Simulation using UM-DPF2 Parameters

Simulation using UM-DPF2 parameters are given below:

2.5.5.1 Numerical Calculation Method

The plasma focus behavior is numerically computed based on the equations presented in previous sections.

A simple linear approximation integration method [121], is used to calculate all variables by small time steps. The parameter values at a series of time points $t_1, t_2, t_3, t_4, \dots$ with an increment Δt are calculated according to the equations.

The values of variables in the differential equations (i.e., z, z_f, r_s, r_p, r_r) at time t are related to the previous corresponding values at time $t - \Delta t$ as (such as for the current I). Thus:

$$I(t) = I(t - \Delta t) + \frac{dI}{dt}(t - \Delta t) \times \Delta t \quad (2.34)$$

where Δt is the time increment for calculation.

The value $\frac{dI}{dt}(t - \Delta t)$ is calculated by the circuit equation. The values of the discharge current and plasma dimension parameters can be obtained in this manner. The other plasma parameters (i.e., N_{ion}, T_{ev} , and $EINP$ etc.) are calculated by these solved values accordingly.

The axial phase ends at $z = z_0$ when the plasma sheath reaches the anode top. The radial phase then starts at:

$$r = r_p = a, z_f = 0 \quad (2.35)$$

The initial values of the other parameters such as $\frac{dI}{dt}$ are taken as the final

values at the end of the axial phase. The reflected shock begins when $r_s = 0$ and inherits all the parameters from the radial phase. Similarly, the slow compression phase starts when $r_r = r_p$ and inherits the parameters from the reflected shock phase.

2.5.5.2 Parameters for UM-DPF2

This model is applied to simulate the performance of the UM-DPF2 plasma focus machine. The simulation parameters for our machine are fixed as follows:

$$f_m = 0.017; f_{mr} = 0.16; f_c = 0.7; f_{cr} = 0.7 \quad (2.36)$$

where, f_m is the mass factors for the axial phase,

f_{mr} is the mass factor for the radial phases,

f_c is the current shedding factor, and

f_{cr} is reflected shock factor.

The model presented in this chapter gives a basic understanding of the plasma focus.

EXPERIMENTAL SETUP AND DIAGNOSTICS

3.1 Introduction

This chapter reports about the experimental setup and the diagnostics. Measurements are performed on the radiation emission (X-ray) and electron beams emitted from the plasma focus by employing various diagnostics.

3.2 Setup of the Plasma Focus Device

The Mather-type plasma focus device was energized by a single 30 μF , 15 kV Maxwell capacitor. A maximum available energy to of 3.4 kJ/shot was necessary to create a plasma in the vacuum chamber. The capacitor was charged up to 12 kV because charges beyond the peak value may damage this device. The energy available to create plasma was 2.2 kJ/shot; the peak current obtained was 140 kA. The proposed plasma focus device comprised the following sub-systems:

- i. vacuum chamber and vacuum system
- ii. electrode system
- iii. energy storage and transfer system
- iv. damping system

3.3 Parameters of UM-DPF2 Device

Tables 3.1 and 3.2 respectively summarize the design and experimentally measured parameters of the UM–DPF2.

The schematic of 2.2 kJ plasma focus device is shown in Figure 3.1. The discharge tube comprised a copper electrode. The inner electrode was a hollow cylinder (diameter, 1.9 cm; effective length, 18 cm) and functioned as the anode. The selection of the hollow anode was attributed to the studies of electron beams in plasma focus device. The outer electrode was composed of six copper rods that formed a squirrel cage (inner diameter, 3.2 cm).

The length of the individual cathode rod was 27 cm. The length of the cathode rod was 9 cm higher than that of the anode rod. A Pyrex glass was used as the insulator to separate the hollow anode and cathode. The vacuum system comprised a rotary van pump and an evacuated chamber with a pressure of less than 10^{-2} mbar; this pressure was used in some published experiments. The chamber was refreshed after every shot to reduce gas contamination with impurities on the output radiation. Fresh Ar gas was refilled to the desired pressure.

Identical coaxial cables (length, 110 cm) were used for all electrical diagnostics. All coaxial cables were protected with aluminum foil to reduce the effects of electromagnetic noises on the data signals. Two DPO4043 digital storage oscilloscopes were used to record all electrical signals from the Rogowski coil, high voltage probe, five channel PIN diode, and the energetic electron beam through the Faraday cup. The oscilloscope was simultaneously triggered for all electrical signals. The five channel PIN diode detectors were normalized against each other by masking with identical aluminized Mylar foils (thickness, 23 μm). The PIN diode response ranged between 1keV and 30 keV. Filter combinations were used to determine the different spectral windows.

Table 3.1: Design parameters with applied specification of the UM-DPF2 device.

Components	Diameter (cm)	Length (cm)	Material
Vacuum Chamber	14.25 / 14.50 (O.D/I.D)	61.50	Stainless steel
Hollow Anode	1.90 / 1.60 (O.D/I.D)	18.00	copper
Cathode Rod	0.95	27.20	copper
Insulator sleeve	2.00	5.00	Pyrex
Target	1.50	0.35 (width)	Lead

Table 3.2: Experimentally measured parameters of the UM-DPF2 device.

Parameter	Symbol and unit	Specification
Charging Voltage	V_o (kV)	12
Capacitance	C_o (μ F)	30
Stored Energy	E (J) [$= \frac{1}{2} C_o V_o^2$]	2160
Inductance	L_o (nH) [$= \frac{T^2}{4\pi^2 C_o}$]	165
Impedance	Z_o (m Ω) [$= \sqrt{\frac{L_o}{C_o}}$]	74
Peak Current Discharge	I_o (kA) [$= \frac{\pi C_o V_o (1+f)}{T}$]	140
Resistance of Electric Circuit	R_o (m Ω) [$= -\left(\frac{2}{\pi}\right) (\ln f) \left(\frac{L_o}{C_o}\right)^{1/2}$]	14

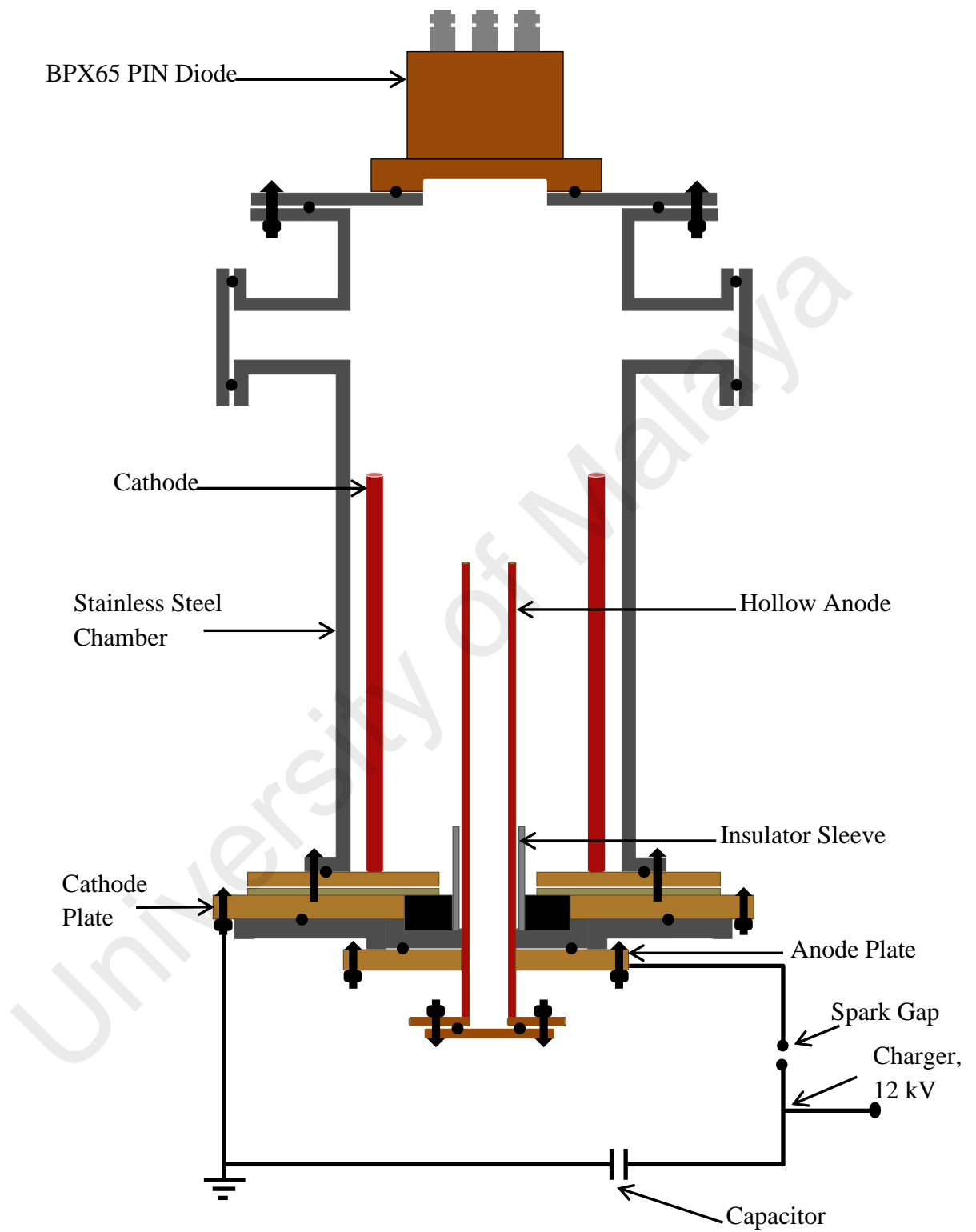


Figure 3.1: Schematic of plasma focus device.

The UM-DPF2 device was powered by a single 30 μF Maxwell capacitor charged to 12 kV. The other sub-systems of this device included the control electronics and diagnostic systems (Figure 3.2).

3.4 Plasma Diagnostic Techniques

Several diagnostic experiments were performed to elucidate the discharge characteristics, investigate the radiation and the electrons emitted from the plasma focus, and monitor the EM parameters of this device. High voltage probe and Rogowski coil were used to monitor the voltage across the electrodes and the discharge current, respectively.

3.4.1 High Voltage Probe

The high voltage (HV) probe is a resistive divider used to measure the transient voltage across the electrodes [124, 125]. This probe comprised low inductance resistors, 10 pieces of 560 Ω resistors in series with a 51 Ω shunting resistor at the end of the chain; the power rating for each resistor was 1 W. The resistors were placed in polyethylene tubing. The resistors allowed a large power overload when the HV probe was created from the low inductance resistors. The probe system was enclosed in a copper tube (diameter, 0.5 inch) at a ground potential. This probe was mounted across the anode and cathode plates at the outer back wall of the focus tube. The output of the high voltage probe was reduced by 10 \times attenuator connected to the oscilloscope input. Figure 3.3 shows the schematic diagram of a typical HV probe. A high voltage of about 100 kV was developed because of the rapid changes in

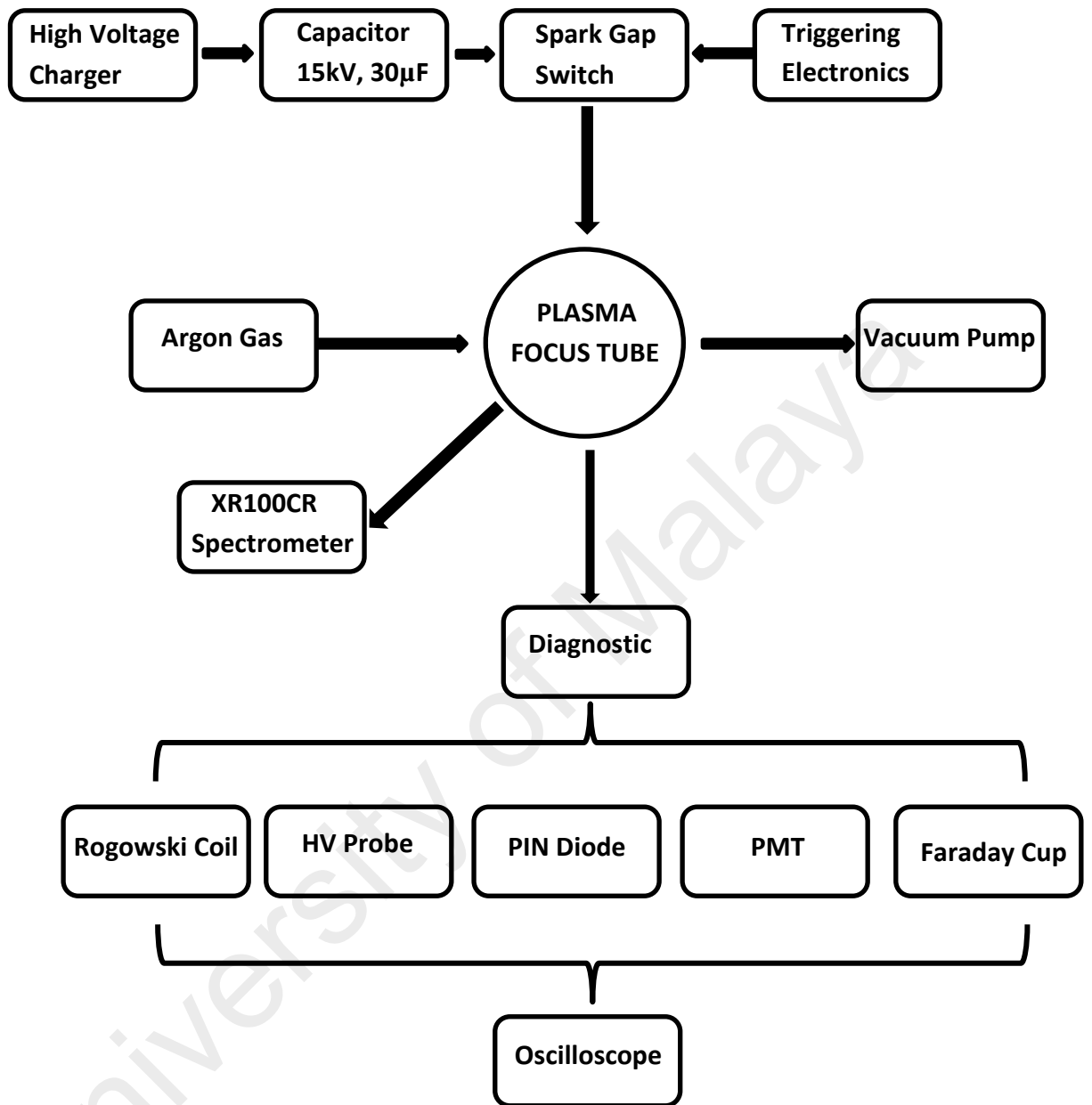


Figure 3.2: Block diagram of the experimental setup.

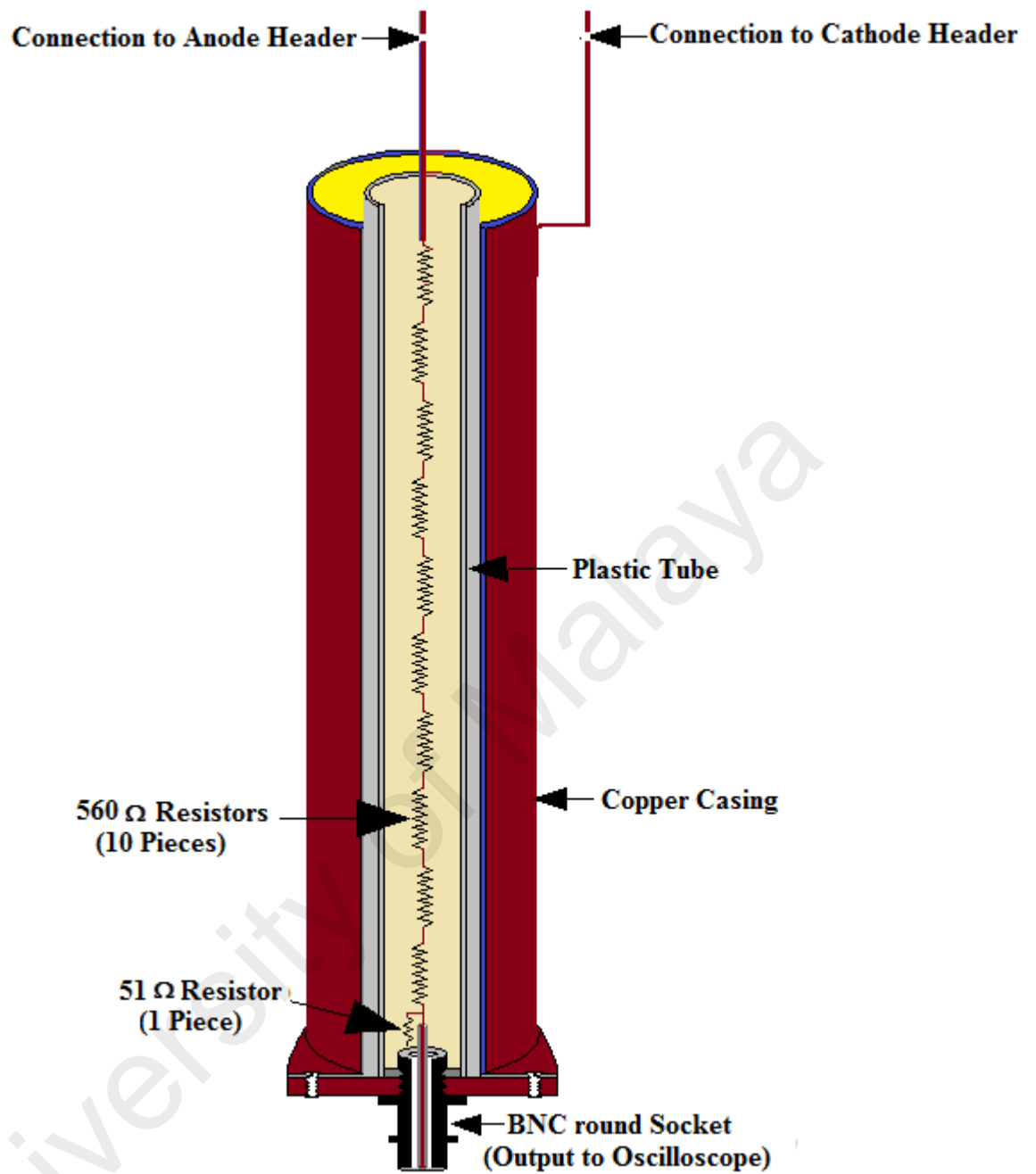


Figure 3.3: Schematic diagram of a typical high voltage probe.

the inductance when the CS radially collapsed beyond the face of the central electrode. The voltage was several times higher than that during charging, which could not be measured by any conventional voltage measuring equipment. However, the HV probe could be employed to record the transient high voltage. The resistor dividers are usually used because of their simplicity in design and fabrication. These dividers were constructed for to measure the voltage of the plasma focus device. The errors in resistors were less than 5 %, and the estimated time response ranged from 15 ns [126] to 20 ns [127]. The errors were primarily associated with the resistor quality; however, these errors were within reasonable ranges and acceptable limits.

Safety measures should be considered during the use of HV probe in the plasma focus. The oscilloscope should not be directly placed in series with the high-resistance resistors. The first resistor should be parallel with the oscilloscope and the ground. Dangerous shock hazards could be avoided if the connection to the oscilloscope was open; this case was similar to that of the scope arranged in series.

3.4.2 Rogowski Coil

The main discharge current was measured with a Rogowski coil or Rogowski belt [128, 129]. This coil is a multi-turn and toroidally bent solenoid used to measure the current flowing through the inner toroidal surface. The basic design of the Rogowski coil is shown in Figure 3.4.

When HV is applied across the electrodes, discharges are obtained along the surface of the insulator sleeve. During this period, the internal resistance of the system becomes very small, and high discharge currents (few hundred kA to MA) are passed through the device. These currents could not be measured by using the conventional

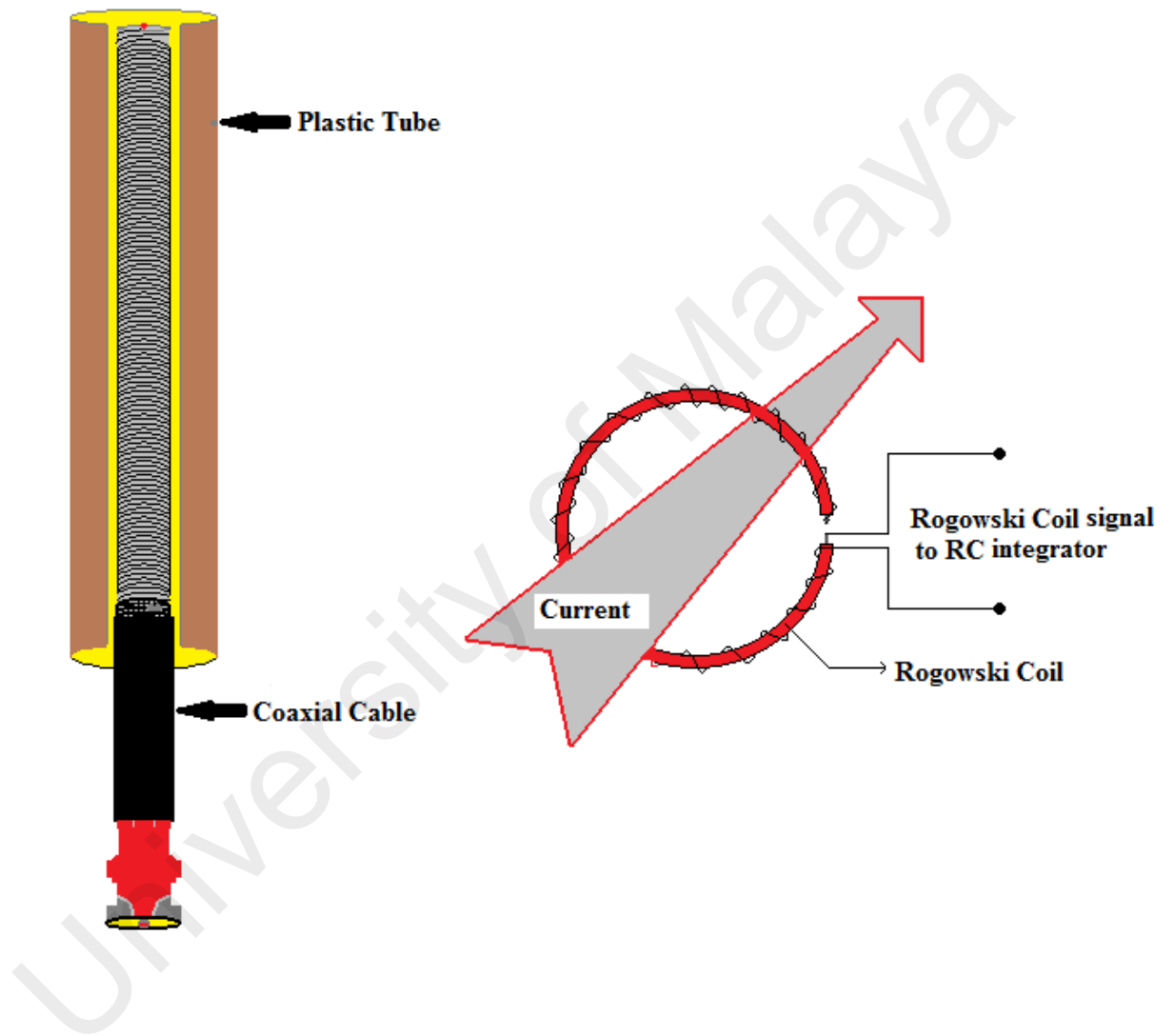


Figure 3.4: A schematic diagram of the Rogowski coil.

measuring equipment. Indirect techniques have been introduced to solve this problem. The Rogowski coil effectively measures high currents. This coil works based on Faraday's law of electromagnetic induction and comprises an air cored toroidal coil placed around the current-carrying conductor. The time-dependent magnetic field produced by variations in the current induces a voltage in the coil, which is proportional to the rate of change of current. The coil-integrator combination is a versatile current-measuring system.

The Rogowski coil was selected over the common current transformer because this coil exhibits open-ended production, flexibility, the absence of restrictions in the position, direction, and current sense.

Furthermore, the Rogowski coil can be used as a current transformer. This coil was terminated with a low inductance resistor r (resistance, $\sim 0.1 \Omega$). Figure 3.5 shows the equivalent circuit, where L_c , I , and i are the coil inductance, discharge current, circuit current through the coil, respectively. Specific criteria were imposed to ensure that the diagnostic tool was at a sufficient high resolution and determine the rapidly changing current.

From the equivalent circuit, the circuit equation can be written as

$$\frac{L\phi}{dt} = k \frac{dI}{dt} \quad (3.1)$$

$$\text{or } L_c \frac{di}{dt} + i (r + r_c) = k \frac{dI}{dt} \quad (3.2)$$

Where, i is the induced current in the coil and I is the discharge current.

(a) When $L_c \frac{di}{dt} \gg i (r + r_c)$, Then $L_c \frac{di}{dt} = k \frac{dI}{dt}$, by integration,

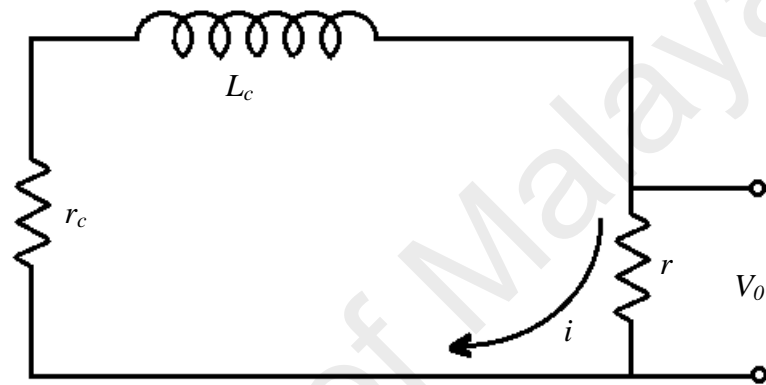


Figure 3.5: Equivalent circuit of the Rogowski coil.

$$L_c \int \frac{di}{dt} dt = k \int \frac{dI}{dt} dt \quad (3.3)$$

$$L_c \int di = k \int dI \quad (3.4)$$

$$L_c i = k I \Rightarrow i = \left(\frac{k}{L_c}\right) I \quad (3.5)$$

Therefore, the output voltage across the terminal can be written as

$$V_o(t) = i r \quad (3.6)$$

Thus, using the equation (3.5) into the equation (3.6), we have

$$V_o(t) = \left(\frac{k}{L_c}\right) I r = \left(\frac{kr}{L_c}\right) I \quad (3.7)$$

$$V_o(t) = KI \quad (3.8)$$

where $K = \left(\frac{kr}{L_c}\right)$

$$V_o(t) \propto I \quad (3.9)$$

Eq. (3.9) implies that the potential difference $V_o(t)$ across the small resistor r is directly proportional to the discharge current through the coil. The constant factor K was determined by calibrating the Rogowski coil.

For the Rogowski coil to efficiently perform as a current transformer, the expression $\frac{L_c}{(r+r_c)}$ should be higher than the duration of the current pulse.

$$(b) \text{ when } L_c \frac{di}{dt} \ll i(r+r_c),$$

then,

$$i(r+r_c) = k \frac{dI}{dt} \Rightarrow i = \left(\frac{k}{(r+r_c)}\right) \frac{dI}{dt} \quad (3.10)$$

So, the output voltage across the terminal can be written as (using equation (3.6)), we have

$$V_o(t) = \left(\frac{k}{(r+r_c)} \right) r \frac{dI}{dt} = \left(\frac{rk}{(r+r_c)} \right) \frac{dI}{dt} \quad (3.11)$$

In this case, the Rogowski coil could be used to measure $\frac{dI}{dt}$, in which $\frac{L_c}{(r+r_c)}$ must be lower than the duration of the current pulse.

The Rogowski coil is strongly sensitive to electromagnetic radiation because of its open-ended design. The noise shield in the coil can be used to avoid signal disturbances.

Calibration of the Rogowski coil: The Rogowski coil was calibrated in situ. The plasma focus system was operated at an Ar gas pressure of 25 mbar. The measured current waveform resembled that of an under damped LCR discharge. Hence, the sinusoidal characteristic of the current signal and amplitude decay with time.

The sensitivity of the Rogowski coil was calibrated using a damped sinusoidal LCR discharge circuit; this circuit was obtained by firing the plasma focus device at 25 mbar Ar gas. The first peak of the discharge current I_o could be determined as follows [97]:

$$I_o = \frac{\pi C_o V_o (1+f)}{T} \quad (3.12)$$

Using this equation (3.12), the peak current values can be estimated if the charging voltage of the capacitor is known.

We know that the angular frequency is given by equation

$$\omega = 2\pi f = \frac{1}{\sqrt{L_o C_o}} \quad (3.13)$$

$$T = \frac{1}{f} = \frac{2\pi}{\omega} \quad (3.14)$$

$$\Rightarrow T = 2\pi\sqrt{L_o C_o} \quad (3.15)$$

Where, T the time period of the waveform is observed on the oscilloscope.

Figure 3.6 illustrates the typical current waveform for a plasma focus discharge.

From T measurements based on this waveform:

$$f = \frac{1}{4} \left(\frac{V_5}{V_4} + \frac{V_4}{V_3} + \frac{V_3}{V_2} + \frac{V_2}{V_1} \right) \quad (3.16)$$

Reversal ratio of the current = f , (is always less than unity)

Capacitance of capacitor bank = C_o

Periodic time of the current waveform = $T = \frac{1}{2}(T_1 + T_2)$

Initial charging voltage = V_o

For instance,

$$f = \frac{1}{4} \left(\frac{V_5}{V_4} + \frac{V_4}{V_3} + \frac{V_3}{V_2} + \frac{V_2}{V_1} \right)$$

$$C_o = 30 \mu F$$

$$T = \frac{1}{2}(T_1 + T_2) = 14 \mu s$$

$$L_o = \frac{T^2}{2\pi^2 C_o} = 165 nH$$

$$V_o = 12 kV$$

$$I_o = 140 kA$$

$$K = 16.09 kA/V$$

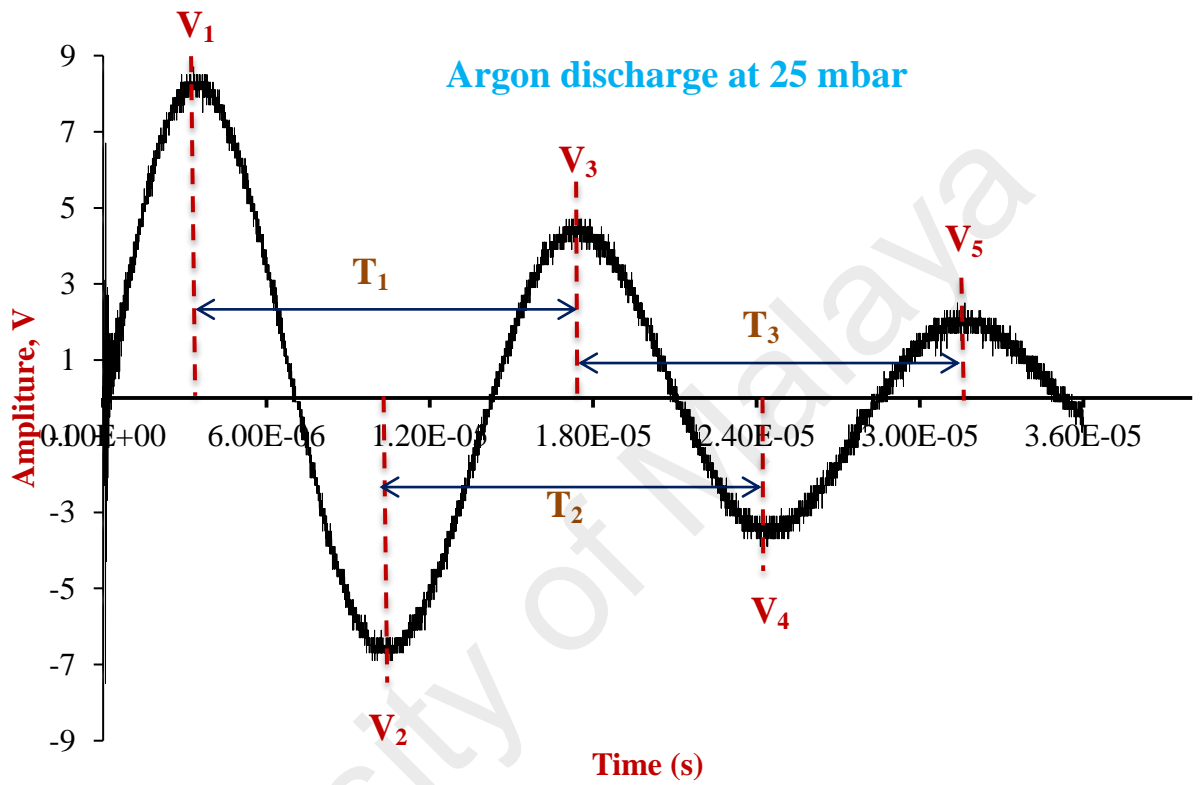


Figure 3.6: Typical short circuit signal (25 mbar Argon discharge).

From the calculated I_o [Eq. (3.12)] and V_o from the current oscillogram (Figure 3.6), the calibration factor or coil sensitivity is given by Eq. (3.17):

$$K = \frac{I_o}{V_o} \text{ Amp./Volts} \quad (3.17)$$

The calibration factor for the derivative-type Rogowski coil was found to be $(16 \pm 0.1) \text{ kA/V}$.

3.4.3 The PIN Diode Detector

Various types of semiconductor diodes were available to detect the radiation. BPX 65 silicon PIN diodes were used to detect X-rays. The typical parameters of this diode are shown in Table 3.3.

Experimental techniques and instruments should be employed during PF discharge to diagnose the radiations that were naturally emitted from the plasma. X-ray emissions were observed by the BPX 65 PIN diodes because of their simplicity in installation, fast response, and high sensitivity to measure the pulsed radiations between 1 keV and 30 keV [130].

The PIN diode was similar that of PN junction with an additional lightly doped intrinsic silicon layer in the region between heavily doped p - and n -type semiconductors. The n -type region or the 'dead layer' is maintained at ground potential and used as the entrance window of the diode. Each diode was reversed biased as a photo detector, where the p -type layer was maintained at a negative potential with respect to the n -type layer.

Table 3.3: The typical parameters of the BPX 65 PIN diode.

Effective detection area	1 mm^2
Intrinsic Si wafer thickness (estimated)	$\sim 10 \text{ }\mu\text{m}$
Dead layer thickness (estimated)	$\sim 0.5 \text{ }\mu\text{m}$
Rise time (typical)	0.5 ns

The PIN diode fails to conduct under reversed bias. However, when the diode absorbs an X-ray photon of energy equal or more to form an electron–hole pair in the intrinsic layer, one or more of these pairs are created and result in charge flow in the biasing circuit.

An average energy of 3.55 eV is necessary to form an electron–hole pair for the case of silicon at room temperature [131]. Every joule of X-ray energy absorbed in the intrinsic layer results in a charge flow of about 0.282 C.

The original diode was enclosed in a TO-18 casing with a glass window, which is removed to detect the X-rays. The *p*-type layer of the PIN diode was maintained at a negative potential -45 V with respect to the *n*-type layer at ground potential. Two dry cells (voltage, 22.5 V) were used to provide the reverse bias voltage. Fig. 3.7 shows the PIN diode setup with a biasing circuit. The blocking capacitor (capacitance, 0.047 μ F) and the resistor (resistance, 51 Ω) were placed in an RS in-line module case with BNC connectors. The inputs and outputs were directly connected to the diodes and DPO4043 digital storage oscilloscope, respectively.

An array of five windowless BPX 65 PIN diodes (labeled D1 to D5) was used to monitor the temporal and spectral profiles of the X-rays. These diodes were glued on five holes on a circular brass flange (diameter, 7 cm; thickness, 5 mm) with one of the diodes at the flange center. Each diode was vacuum tightened by mounting the circular brass plate onto a cylindrical brass casing with an O-ring to reduce the attenuation of X-rays through the ambient gas from reaching the diode. The casing contained five BNC-free sockets; all the diodes were connected to these sockets via short wires. Figure 3.8 shows the construction of the diode assembly.

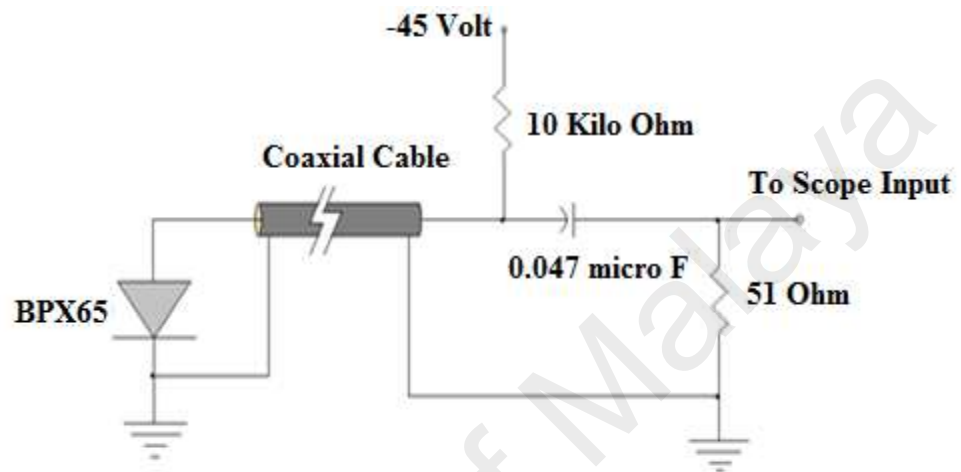


Figure 3.7: Biasing circuit of the BPX65 PIN diode.



Figure 3.8: Design of five PIN diodes.

The array of PIN diodes covered with a suitable set of Ross filters [132-134] provides qualitative information of the X-ray spectra and the estimated plasma temperature [135]. The electron temperature of the plasma can be determined if the detectors are calibrated. Each of the diode is covered with aluminum filters of different thickness (Table 3.4). Subsequently, all the PIN diodes were covered with aluminized Mylar foils of similar thicknesses of 23 μm and exposed to X-ray emission. This procedure was performed to normalize the geometrical differences of the detector caused by the position and sensitivity of each diode with each other.

The diode could suitably detect the X-rays for wavelengths between 0.3 \AA to 10 \AA . Various filter thicknesses were used for the PIN diodes at different channels.

The transmission curves of the BPX 65 PIN diode were attached with the associated absorption filters (Figure 3.9).

The detection efficiencies of the PIN diodes predominantly depend on the X-ray wavelength and filter thickness. The sensitivity of the PIN diode could be expressed as a 2D thickness model as follows [136]:

$$S(\lambda) = 0.282e^{-\mu(\lambda) \cdot x_1} (1 - e^{-\mu(\lambda) \cdot x_2}) A/W \quad (3.18)$$

where, $\mu(\lambda)$ = X-ray mass-absorption coefficient of silicon in cm^2/g

x_1 = Mass thickness of the entrance windows in g/cm^2

x_2 = Effective depletion region of the intrinsic layer in g/cm^2

The first and second exponential terms represent the X-ray transmission through the entrance window (n -type layer) of the PIN diode and the absorption coefficient of the intrinsic layer, respectively.

Table 3.4: An array of five PIN diodes exposed with Al foil + Aluminized Mylar (μm).

PIN diode	Filter	Thickness (μm)
D1	Aluminized Mylar	23
D2	Aluminized Mylar + aluminium	23 + 20
D3	Aluminized Mylar + aluminium	23 + 30
D4	Aluminized Mylar + aluminium	23 + 40
D5	Aluminized Mylar + aluminium	23 + 100

When the X-ray passes through a filter, the absolute monochromatic transmission is presented in Eq. (3.19):

$$T(t, \lambda) = \frac{I(t, \lambda)}{I_0} = e^{-\mu(\lambda)t} \quad (3.19)$$

Where, λ is wavelength of incident X-ray,

$\mu(\lambda)$ is X-ray absorption coefficient of filter,

t is thickness of filter,

I_0 is initial incident intensity and

$I(t, \lambda)$ is intensity transmitted.

The absorption coefficient $\mu(\lambda)$ can be obtained from the standard references [137, 138].

Given the array of five BPX65 PIN diodes, the X-ray spectrum can be analyzed by ratio method to determine the electron temperature of the plasma. The theoretical X-ray transmission ratio through aluminum filters a and b with of different thicknesses was calculated as follows [122a]:

$$R_{theory} = \frac{\int P(\lambda). \exp(-\sum_a \mu_a x_a - \sum_b \mu_b x_b). S(\lambda). d\lambda}{\int P(\lambda). \exp(-\sum_a \mu_a x_a). S(\lambda). d\lambda} \quad (3.20)$$

where, $P(\lambda)$ is the emission from the plasma source. μ_a and μ_b are the mass absorption coefficients, and x_a and x_b are the thicknesses of filters a and b, respectively. $S(\lambda)$ is the practical sensitivity of the PIN diode.

For deuterium plasma with bremsstrahlung X-rays, $P(\lambda)$ is presented by Eq. (3.21):

$$P(\lambda) = 1.9 \times 10^{-28} \frac{N_e N_i z_i^2}{\lambda^2 T_e} \exp\left(\frac{-12395}{\lambda T_e}\right) \quad (3.21)$$

where T_e , N_e , N_i , and z_i are the electron temperature, electron density, ion density, and ion charge state, respectively.

Theoretical transmission ratio R_{theory} for plasma-emitted X-rays at various temperatures can be plotted by repeating the procedure for various filter thickness. The

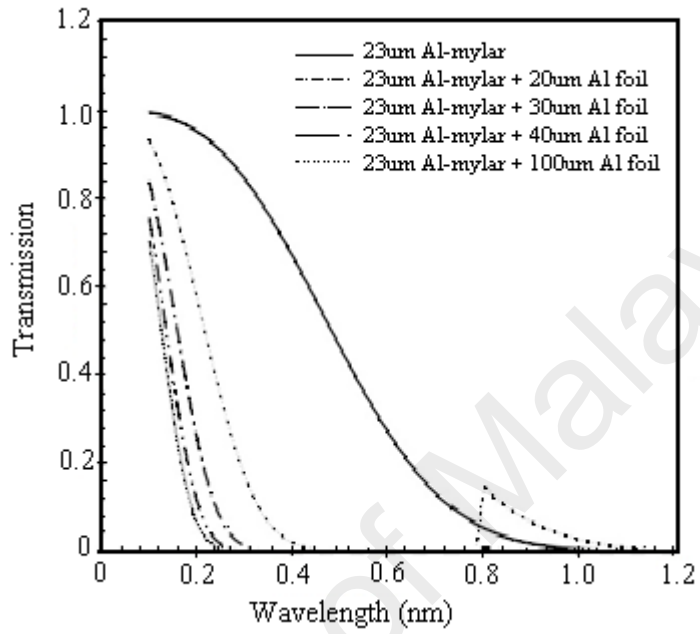


Figure 3.9: Transmission curves of 23 μm Aluminized Mylar, 23 μm Aluminized Mylar + (20 μm , 30 μm , 40 μm , and 100 μm) Al foil.

experimental transmission ratio $R_{exp.}$ over a range of filter thicknesses is computed as follows:

$$R_{exp.} = \frac{S_{a,b}^n}{S_a^1} \cdot k_1^n \quad (3.22)$$

where $S_{a,b}^n$ and S_a^1 are the PIN diode signals collected by the detectors n (filters a and b) and D1 (filter a only), respectively. k_1^n is the normalization factor of detector n with respect to D1, which is obtained by simultaneously calibrating the PIN diode detectors by using 23 μm aluminized Mylar. This parameter accounts for the geometrical differences of the detectors and the intrinsic sensitivity of each diode.

The X-ray line radiations or the plasma temperature can be deduced by plotting $R_{exp.}$ of the X-ray emission from the PF against the thickness of the aluminum filter and comparing the corresponding result with those of R_{theory} . Figure 3.10 plots R_{theory} of the X-rays against the thickness of aluminum filter for Cu- K_α and Cu- K_β lines and plasma temperatures ranging from 1 keV to 10 keV.

3.4.4 The X-ray Spectrometer

Spectrometers determine the properties of light over a specific portion of the EM spectrum, identify materials, as well as produce spectral lines and measure their wavelengths and intensities. X-ray spectrometer is used to obtain the spectrum of X-ray image produce by the electron beam target. Since electron beam is energetic, it is enough to induce the $K\alpha$ lines to a rough estimate of electron beam energy. We use to see X-ray spectrum from target by the bombardment of energetic electron beam emission for possible energy. XR100CR X-ray spectrometer was used to analyze the obtained X-ray spectra. This instrument functions as a preamplifier, and cooler system that uses a thermoelectrically cooled Si-PIN photodiode as an X-ray detector.

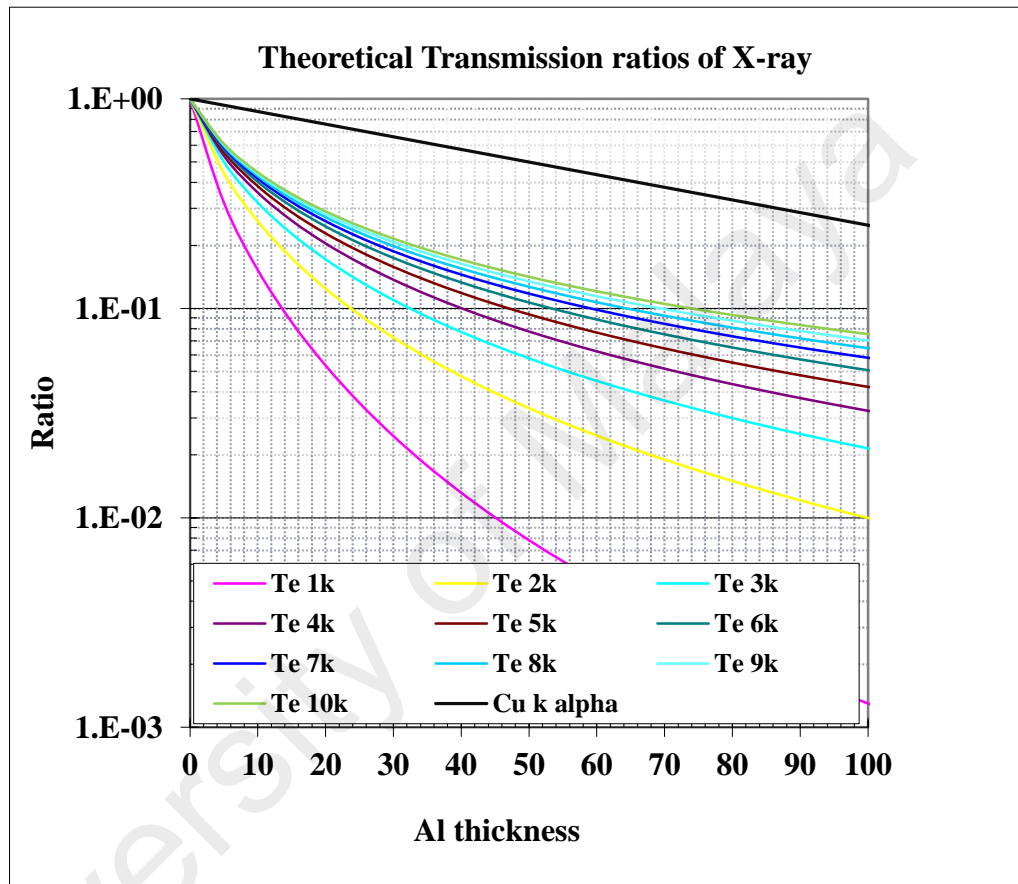


Figure 3.10: Theoretical transmission ratios of X-ray as a function of the aluminum filter thickness for temperature of 1 keV to 10 keV. The transmission ratio of Cu-K_α is also shown.

The spectrometer was operated by the PX2CR AC power supply, which includes a spectroscopy grade shaping amplifier. The spectrometer–power supply system ensures stable operation in less than 1 min from power turn-on. The spectrometer performance remains constant for temperatures below $-20\text{ }^{\circ}\text{C}$. The temperature may not be monitored when the spectrometer is operated at room temperature.

The XR100CR spectrometer can be operated in air or in vacuum (pressure, about 10^{-8} Torr). This spectrometer can be vacuum operated as follows:

1. The detector and preamplifier box can be placed inside the chamber. About 1 W of power is required to avoid overheating and heat dissipation, as well as operate the spectrometer. The additional power provides good heat conduction to the chambers walls.
2. The spectrometer can be located outside the vacuum chamber to detect X-rays through a standard O-ring port.

Operational Theory: X-rays interact with silicon atoms to create an average of one electron–hole pair for every 3.62 eV of energy lost. Depending on the energy of the incoming radiation, this loss is dominated by either the photoelectric effect or Compton scattering. The probability or efficiency of the detector to "stop" an X-ray and create electron–hole pairs increases with the thickness of the silicon.

To facilitate the electron/hole collection, a 100 V bias voltage is applied across the silicon. However, this voltage is too high for the room-temperature operation because it causes excessive leakage and breakdown. Since the detector in the XR100CR is cooled, the leakage current is considerably reduced because the detector in the spectrometer is cooled, thereby permitting high bias voltage, decreasing the detector capacitance, and reducing system noise.

The electron–hole pairs that are produced by X-rays and interact with the silicon near the back contact of the detector are slowly collected. Hence, the collected charge is low, the background in the energy spectrum increases, and false peaks are produced. The slow collection of electron–hole pairs are characterized by prolonged rise time. The PX2CR amplifier incorporates a rise time discrimination (RTD) circuit that prevents the pulses from being counted by the multichannel analyzer (MCA).

XR100CR Detector Specifications:

General Specifications:

- Detector type Si-PIN
- Detector size 2.4 x 2.8 mm (7 mm²), standard
- Detector window Be, 1 mil thick (25 μm)
- Silicon thickness 300 μm
- Beryllium window thicknesses 0.3 mil - 7.5 μm
- Background counts <3 x 10⁻³/s, 2 keV to 150 keV
- Total power <1 Watt

Model PX2CR: Power Supply & Shaping Amplifier

General:

- Size 6 x 6 x 3.5 in (15.3 x 15.3 x 8.9 cm)
- Weight 2.5 lbs (1.15 kg)

DC voltages are supplied through a female connector on the PX2CR amplifier to operate the spectrometer. Figure 3.11 shows the multi-conductor cable that connects the amplifier to the XR100CR spectrometer. The output pulse produced by the PX2CR amplifier is optimally applied using the Si–PIN photodiode detectors and directly

connected to the MCA. The pulses are internally and externally connected to the PX2CR amplifier.

3.4.5 Faraday cup

A Faraday cup is used to collect the charged particles (e.g., electrons and ions) and comprises a cylindrical metallic body with a small opening to function as an entrance for the charged particles. When a beam of charged particles enters in the cup, the beam of charged particles is partially reflected; some secondary electrons are emitted by the effect of incident particles. Faraday cups are designed to trap the reflected beam and reabsorb the secondary electrons. The charged particles have low probabilities to escape from the Faraday cup upon entry; hence, almost all the incident particles are recorded.

The sensitivity of the Faraday cup is unsatisfactory to collect low charged particles. For instance, an undetectable current of $\sim 10^{-13}$ A would be generated if $\sim 10^6$ electron/s are collected by the cup.

The accuracies of Faraday cups are affected by the pulses introduced by the noise after the cup is picked up, electron emissions caused by UV and X-rays, and charge accumulation of the insulating material that surrounds the charge collector. Faraday cups should be placed within evacuated chambers because they can gather free charges from the environment. Energetic charged particles (electron energy, ≥ 5 keV; proton energy, ≥ 20 keV) can penetrate through the thin foil, which can be used to cover the Faraday cups and suppress the secondary emissions. The bottom part of the cup

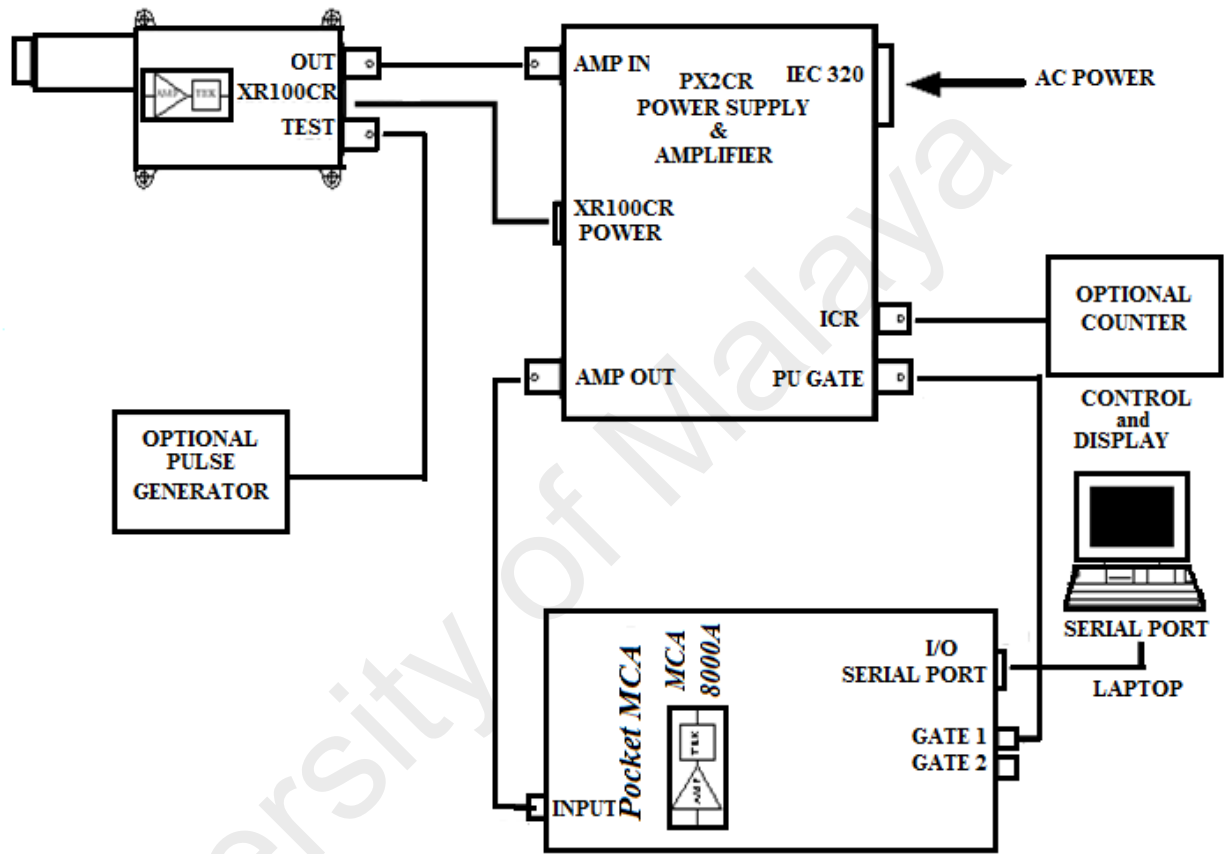


Figure 3.11: XR100CR Connection Diagram.

should be made from materials with low secondary emission yields, such as carbon and beryllium. Upon the entry of the charged particles into the cup, a potential difference is produced between the cup and the ground (or some other level). The potential difference is proportional to the charge on each particle and the number of incident particles; this parameter is independent of the kinetic energy.

We experimentally developed Faraday cup to collect electron beams generated from the plasma focus region. The cup was developed in bias mode with a 0.1Ω resistance, which was prepared with the parallel combination of ten carbon film resistors (resistance, 1Ω). The Faraday cup comprises a metallic disk as the charge collector and a flat circular copper disk (diameter, 7.5 mm). Carbon film is good absorber of secondary electrons and is used to control the secondary electron emission to avoid the contribution of electron with the electron beam (from the plasma focus) register on the circular disk. Furthermore, the cup was enclosed in the PVC pipe (Figure 3.12). The diameter of the Faraday cup was restricted by that of the PVC insulator tube, which was used in the hollow anode. Energetic electron beams were detected by placing the Faraday cup at the bottom end of the hollow anode 37 cm from the anode tip.

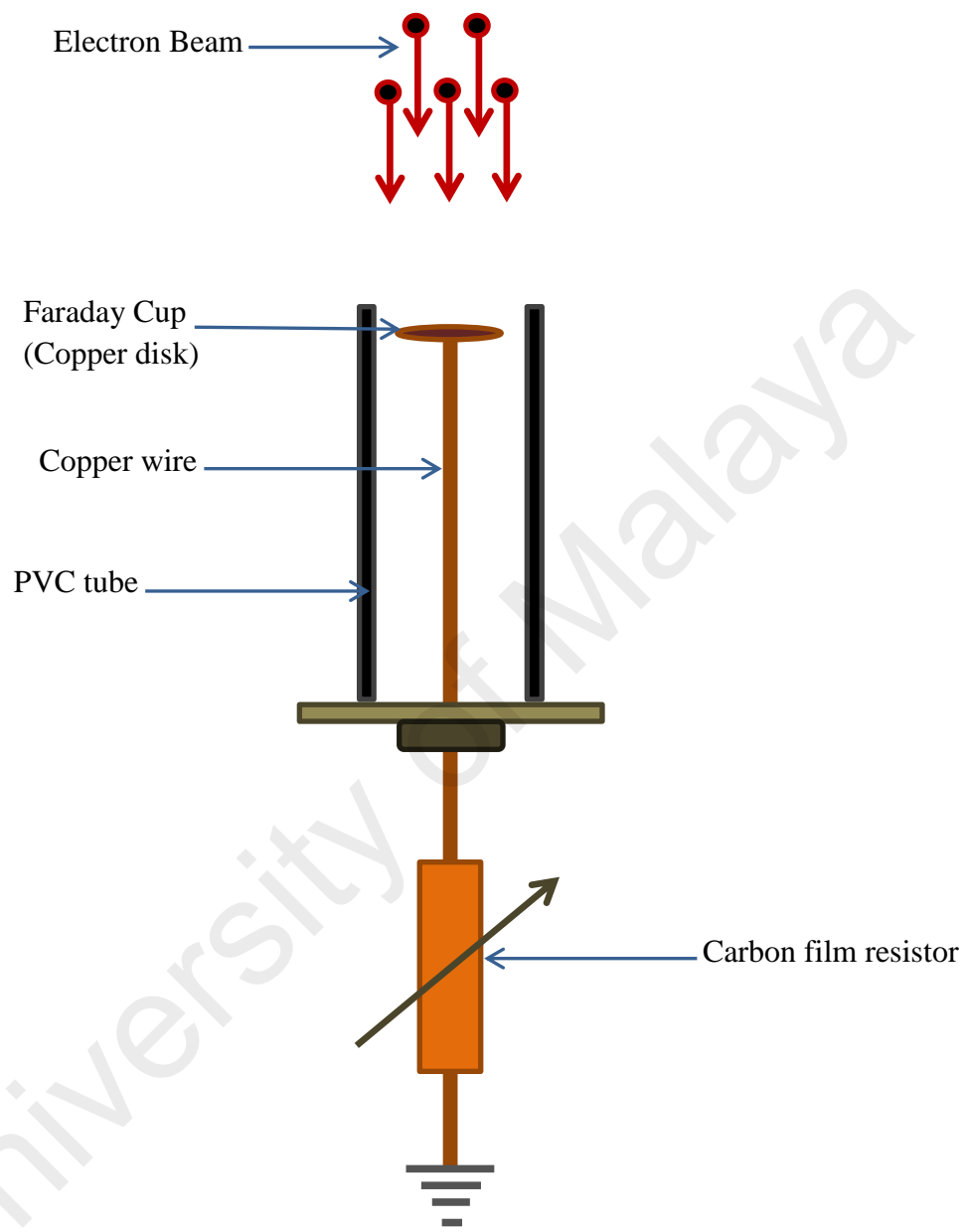


Figure 3.12: Schematic of Faraday Cup.

3.4 Data Acquisition and Analysis System

Two DPO4043 digital storage oscilloscopes were used to record all the data channels per discharge. The resultant data from the digital storage oscilloscope were both recorded on the Pin drive and then transferred to a computer. The experimental data were mostly analyzed using Microsoft Excel and Origin 6.0 software.

University of Malaya

CHAPTER 4

RESULTS AND DISCUSSIONS

4.1 Introduction

Plasma focus has been developed because of their relatively simple engineering and high X-ray yield. These machines are sources of pulsed neutrons, charged particles (electron and ions), and electromagnetic radiations. Although plasma focus is a considerably old device, it can potentially be used to analyze radiation emissions. The time evolution and energy distribution of the electron beam should be precisely determined to elucidate the physical mechanisms of its emission, acceleration, and viability for technological applications.

Table 4.1 lists the design and calculated parameters of the UM-DPF2.

Experiments were carried out at the Plasma Technology Research Center (UM-PTRC) of the University of Malaya (UM; Kuala Lumpur Malaysia) at discharge energy, charging voltage, and capacitance of 2.2 kJ, 12 kV, and 30 μ F, respectively. The lead was used as target in the whole experiments. The X-ray emission was investigated as a function of pressure (range, 0.7 mbar to 2.0 mbar); argon was used as the filling gas. Signals from the five shots were recorded using a four-channel BPX65 PIN diode, Rogowski coil, and high-voltage probe at five pressure values (Figure 4.1).

For each operating pressure, 10 discharges were fired for a specific gas filling pressure. The filling Ar pressure was refreshed after each shot to ensure constant discharge conditions for the entire experiment. For each new pressure, two conditioning shots at newly specified pressures were fired without recording the data. A hollow anode was used to analyze the emission of the electron beam from the plasma focus device.

Table 4.1: The design/calculated parameters of the UM-DPF2.

Capacitance (C_o)	30 μ F
Charging voltage (V_o)	12 kV
Capacitor voltage rating	40 kV
Stored energy ($E_o = 1/2 C_o V_o^2$)	2.2 kJ
Inductance ($L_o = T^2 / 4\pi^2 C_o$)	165 nH
Impedance ($Z_o = \sqrt{L_o / C_o}$)	74 m Ω
Anode (hollow) diameter (d_a)	19 mm
Cathode rod diameter (d_c)	9.5 mm
Anode length (l_o)	180 mm
Peak discharge current (I_o)	140 kA
Trigger unit voltage	30 kV
Electric circuit resistance (r_o)	14.55 m Ω
RC calibrating factor (K)	16.09 kA / V
Time period (T)	14.0 μ s

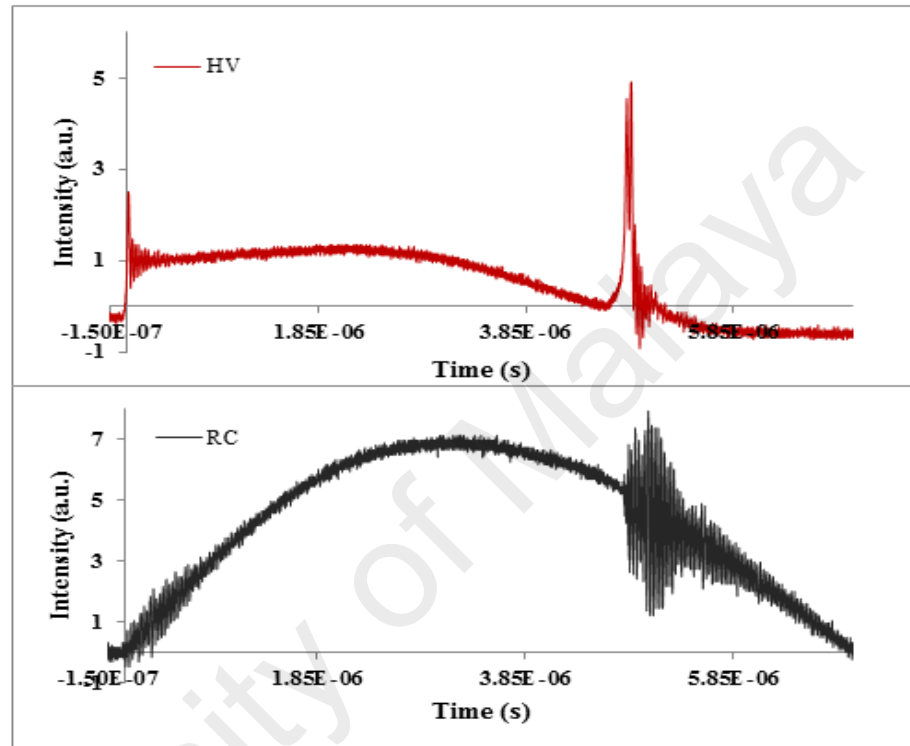


Figure 4.1: Typical Rogowski coil signal with high voltage probe.

When a strong plasma was observed, the following diagnostics were simultaneously used with a recorded sampling of 1 ns for the time resolved signals:

1. Five-channel BPX65 PIN diodes with different Al filters
2. XR100CR spectrometer for hard X-ray (HXR) spectra
3. Scintillator–photomultiplier detector for HXR
4. Faraday cup for plasma-induced electron emission

A theoretical model (Lee Model RADPF5.15FIB) was utilized in the experiment.

In this dissertation, the experimental data on the radiation and electron emissions in a specific pressure range (1.0 mbar to 2.0 mbar) for the Argon gas were obtained; the correlations with other diagnostic signals were analyzed.

The discharge of charged particles in the plasma column was demonstrated by the electron beam emissions in the low-energy PF device. The electrons were emitted towards the anode; the direction of ions discharge was opposite to that of electron emission. The emitted electron beams exhibited energies ranging from a few keV to hundreds of keV [113, 139].

To assess the function of the low energy plasma focus device as an electron beam source, and X-ray emissions from the Ar-operated plasma focus were investigated using time-resolved PIN diode detectors with respect to the filling pressure of the Ar. Table 4.2 lists the design parameters of the UM-DPF2 for the electron beam.

An array of filtered five-channel PIN diodes is housed at a distance of 43.50 cm from the head of the hollow anode to detect X-rays and measure the radiation emission from the plasma focus. The glass window of the PIN diode is covered with Al foils with specific thicknesses (Table 3.4) and detached to detect X-ray emissions. Figure 3.9

Table 4.2: The design parameters of the UM-DPF2 for the electron beam.

Component	Length (cm)	Diameter (cm)	Material
Hollow Anode	18.00	1.90/1.60 (O.D/I.D)	Copper
Cathode Rod	27.20	0.95	Copper
Insulator sleeve	5.00	2.00	Pyrex
Faraday cup plate	0.1	0.75	Copper
Photo diode (BPX65)	---	---	---

illustrates the transmission curves of the BPX-65 diode that was attached with absorption filters. The PIN diode response ranged from 0.5 keV to 30 keV [140].

Figure 4.2 shows the schematic of the UM-DPF2 device that corresponds to the typical signals from the Rogowski coil, high-voltage probe, and two X-rays with specific Al foils. Typical X-ray signals were generated using an Al foil (20 μm , 30 μm) with 23 μm aluminized Mylar. The strong focus yielded the information of a signal pulse that started from 4.65 μs and ended at 4.67 μs ; the peak value was at 4.66 μs .

The pulse of the X-ray signals was correlated with the voltage spike. The delay period of compression corresponded to the position of the top portion of the hollow anode about 9 cm below the cathode rods.

Therefore, the radiation emission from the focus region yielded a small contribution to the electron beam that hit with the hollow anode. We assumed that the X-ray pulse was ascribed to the strong interaction of the electron beam with the edge surface of the hollow copper anode.

The uniqueness of the Rogowski and voltage signals prompted the development of strong plasma focus [50]. The operational pressure regime for the radiation emission with the hollow anode was obtained by varying the filling pressure of the argon gas. The optimum pressure of the argon gas (1.7 mbar) was ascertained from the maximum dip in the Rogowski coil signal and the maximum spike in the voltage and BPX65 PIN diode signals. The peak(s) in the BPX65 PIN diode signals were also observed using the hollow anode. X-ray emissions occurred in brief pulse(s) with duration of 20–30 ns, which was coincident with that of the Rogowski signal. Johnson [108] and Zakaullah *et al* [141] reported SXR pulses with a duration of ~ 125 ns, which was inconsistent with that of the observed pulse. By contrast, a pulse duration of 10–20 ns was reported [142, 143]. The irregularities in the pulse durations were attributed to the differences in the

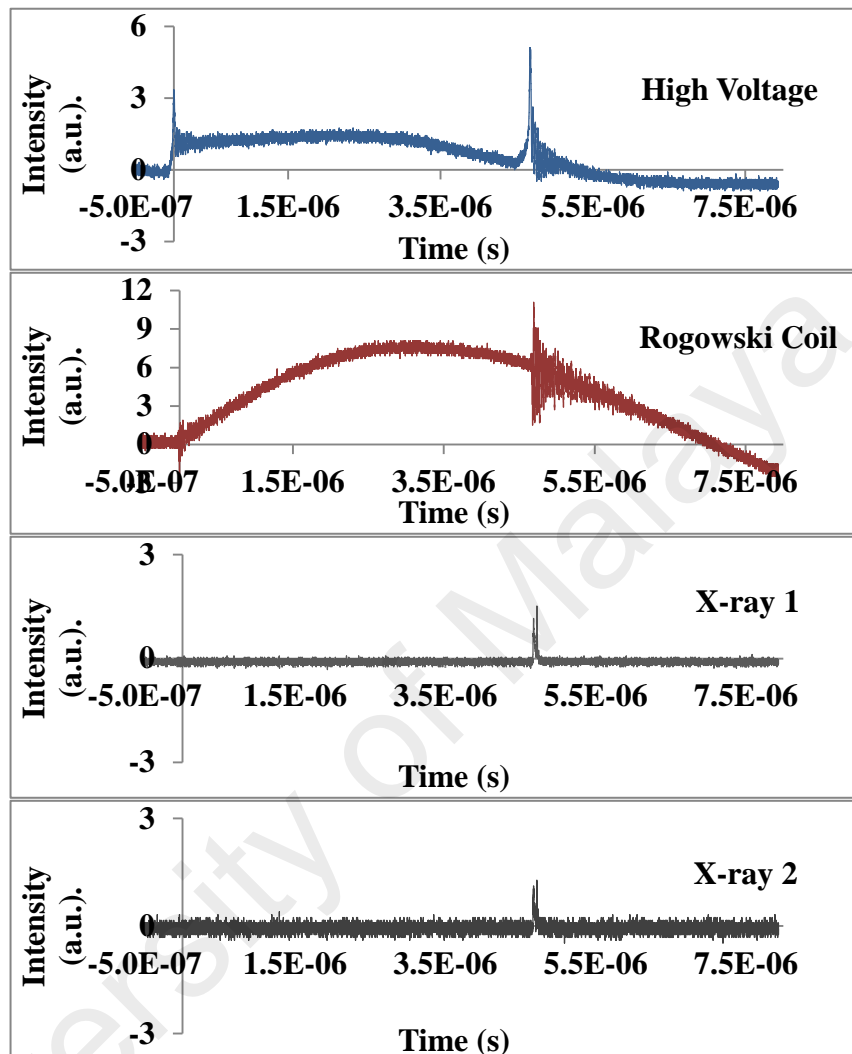


Figure 4.2: Typical signals of Rogowski coil, high voltage probe, two X-ray diodes with specific Al foils ($20\mu\text{m}$, $30\mu\text{m}$).

device parameters.

The X-ray yield in 4π -geometry and the system efficiency of X-ray emission can be calculated from five-channel PIN diodes that are masked with Al foils. The X-ray yield is calculated as follows [144-146]:

$$Y = \frac{Q_{exp}(4\pi)}{d\Omega S(E) T(E)} \quad (4.1)$$

where, $Q_{exp} = \int \frac{V dt}{R}$ (Coulomb) .

where, $\int V dt$ represents the area under the curve with the filter of the PIN diode, $R = 50 \Omega$, $S(E)$ is the average sensitivity of the detector, and $T(E)$ is the average filter transmission. $d\Omega = dA/r_o^2$ (sr.) is the solid angle subtended by the detector at the anode center, where $dA = \pi r^2$, r (cm) is the radius of the exposed area of one detector, and r_o (43.50 cm) is the distance between the detector and hollow anode.

4.2 Five channel PIN diode for Radiation Measurement

The variations in X-ray emissions as functions of the Argon gas pressure possess efficient functions in generating radiation in the plasma focus device. A pair of Ross filters (20 μm Al foil, 100 μm Al foil; 30 μm Al foil, 100 μm Al foil; 40 μm Al foil, 100 μm Al foil) are used to determine the X-ray yield. Figure 4.3 shows the variations of the average signal intensity with different Argon gas pressures.

The maximum average signal intensities are recorded with 20 μm , 30 μm , and 40 μm Al foil at an Argon gas pressure of 1.7 mbar.

The variations in the total X-ray yield against Argon gas pressures at a constant applied voltage of 12 kV are shown in Figure 4.4. The maximum total X-ray yields are

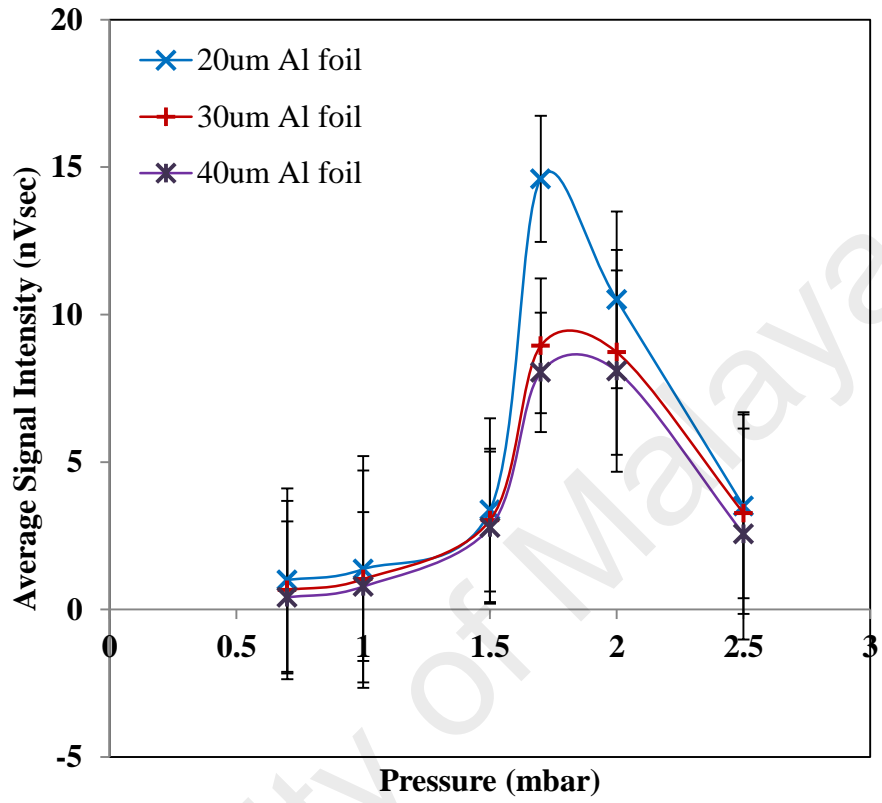


Figure 4.3: Variation of average signal intensity recorded by Al foil (20 μm , 30 μm , 40 μm) versus Argon gas pressure.

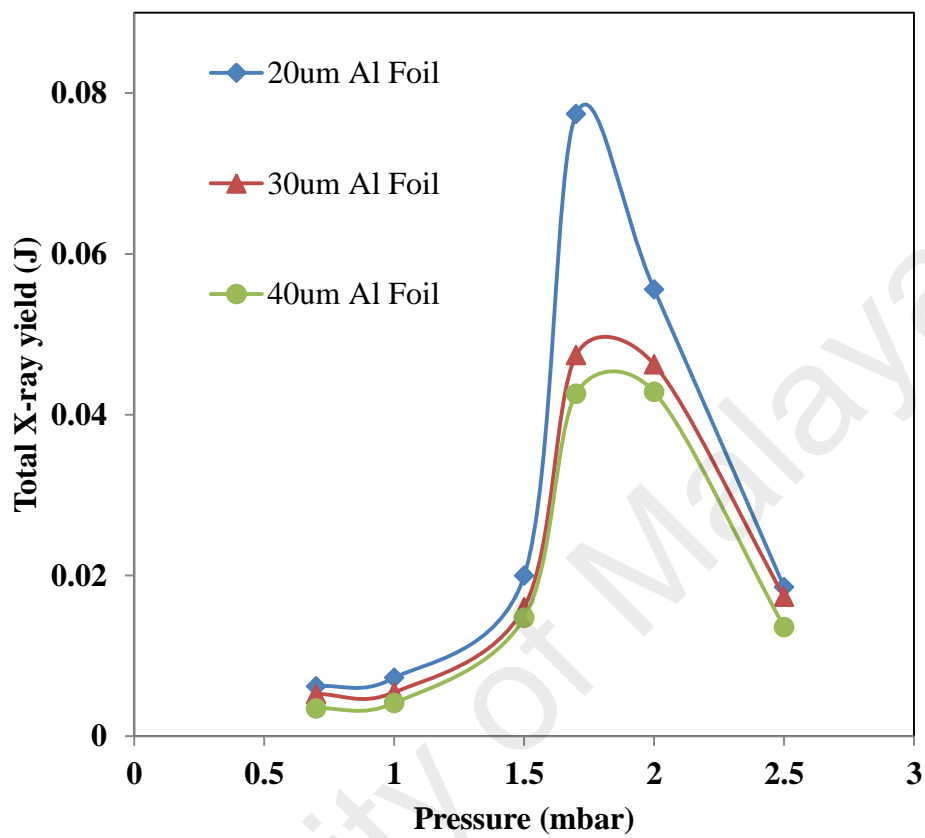


Figure 4.4: Variation of total X-ray yield in 4π -geometry versus Argon gas pressure at constant applied voltage 12 kV.

total X-ray yields are 77 mJ, 47 mJ, and 42 mJ in 4π -geometry at an optimum pressure of 1.7 mbar.

After a series of experiments, maximum X-ray yield is obtained at a pressure of 1.7 mbar (constant voltage, 12 kV) by using pairs of Al foils with specific thicknesses (20 μm Al foil, 100 μm Al foil; 30 μm Al foil, 100 μm Al foil; 40 μm Al foil, 100 μm Al foil). These foils are fixed on top of the hollow anode tip at a distance of 43.50 cm. The energetic electron beam interacted with the lead target, which is placed at a depth of 27 cm in the hollow anode.

The results revealed that the maximum total X-ray yields are 77 mJ, 47 mJ, and 42 mJ at an Argon gas pressure of 1.7 mbar by using pairs of Al foils with respective thicknesses of 20 μm and 100 μm ; 30 μm and 100 μm ; and 40 μm and 100 μm . The results from our low-energy plasma focus device are significant. The radiated energy depended on the filling pressure and the hollow anode shape because of the strong electron beam–hollow anode interactions. The X-ray yield decreased for pressures higher or lower than the optimum Argon pressure (1.7 mbar). The X-ray yield could be enhanced by reducing the system inductance, system size, and factors related to the electron beam–hollow anode interactions. The X-ray yield is high in the Argon pressure range of 1.5 mbar to 2.0 mbar; therefore, the intensity of the electron beam is high in this range for potential applications in the analysis of material characteristics.

The images of the target before and after hitting by the energetic electron beam in the plasma focus are shown in Figure 4.5; this interaction is attributed to the bombardment of the energetic electron beam. The images reveal that when the electron beam hits the lead target (diameter, 1.5 cm; width, 0.35 cm), the electron beam is generated from the plasma focus region. Lead is a feasible material to produce maximum X-ray yield, in contrast to other materials.

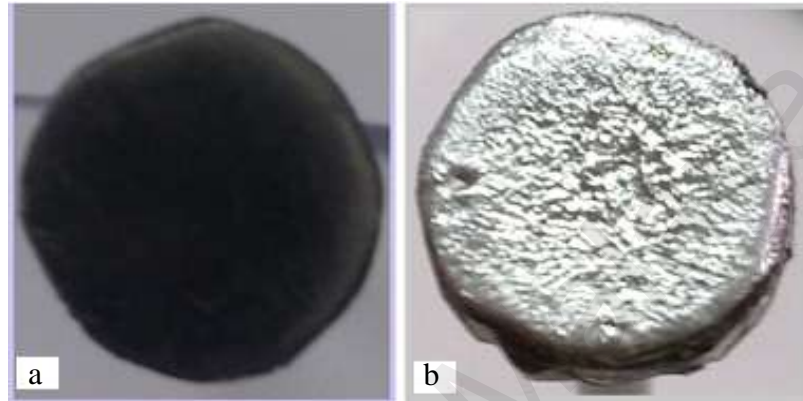


Figure 4.5: Images of the lead target (a) before and (b) after interaction with an electron beam in the plasma focus.

The images reveal that the electron beam produced from the plasma focus region hits the lead target (diameter, 1.5 cm; width, 0.35 cm) and produced X-rays. Lead is a material to produce possible maximum X-ray yield. The marked image in Figure 4.5 (b) is attributed to the interaction of the target with an electron beam generated for Argon pressures ranging from 15 mbar to 2.0 mbar. The flux of the electron beam significantly affected the material.

Electron Temperature at the different pressure: The X-ray signal ratio $R = I/I_0$ to measure temperature (where I is the absorbed intensity, and I_0 is the intensity) was calculated against different Al foil thicknesses for electron temperatures ranging from 3 keV to 7 keV and pressures ranging from 1.0 mbar to 2.5 mbar.

Figure 4.6 describes the estimated electron temperature from ratio method is found around 3 keV when the Argon gas pressure is 1.5 mbar. The electron temperature is 7 keV with the Argon gas pressure 1.7 mbar in Figure 4.7. Figure 4.8 shows 6 keV electron temperature with the Argon gas pressure 2.0 mbar.

The maximum electron temperature at optimum Ar gas pressure (1.7 mbar) and constant voltage (12 kV) was found to be 7 keV. This result was obtained from the hollow anode in the UM-DPF2 device.

The ratio curves for all peaks between 1.5 mbar and 2.0 mbar lie close to the absorption curve for Cu radiation. This result implied that the plasma was largely contaminated with Cu impurities related to the X-ray emission from the Cu-K α line. The X-rays are ascribed to the interactions of energetic electrons with the hollow Cu anode. In plasma focus, the energetic electron beams are dependent on the gas pressure [113]. The electron beam intensity increases up to a specific optimum pressure and decreases for pressures higher or lower than the optimum value. The results further revealed that our plasma focus device is highly contaminated with Cu impurities.

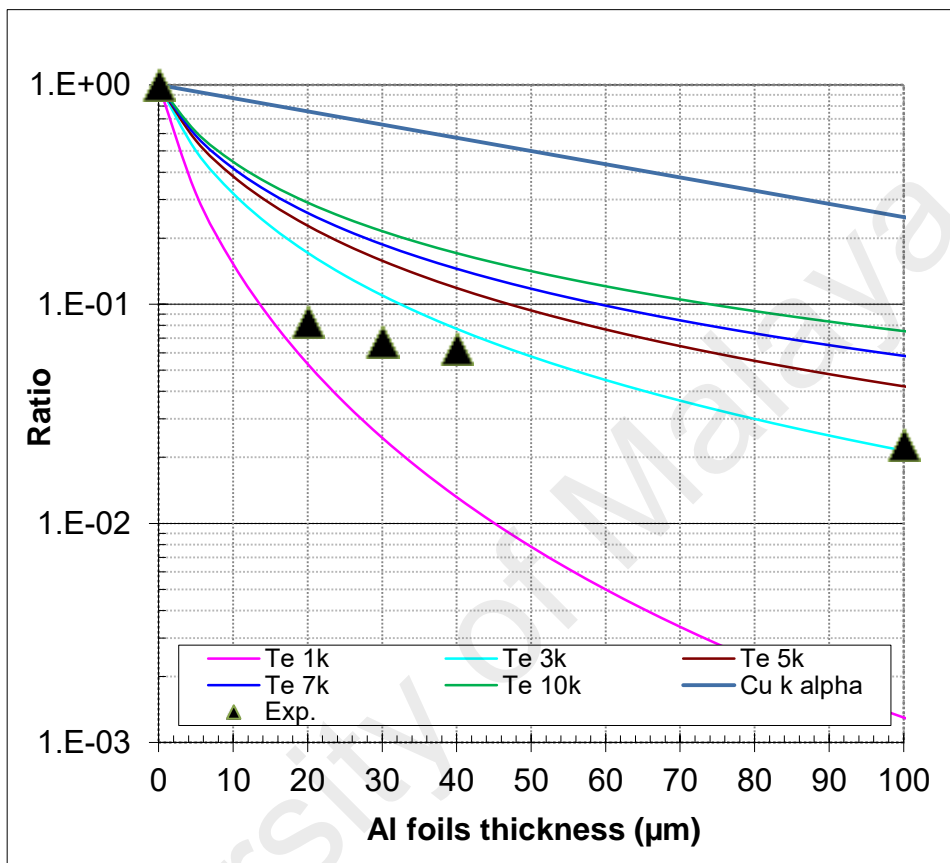


Figure 4.6: Calculated absorption curves of Al foils for X-rays from copper plasma at various temperature and Cu K α X-rays with Argon gas pressure 1.5 mbar, estimated electron plasma temperature 3 keV.

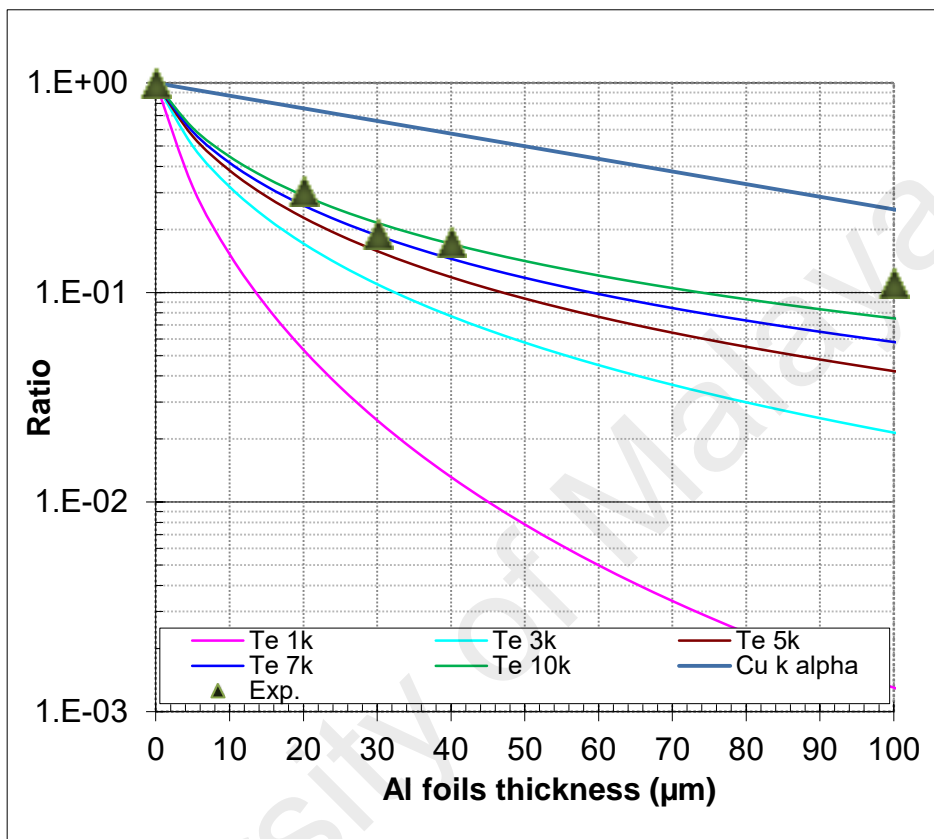


Figure 4.7: Calculated absorption curves of Al foils for X-rays from copper plasma at various temperature and Cu K α X-rays with Argon gas pressure 1.7 mbar, estimated electron plasma temperature 7 keV.

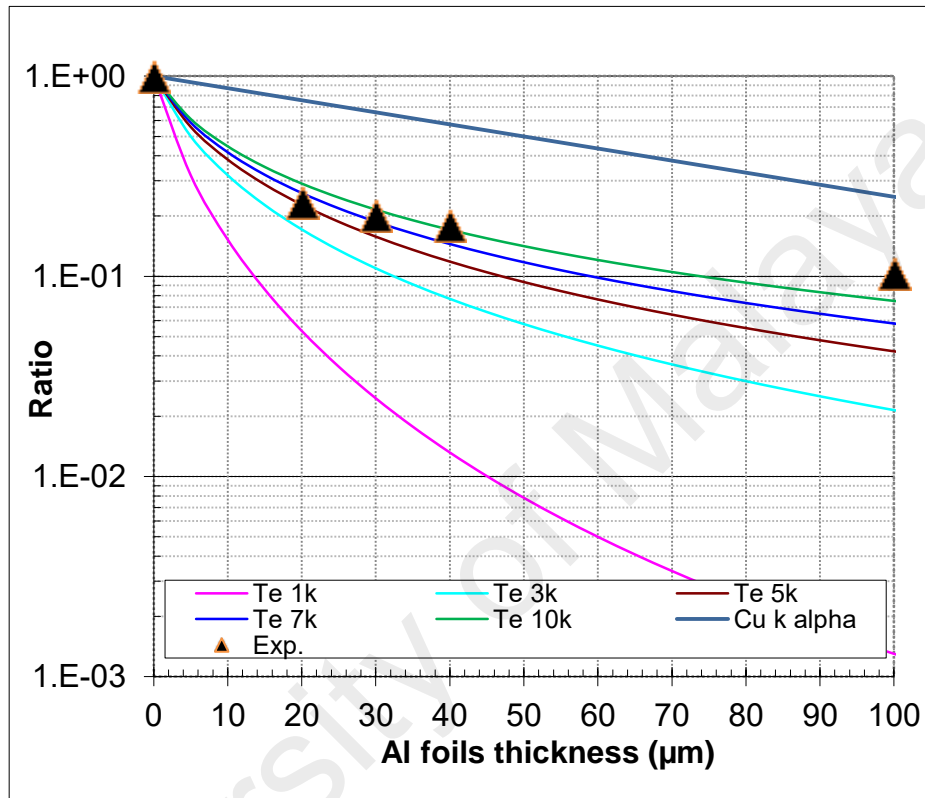


Figure 4.8: Calculated absorption curves of Al foils for X-rays from copper plasma at various temperature and Cu K α X-rays with Argon gas pressure 2.0 mbar, estimated electron plasma temperature 6 keV.

Therefore, the radiation primarily originated from Cu impurities generated from the bombardment of energetic electrons with the hollow anode surface.

The Rayleigh–Taylor (RT) instability in the compression period of the plasma focus was established via interferometric analyzes [112]. The interface between the plasma and the magnetic field was unstable during radial compression; the inertial force inside the plasma column was directed normal to the magnetic field. The electrons and ions drifted in the opposite direction because of the charge-independent force that interacted with the magnetic field. Charge separation in the surface layer of the plasma column was caused by this drift. This separation established an electric field, which introduced another plasma drift and resulted in RT instability. The boundary of the plasma column was fluted because of the RT instability at the end of compression. This instability was developed at about 30 ns [147].

4.3 The X-ray spectrometer for X-ray Spectrum from Target

An XR100CR X-ray spectrometer was used at the top and side of the system to record the X-ray line spectra caused by the electron beam– target collision (Figure 4.9). This spectrometer could suitably analyze the distribution of X-ray energy and was sensitive up to the energy of 45 keV.

The X-ray spectrometer was used to trace the X-ray line spectra and analyze the X-ray energy spectrum up to 45 keV. In the first experiment, this spectrometer was used at a side-on position below the system (distance from focus region, 37 cm; distance from the lead target, 4 cm; angle, 45°). The X-ray line spectra showed energies of 8.07 keV, 8.67 keV, and 10.42 keV, which correspond to Cu-K_{α1}, Cu-K_{β1}, and Pb-L_{α2} lines

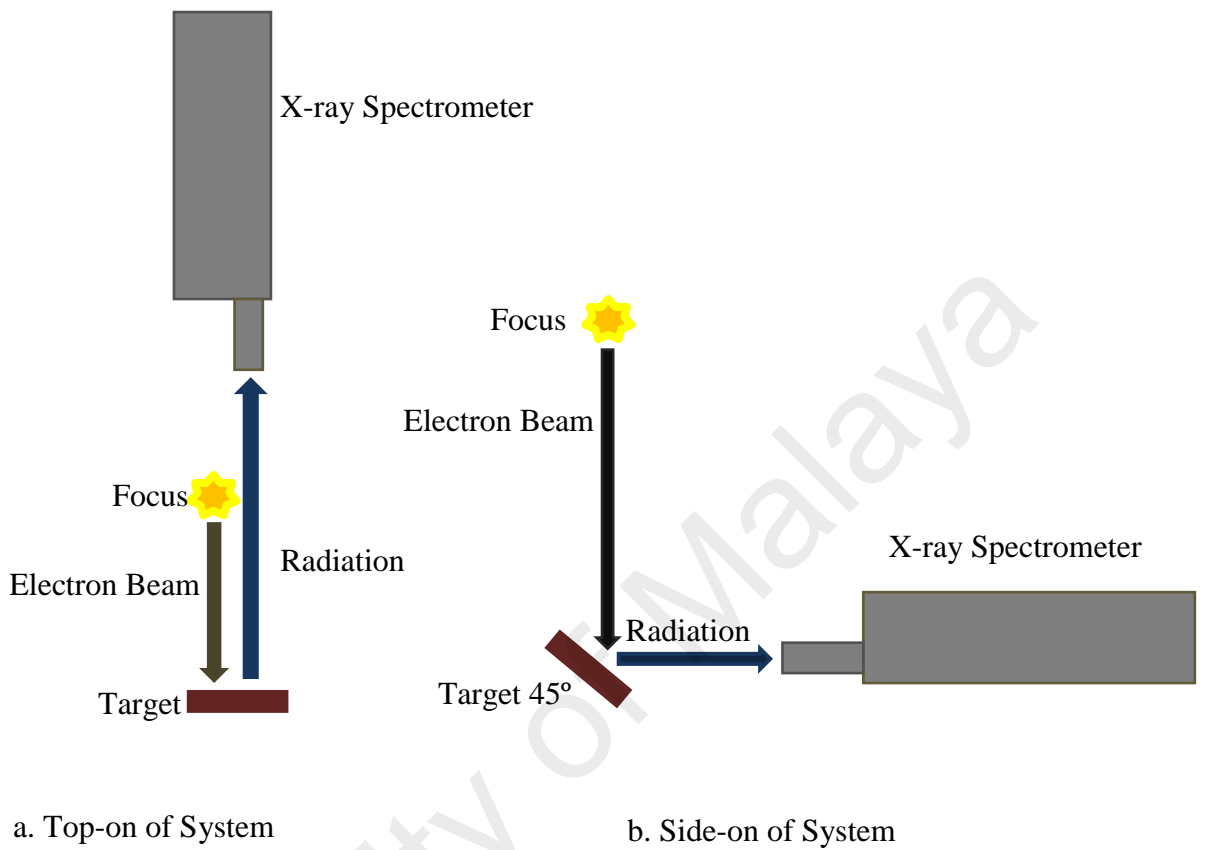


Figure 4.9: X-ray Spectrometer position at top-on of the system with the target (a) and side-on of the system with a target at an angle of 45 degree (b).

with temporal evolution of X-ray pulses at specific Al foil thickness and Argon pressure of 1.7 mbar. X-ray-1 (23 μm aluminized Mylar plus 30 μm Al foil) and X-ray-2 (23 μm aluminized Mylar plus 20 μm Al foil) were used with signals from the high-voltage probe and Rogowski coil Figure 4.10.

For the second experiment, the X-ray spectrometer was used at the top-on position of the system at a distance of 47.50 cm from the lead target within the hollow anode. The X-ray line spectra revealed energies of 8.80 keV and 10.46 keV, which correspond to Cu- $K_{\beta 1}$ and Pb- $L_{\alpha 2}$ lines with temporal evolution of X-ray pulses with specific Al foil thickness and Argon pressure of 1.7 mbar. X-ray-1 (23 μm aluminized Mylar plus 30 μm Al foil) and X-ray-2 (23 μm aluminized Mylar plus 20 μm Al foil) were used with signals from the high-voltage probe and Rogowski coil Figure 4.11.

Spectrometric results supported the energetic electron beam emission from the focal region because of instabilities upon collision with the target material. The energetic electron beam energy was high enough to Pb- $K_{\alpha 1}$ (74.96 keV) radiation in the X-ray line spectrum. However, this radiation was impossible to be detected by the present spectrometer because of constraints in its energy range.

Additional, the X-ray spectrometer was used to trace the X-ray line spectra of In and Cu targets at the side-on position at the same conditions. The X-ray line spectra of the Cu target exhibited energies of 8.047 keV, 8.905 keV, and 0.929 keV, which corresponded to Cu- $K_{\alpha 1}$, Cu- $K_{\beta 1}$, and Cu- $L_{\alpha 2}$ lines with temporal evolutions of the X-ray pulses at specific Al foil thicknesses and a constant Ar pressure of 1.7 mbar (Figure 4.12). Similarly, the X-ray line spectra of the In target showed energies of 24.17 keV, 27.28 keV, 3.26 keV, and 3.487 keV that were ascribed to In- $K_{\alpha 1}$, In- $K_{\beta 1}$, In- $L_{\alpha 1}$, and In- $L_{\alpha 2}$ lines at conditions similar to those of the Cu target (Figure 4.13).

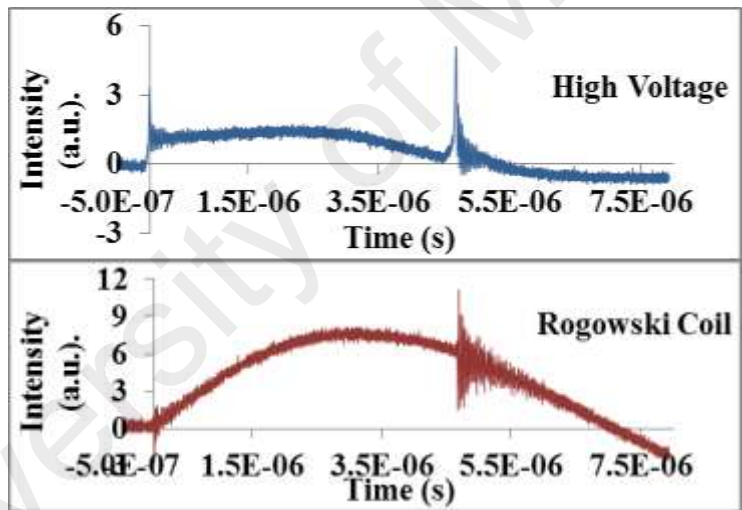
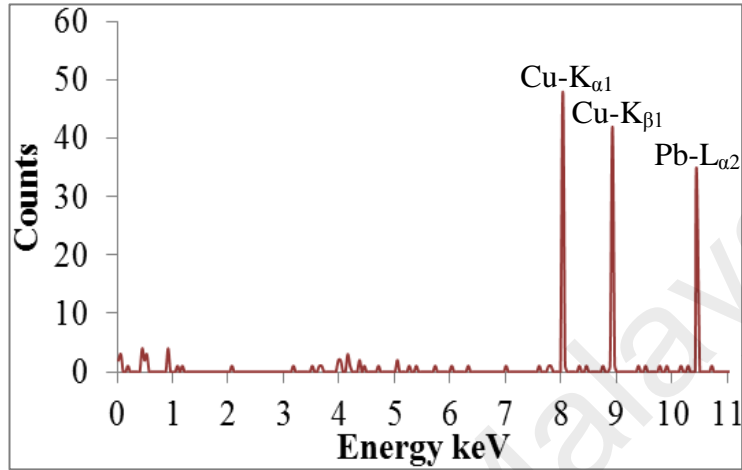


Figure 4.10: X-ray spectrum: X-ray produced by energetic electron beam target effect at an angle of 45° when the spectrometer is at the side-on position with typical high voltage and Rogowski coil signal at pressure 1.7 mbar.

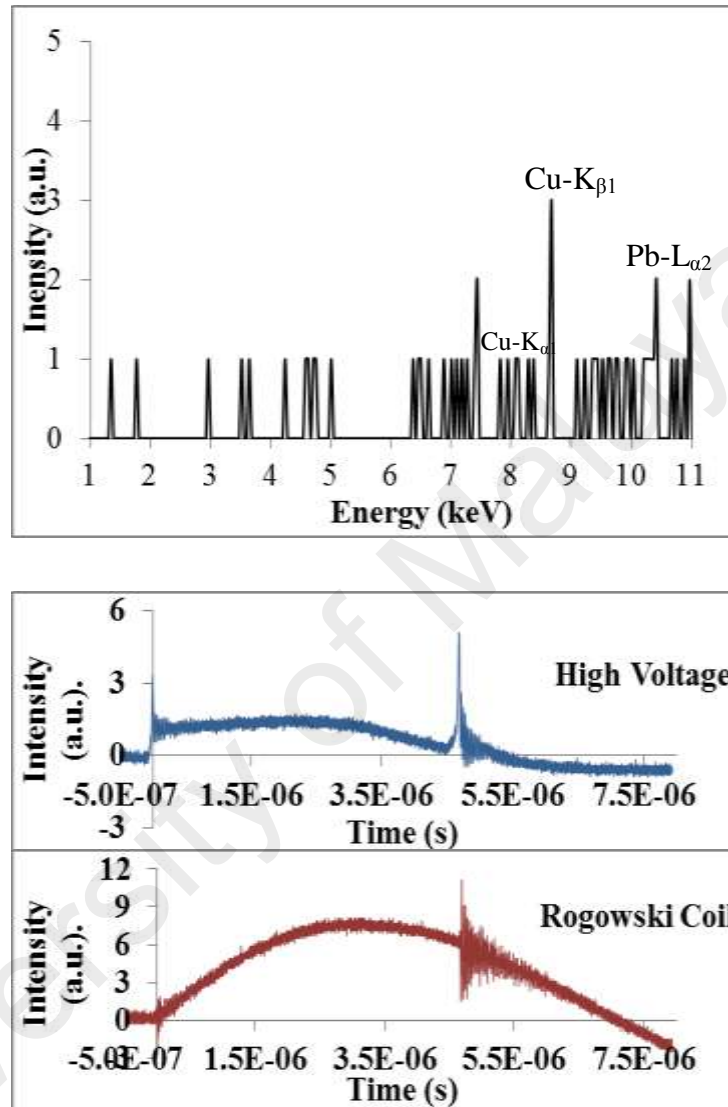


Figure 4.11: X-ray spectrum: X-ray produced by electron beam target effect when spectrometer is at top-on position with typical high voltage and Rogowski coil signal at pressure 1.7 mbar

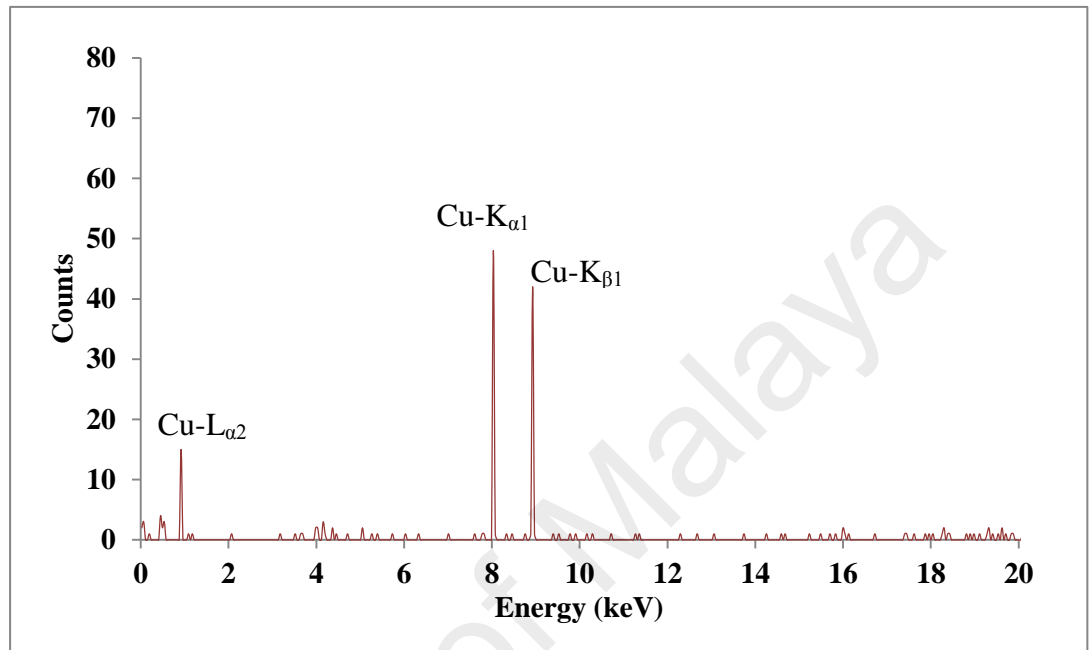


Figure 4.12: X-ray spectrum: X-ray produced by electron beam target (Copper) effect at an angle of 45° when the spectrometer is at a side-on position at pressure 1.7 mbar.

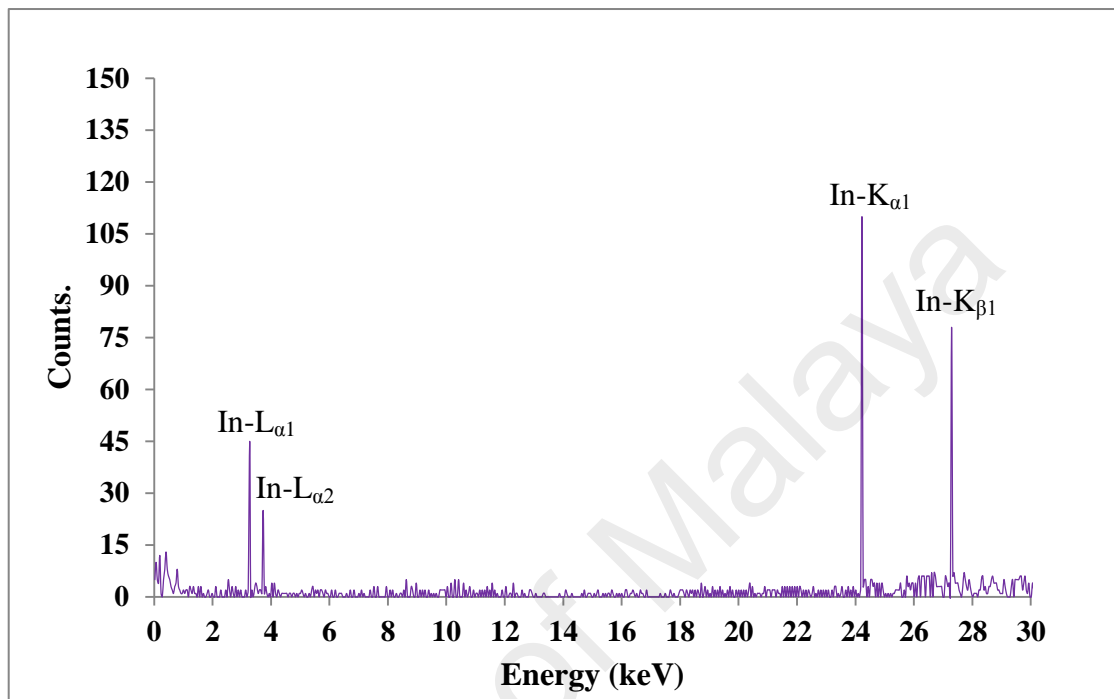


Figure 4.13: X-ray spectrum: X-ray produced by electron beam target (Indium) effect at an angle of 45° when the spectrometer is at a side-on position at pressure 1.7 mbar.

The spectrometry results supported the emission of the energetic electron beam from the focus region because of the instabilities upon collision with the Cu and In targets. The corresponding beam energy was high enough to induce Cu- $K_{\alpha 1}$ and In- $K_{\alpha 1}$ radiations in the X-ray line spectrum at the optimum Ar pressure.

However, the X-ray line spectra of Pb, Cu, and In targets were hardly detectable by using the XR100CR spectrometer for Ar pressures ranging from 0.5 mbar to 0.7 mbar because of the very weak focus. This result implied that the energy of the electron beam was low at low eV, which is not sufficient to obtain the X-ray line spectra of different targets. The electron beam interacted with the targets at 1.0 mbar and 1.5 mbar; however, the resultant spectra were not detected because of the background radiations. As a result, the associated energies could not be counted. The electron beam energy was around 50 keV at a pressure of 2.0 mbar, which aptly enabled the target–beam interaction. However, the X-ray line spectrum of the target materials could not be obtained because of the few electron–target interactions. The focus failed to aptly generate the electron beam from the PF region for pressures higher than 2.0 mbar to interact with the material and to radiate the HXR. The notable X-ray line spectra of Pb, Cu, and In targets were obtained at an Ar pressure of 1.7 mbar; a similar good agreement of the energetic electron beam was observed at the same pressure to detect the X-ray line spectrum from the plasma focus region of the low energy focus device. The X-ray line spectrum could be detected from 1.5 mbar to 2.0 mbar when the background radiation and others factors were reduced in the plasma focus device.

The spectrometry results implied the emissions of the energetic electron beam from the focus region that hits the target materials. The flux of the electron beam significantly affected these materials.

4.4 Scintillator-Photomultiplier Detector for Hard X-rays

An R928 photomultiplier tube (PMT) coupled with a cylindrical plastic scintillator was positioned at 4 ± 0.5 cm from the system. The target was adjusted at 37 cm from the focus within the hollow anode (Figure 4.14).

The PMT was used to detect the signals; the electrical output signal reproduced a waveform to the incident pulse waveform with an electron transit time of 22 ns. PMT-scintillator signals obtained at an operating pressure of 1.7 mbar is shown in Figure 4.15.

PMT-scintillator was used to determine the emissions of X-ray produced by the electron beam from the plasma focus. The radiation was observed from 1.5 mbar to 2.0 mbar. The radiation intensity was attributed to the bombardment of the electron beam on the target, which was adjusted at an angle of 45° . The total radiation between 1.0 mbar and 2.0 mbar was shown in Figure 4.16. The total radiation increased in the aforementioned pressure because of the bombardment from the electron beam. The maximum radiation was recorded by PMT-scintillator at 1.7 mbar. This result implied the importance of the presence of the total radiation including energetic electron beam emission from the plasma focus region in low-energy plasma focus devices. This beam emission was attributed to the instabilities that create in the focus.

The results of total radiation were achieved at a pressure range of 1.5–2.0 mbar because of the bombardment of the electron beam. Furthermore, the results from the X-ray spectrometer supported the emissions of the energetic electron beam from the focus region because of instabilities upon hitting the target material. The flux of the electron beam significantly affected the target material (lead).

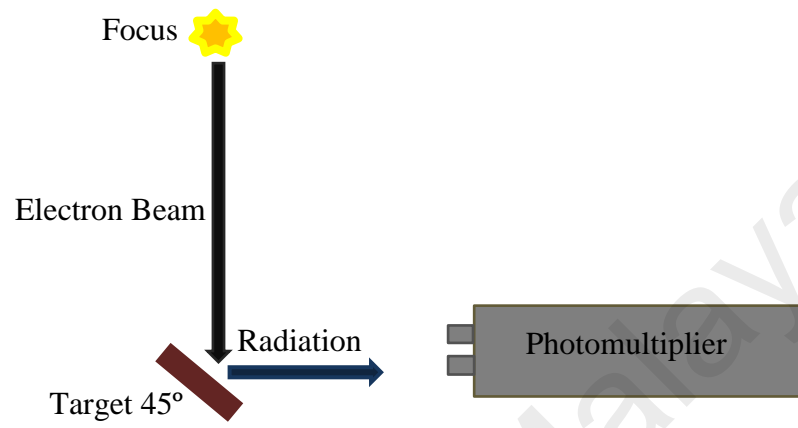


Figure 4.14: Schematic of Photomultiplier tube (PMT) coupled with the scintillator.

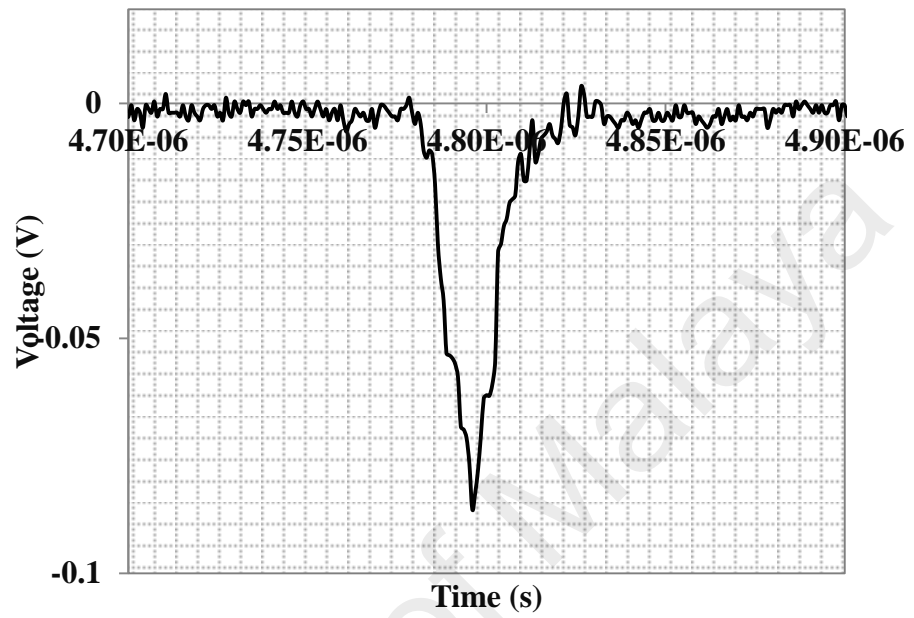


Figure 4.15: Typical signals of PMT-scintillator.

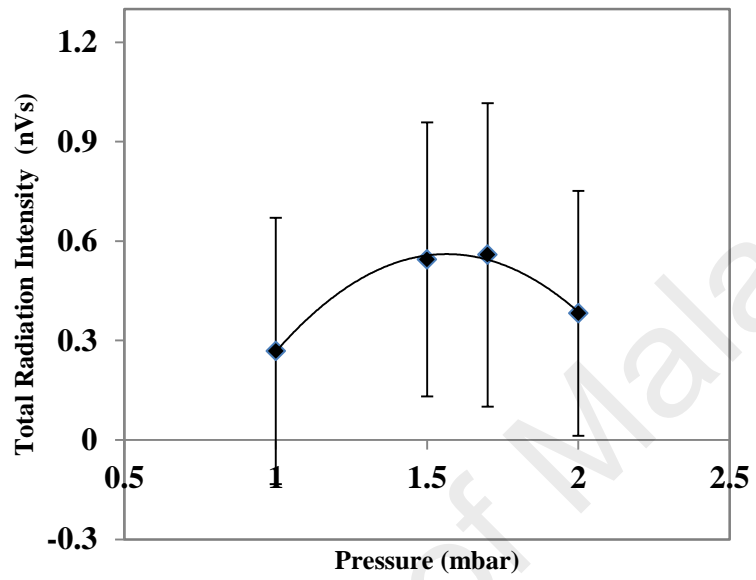


Figure 4.16: Variation of the total radiation intensity with PMT verses Pressure (mbar).

The lower and upper limits of the electron energy differed from the actual values because of the technical limitations of our approach. The proposed technique provided appropriate information of low energy plasma focus devices as electron beam sources.

4.5 Faraday Cup Design for Electron Emission

Acceleration mechanisms have been proposed to consider the electron beam in the plasma focus. Theoretical reports suggest that the accelerating field can be produced by rapidly changing the magnetic field because of the collapse and expansion of the pinch column [148] and anomalous resistivity-induced, rapid current distribution [149]. The emission of electron beams from the low energy plasma focus devices was analyzed [150]. Studies have focused on the physical mechanisms of the generation of electron beams by correlations with the emissions of HXR [72], ion beams [23, 73], neutrons [151], and electrical measurement [23]. The emission of high-energy electron species from the plasma focus was reported with slight speculations for that of HXR. Bernstein *et al.* [44] showed that the measured X-ray intensity was dependent on a power law E^{-2} because of the bombardment of axially accelerated electrons instead of the plasma Bremsstrahlung. Furthermore, Beckner *et al.* [152] found that the dominant X-ray emission caused by the high-energy electrons striking the anode; their results implied the generation of a high electric field in the plasma focus, which accelerated the electrons.

Time-resolved analyzes of electron beam emissions were performed by using Rogowski coils, Cherenkov detectors, and Faraday cups. Smith *et al.* [113] investigated the electron beam emission from a 3 kJ plasma focus device using a fast response Faraday cup and a magnetic energy analyzer. They obtained electron beams that

exhibited energy, current, and pulse duration of 300 keV, 2 kA, and 10–20 ns, respectively.

Short-pulsed, high-power electron beam sources have been widely applied because of their ability to efficiently deposit energy in a given volume or surface at a very short time. Lee *et al.* [76] demonstrated that the electron beams emitted from the plasma focus could lithographically print micro-sized structures (size, 0.5 μm). Tartari *et al.* [153] proposed X-ray brachytherapy source based on the interaction of relativistic electron beam of the plasma focus with high-Z targets.

The electron beam emission from our UM-DPF2 device [154] was investigated, and its essentialities in plasma physics and technological applications were determined. In this study, the diagnostic was a combination of Faraday cup and a photodiode [155], which was satisfactory good in terms of simplicity, cost, and performance.

Diagnostics that can estimate the time history, beam energy and beam flux of electron beams can be designed and developed. Although HXR analysis yields a power law dependence on the X-ray photon energy, the electron energy spectra could not be exclusively determined. Faraday cups are simple and cost-effective diagnostics that exhibit fast signal processing and particle detection with wide energies ranging from a few keV to few hundreds of keV.

In this study, the combination of a self-biased Faraday cup and photodiode were employed to determine the electron beam emission from our UM-DPF2 device. The basic details of Faraday cups are already explained in Chapter 3. A photodiode (BPX65) was used with the Faraday cup at the same position and distance from the top end positions of the hollow anode (Figure 4.17). A technique was proposed to identify the emissions of the electron beam with photoemissions before and after focusing from the focus region.

When the electron beam strikes the Faraday cup, a current flows through the resistance; thus, a negative repulsive voltage [$V = I \times R$] is developed across the resistance. This voltage functions as the self-bias potential for the Faraday cup. The electrons with energies similar to or lower than those of the potentials are repelled because of the latter. These particles do not contribute to the electron beam current based on Faraday cup measurements.

In this experiment, the Faraday cup–photodiode combination was employed and arranged to determine the temporal behavior of the emissions from the electron beam and photoemissions from the plasma focus. The signals from the electron beams, photoemissions, high-voltage probe, and Rogowski coil were recorded on the oscilloscope at various filling gas pressures after a few conditioning shots, which was required to suitably operate the plasma focus device. For each operating pressure, a minimum of seven shots were taken; the corresponding signals from the electron beams and other sources were recorded. Five shots from the electron beam signals were considered to obtain the time evolution of electron beam measurement and estimate the current, charge, and density of the electron beam. Subsequently, the experimental results were analyzed.

Typical signals from the energetic electron beam, photodiode, high-voltage probe, and Rogowski coil (pressure, 1.7 mbar) are shown in Figure 4.18. The electron beam current abruptly increased and coincided with the dip in the signal of the high-voltage probe. The electron beam current initially increased and reached the maximum compression that lasted for around 300 ns [156]. The signals from the electron beam current exhibited multiple spikes, and were correlated with the different pinch stages of the PF and the X-ray emissions with the corresponding photon energies. The first, low-amplitude spike was observed just before the maximum compression followed by multiple, high-intensity spikes.

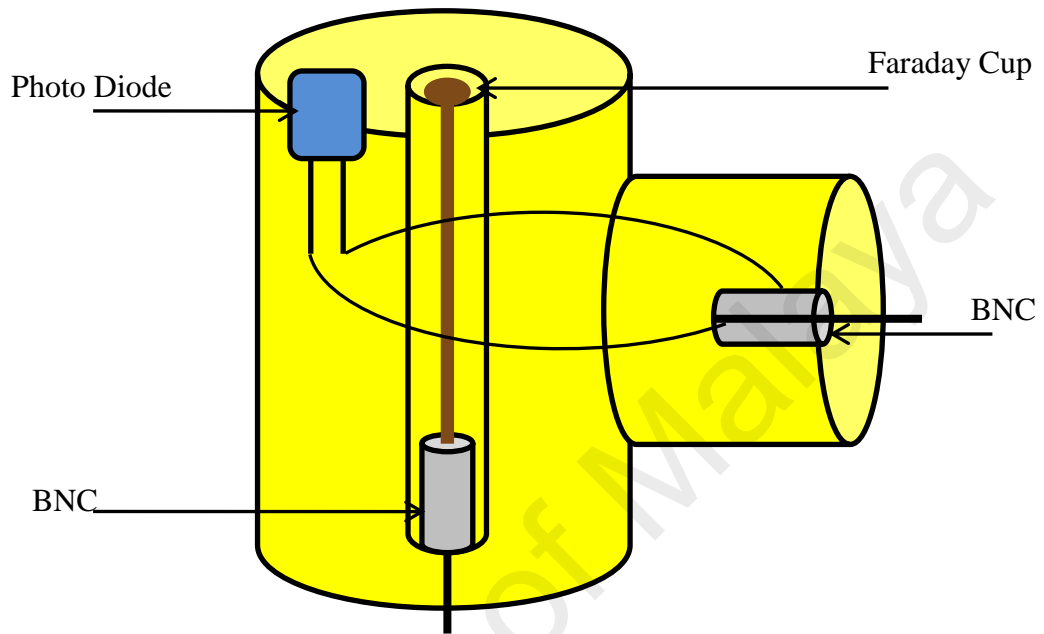


Figure 4.17: Schematic of the arrangement of Faraday cup with Photo diode.

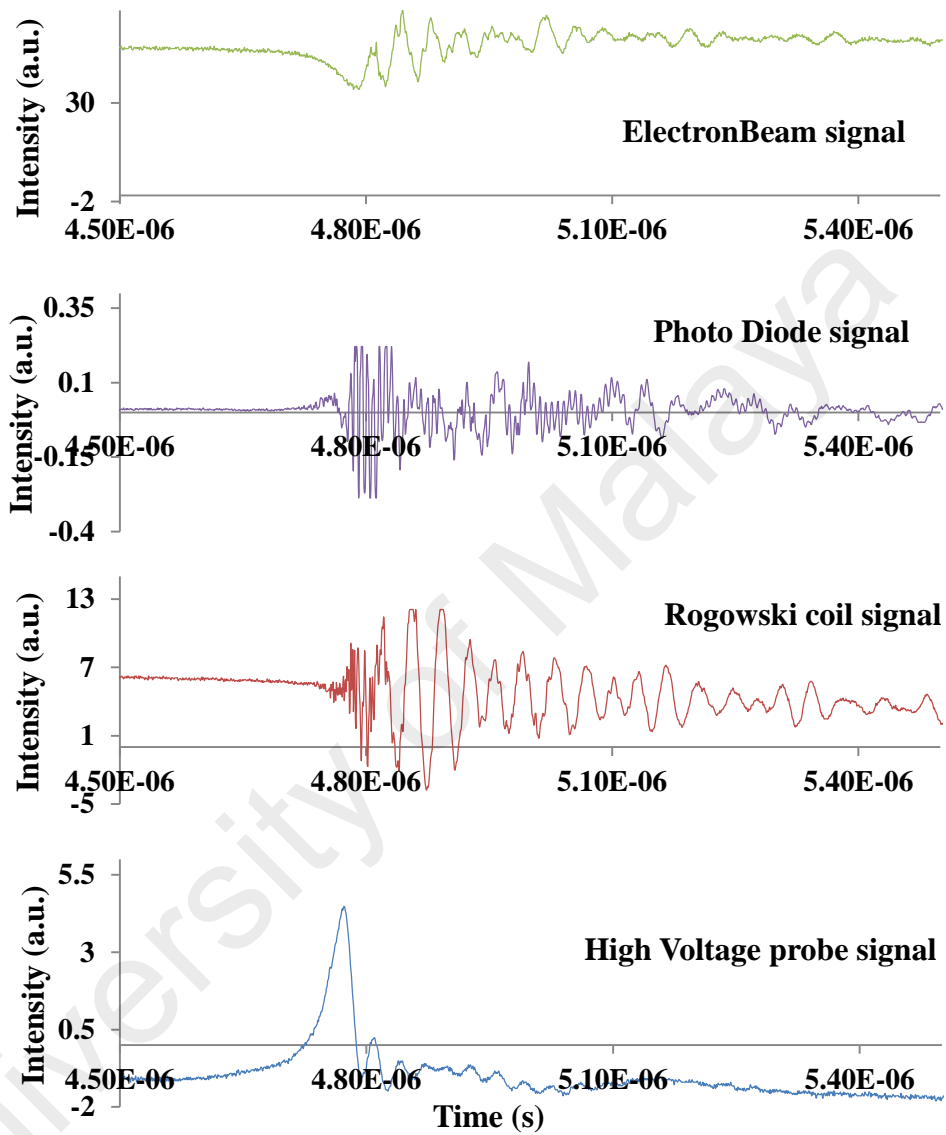


Figure 4.18: Typical energetic electron beam signal with the signals of photo diode, high voltage probe and Rogowski coil (at a pressure of 1.7 mbar).

The first spike was attributed to the breakaway electrons from the collapsing current sheaths caused by the positive anode voltage; similar observations were also reported compression that lasted for around 300 ns [156]. The second spike with FWHM at around 60 ns was observed near the maximum compression. Its duration was equal to the pinch lifetime of the plasma focus according to the high-voltage signal. Therefore, the second spike was ascribed to the electron emission from the pinch column itself. The third spike (or subsequent spikes) occurred after the maximum compression. The electron responsible for the manifestation of this spike was caused by the turbulent plasma after the disintegration of the pinch column.

For a shot at a pressure of 1.7 mbar and electron beam velocity of 4.6×10^7 m/s, the electron beam energy is calculated using the time-of-flight technique from the top part of the hollow anode to the electron collector plate. The calculated average energy of the energetic electron beam is 500 keV at the optimum Argon gas pressure of 1.7 mbar. Therefore, the emissions from the energetic electron beam in the low energy plasma focus device are significant and caused by instabilities.

To study the low energy plasma focus device as an electron beam source, we explored the parameters that are dependent on the filling pressure of Argon gas. Given the dependence of the average electron beam charge, density, and energy with the filling pressure, electron beam signals are recorded from 0.7 mbar to 2.0 mbar.

Figure 4.19 and Figure 4.20 show the variations in the charge and density of the electron beam with the filling pressure of Argon gas, respectively.

The charge and density of the electron beam are pressure dependent and respectively reached their maxima of 0.31 μC and $13.5 \times 10^{16} / \text{m}^3$ at the optimum pressure of 1.7 mbar. The charge and density of the electron beam are high in the pressure range of 1.5 – 2.0 mbar of Argon gas.

At the optimum pressure, the device favors the appropriate discharge dynamics to form a strong pinching [157]. The pinching time occurs near the maximum discharge current, thereby transferring the maximum energy into the plasma. As a result, the emissions of the electron beam are optimal at this pressure, and the maximum average charge, density, and energy of electron beam are achieved. Below the optimum pressure, the beam emission decreased because of the unstable dynamics of the current sheath at low gas pressures. Increasing the Argon pressure beyond the optimum value decreased the velocity of the current sheath because of the increased sheath mass. Therefore, the focus formation weakened and low electron beam emission was produced.

University of Malaya

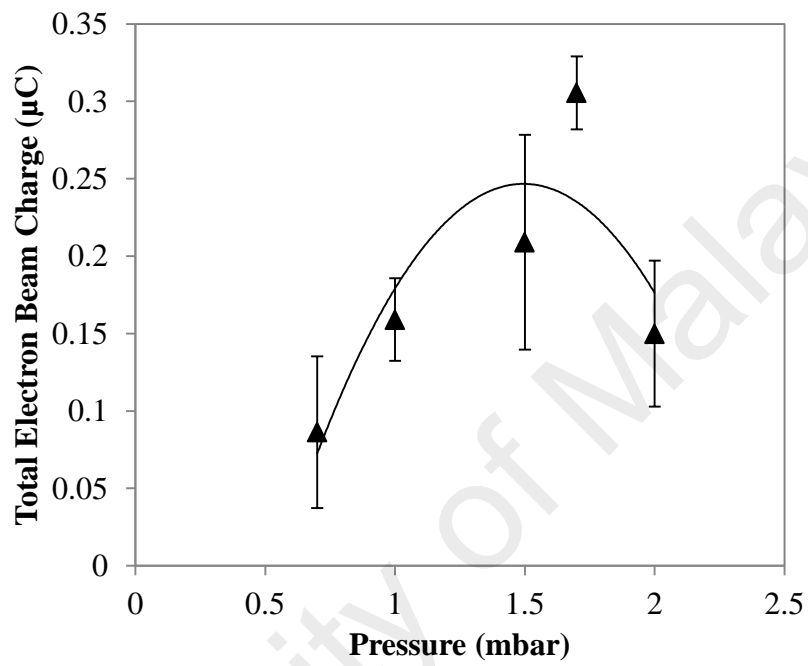


Figure 4.19: Variation of total electron beam charge versus Argon gas pressure.

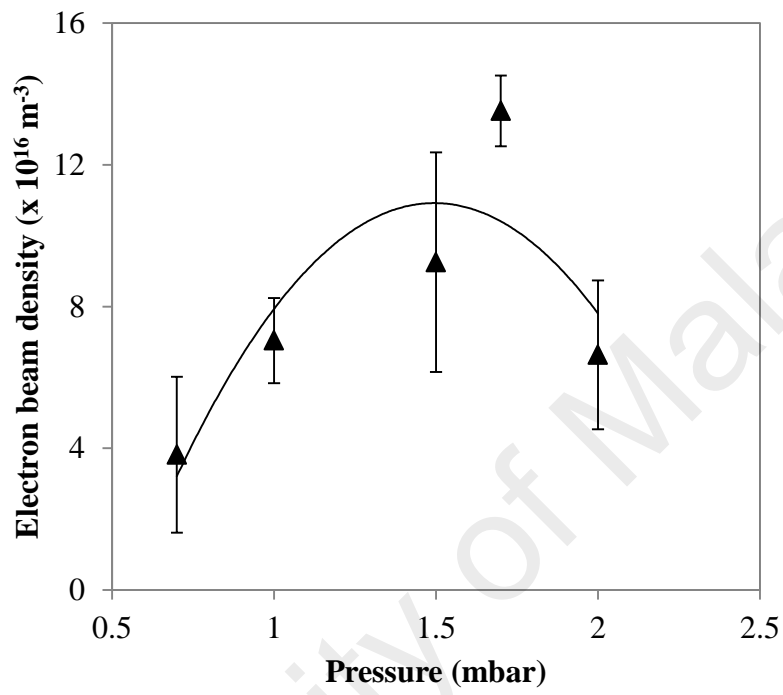


Figure 4.20: Variation of electron beam density versus Argon gas pressure.

4.6 Plasma Focus Model (Radiative) - Lee Model

Plasma Focus Model has been developed for Mather-type Plasma Focus devices, for the energy of 3 kJ plasma focus device (known as UNU/ICTP PFF). There is no limit to optimized electrode configuration and energy storage in order to keep within efficient ranges, for instance, of graph plotting.

There are various applications of this model, for example, estimation of SXR yield [5] for developing radiation source, the design of plasma focus [4] and in recent times, neutron scaling laws [8] and an experimental technique [9] to compute pinch current from a measured discharge current waveform.

This model combines the electrical circuit with plasma focus dynamics, thermodynamics, and radiation, facilitating a realistic simulation of all untreated focus properties. The model was successfully used to assist several projects, for example, radiation coupled dynamics in the five-phase code, numerical experiments on radiation [5]. A new development is addition of the neutron yield Y_n using a beam-target mechanism [20-24], resulting in realistic Y_n scaling with I_{pinch} [20,21]. The description, theory, code, and a broad range of results of this model are available online for download [5].

The two-phase Lee model was described in 1984 [158] and is used to assist in the design and interpret several experiments, [159]. This model was extensively used as a complementary facility in several machines, such as UNU/ICTP PFF, NX2, and NX1 [160]. The information obtained from the model included the axial and radial velocities, dynamics [160-162] as well as the characteristics and yield of soft X-ray (SXR) emissions [105]. A detailed description of the Lee Model is already available on the internet [163]. Numerical experiments were carried out on the UM-DPF2 machine given the available and reliable current traces.

Our machine parameters were used in the theoretical model to determine the results of the radiation (X-ray) emissions and the magnitude of electron emissions from the UM-DPF2 device as well as to compare these findings with those experimentally obtained for Ar pressures between 1.5 mbar and 2.0 mbar.

Figure 4.21 shows the comparison of the computed total current trace (pink, smooth line) with the experimental counterpart (blue, dotted line) of the UM-DPF2 at an operating voltage of 12 kV and an Ar pressure of 1.70 mbar (1.27 Torr). The outer radii b , inner radii a , and anode length z_0 were 3.2 cm, 1.9 cm, and 18 cm, respectively

In the numerical experiments, the external or static inductance $L_0 = 165$ nH and the stray resistance $r_0 = 14$ m Ω were numerically fitted with the model parameters, namely, mass factor $f_m = 0.017$, current factor $f_c = 0.7$, and radial mass factor $f_{mr} = 0.18$. The computed current traces were in agreement with those experimentally determined.

The numerical simulations were considered satisfactory when the computed current traces matched the experimentally obtained current rise profile and peak current, time position of the current dip, slope, and the absolute value of the dip at 1.7 mbar (1.27 Torr). The fitting and actual results presented the dynamics, properties of pinch energy distributions and yields. Figures 4.22(a) and 4.22(b) illustrate the results for UM-DPF2 at an optimized Ar pressure 1.7 mbar.

4.6.1 X-ray yield with the Lee Model

The X-ray yield has been enhanced by changing experimental parameters, such as bank energy [164], discharge current, electrode configuration [105, 165], insulator material and dimensions [165], and gas composition and filling gas pressure [50]. Thus, SXR energies have been investigated in PF research because of their applications in material science [27, 166-171].

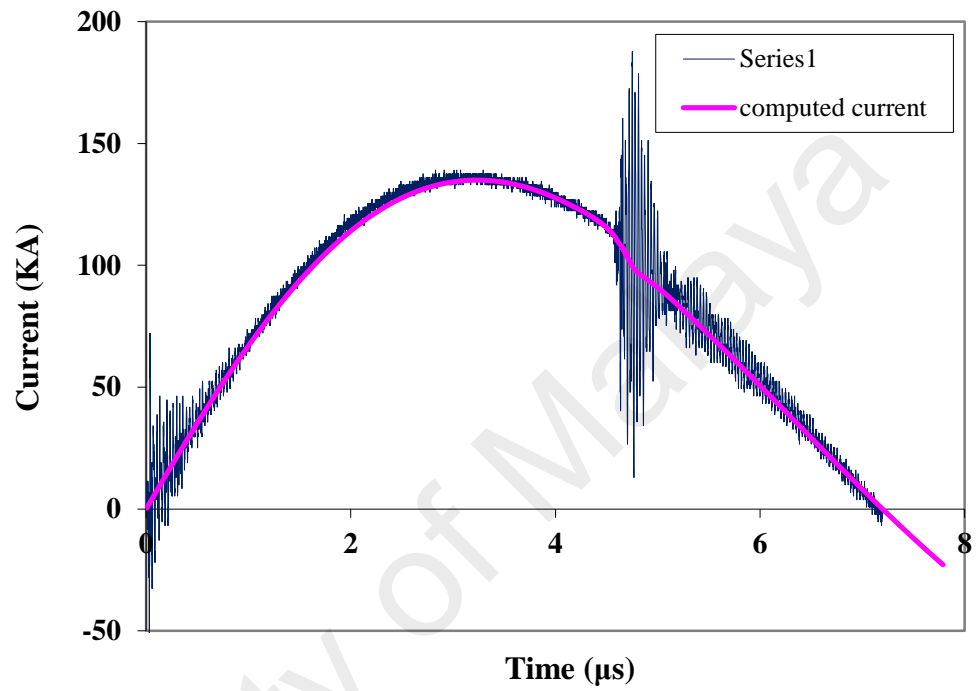
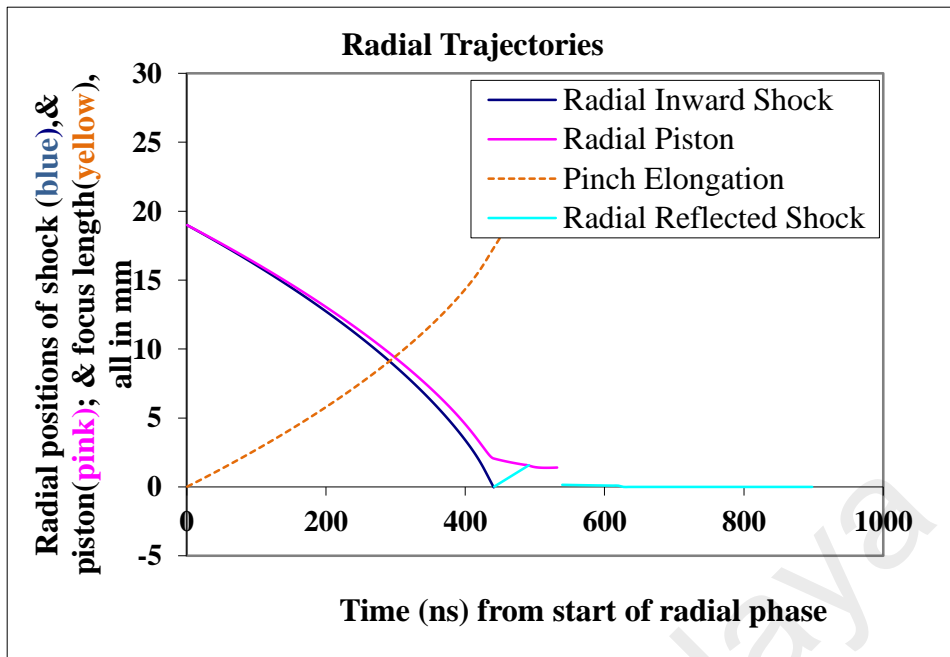
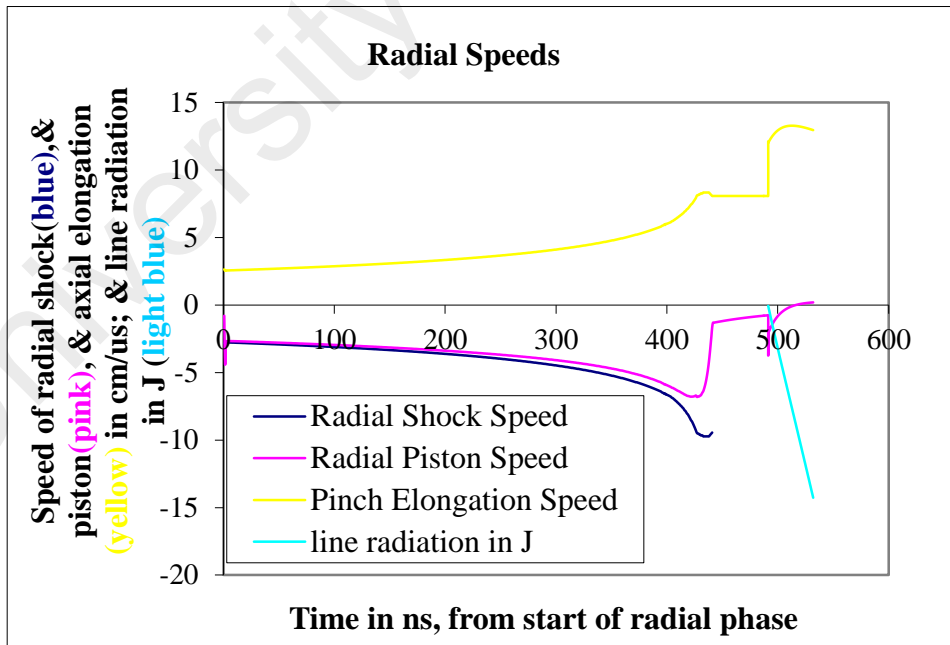


Figure 4.21: Current output at 1.70 mbar (1.27 Torr) with 12 kV measured (dashed line (blue line)) vs computed (smooth line (pink line)) current traces.



(a) UM-DPF2 in 1.27 Torr (1.7 mbar) Argon Radial trajectories of inward shock and reflected shock, inward piston. The dotted line represents the axial elongation of the imploding column.



(b) Radial speeds.

Figure 4.22: Some results of output of code at the end of the fitting process.

The code for the Lee model [163] computes the actual parameters for the focus pinch parameters and the absolute values of SXR yield Y_{sxr} ; these values are consistent with those experimentally measured. For example, the experimental, pressure-dependent Y_{sxr} computed in the NX2 machine [123] was in good agreement with that measured [163, 172]; this result indicated the accuracy of the code in obtaining realistic results for Y_{sxr} . Y_{sxr} was systematically and numerically determined at optimized conditions of the Ar gas-operated UM-DPF2 machine. The Lee model was also utilized to characterize the UM-DPF2 device operated with Ar gas and plasma focus parameters (Table 3.1 and Table 3.2).

The computed total discharge current waveform was fitted to the measured counterpart for the plasma focus device by varying the model parameters f_m , f_c , f_{mr} , and f_{cr} one by one until the computed waveform is in agreement with that measured. The fitted values of the model parameters were used to characterize and optimization the plasma focus via SXR at various pressures [173].

The code for the Lee model (RADPF5.15FIB) was configured to operate as the UM-DPF2 starting with the bank and tube parameters.

The following parameters were used to obtain a reasonably good fit;

Bank parameters: $L_0 = 165 \text{ nH}$, $C_0 = 30 \text{ }\mu\text{F}$, $r_0 = 14 \text{ m}\Omega$,

Tube parameters: $b = 3.2 \text{ cm}$, $a = 1.9 \text{ cm}$, $z_0 = 18 \text{ cm}$,

Operating parameters: $V_0 = 12 \text{ kV}$, $p_0 = 1.27 \text{ Torr}$ (1.7 mbar), Argon gas,

Fitted model parameters: $f_m = 0.017$, $f_c = 0.7$, $f_{mr} = 0.16$ and $f_{cr} = 0.7$.

The computed total current trace is in reasonable agreement with the experimental trace given the experimental parameters (Figure 4.21). The fitted values of

the model parameters were then used to solve for all the discharges at pressures ranging from 0.7 mbar to 2.5 mbar. The results showed that Y_{sxr} increased with pressure, reached its maximum within the pressure range of 1.5 – 2.0 mbar, and decreased thereafter. The code for the Lee model was used to characterize the UM-DPF2.

Figure 4.23 reveals that the maximum measured and computed (via the Lee model) Y_{sxr} are respectively 0.0025 and 0.0020 J at an Ar pressure of 1.7 mbar. These values were within the Ar pressure range of 1.5–2.0 mbar. The computed Y_{sxr} was in agreement with the measured yield within the same pressure range. Akel and Lee [174] demonstrated that Y_{sxr} slightly increased with increasing pressure, reached a maximum value of 0.002 J at 1.7 mbar (1.27 Torr), and decreased thereafter.

4.6.2 The Electron Beam Fluence Determined by the Lee Model Code

A detailed description of the Lee model is available on the internet[163]. The ion fluence is generated by the inductive plasma diode action and is given as follows [175]:

$$J_b \tau = C_n I_{pinch}^2 z_p \frac{\ln\left(\frac{b}{r_p}\right)}{\left(\pi r_p^2 U^2\right)} \text{ ions } m^{-2} \quad (4.3)$$

Equation 4.3 is used to calculate the number of ions per square meter exiting the pinch in each plasma focus shot. Hence, the ion beam number fluence is derived from the beam–plasma target considerations as follows:

$$F_{ib} \tau = C_n I_{pinch}^2 z_p \frac{\ln\left(\frac{b}{r_p}\right)}{\left(\pi r_p^2 U^2\right)} \text{ ions } m^{-2} \quad (4.4)$$

Where, $C_n = 8.5 \times 10^8$; (All SI units) is a constant which was calibrated from a graphical presentation of all available measured Y_n data.

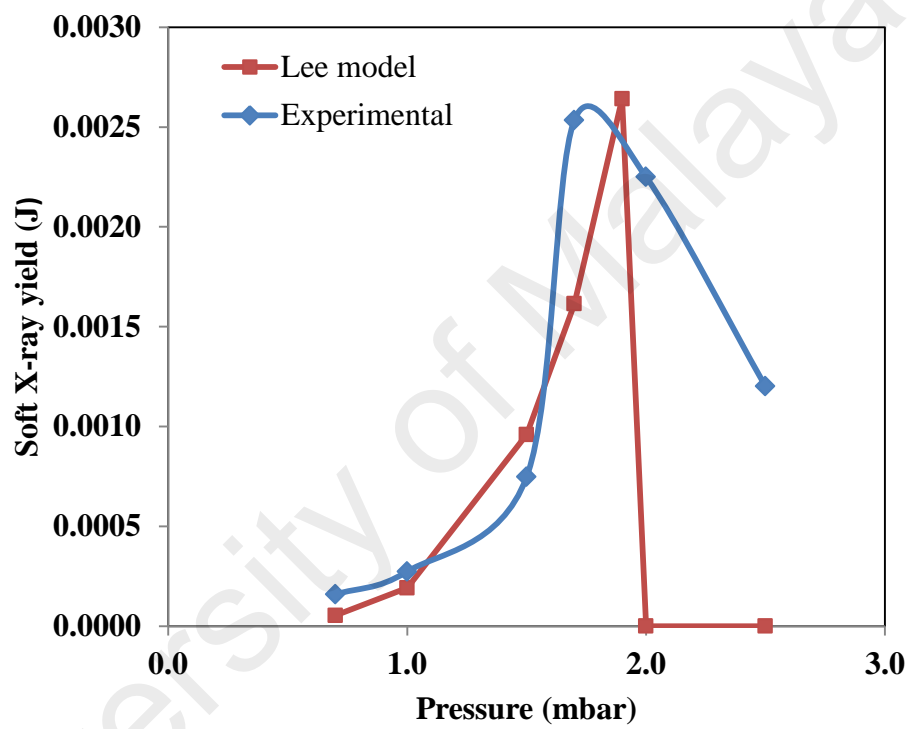


Figure 4.23: Experimental and computed (via the Lee model) Y_{sxr} yield of X-ray emission as functions of the pressure from the Ar-operated UM-DPF2.

I_{pinch} = Pinch current

z_p = Pinch length

b = outer electrode, cathode radius

r_p = Pinch radius

U = beam energy in eV where in this model

$U = n V_{max}$ (max. dynamic induced voltage).

During the calibration process, numerical experiments against the experimental data by using $U = n V_{max}$ with n varied from 1 to 5. The best fit of computed yield against experimental yield was found when $n = 3$.

The plasma focus properties were computed using the Lee model code to determine the fluence for each shot. The electron beam fluence ($F_{eb}\tau$), was assumed to be generated by the action of the inductive plasma diode prior to its computation via the Lee model.

The electron beam fluence ($F_{eb}\tau$) from the UM-DPF2 device can be determined by using the following equation 4.5, as follow:

$$F_{eb}\tau = C_n I_{pinch}^2 z_p \frac{\ln\left(\frac{b}{r_p}\right)}{\left(\pi r_p^2 U^{\frac{1}{2}}\right)} \text{ electrons} / m^2 \quad (4.5)$$

$$F_{eb}\tau = 4.1 \times 10^{19} \frac{\text{electron}}{m^2}$$

Furthermore, the electron beam axially traversed the pinch; the attenuation of the beam was attributed to the interaction with the hot dense plasma. However, the proportion of the electrons that underwent interactions was small; most of the electrons passed through and exited the pinch.

The results revealed that about 4.1×10^{19} electrons / m² exited the pinch for each UM-DPF2 shot. The number of ions and electrons were assumed to be equal.

Figure 4.24 represents the measured (UM-DPF2) and computed (Lee model code) numbers of electrons per shot for pressures ranging from 0.7 mbar to 2.0 mbar in an Ar plasma focus. In the measured results, the number of electrons per shot increased with the pressure, reached a maximum of 1.9×10^{14} /shot at the optimum Ar pressure of 1.7 mbar, and decreased thereafter. The number of electrons per shot in the computed results also increased with Ar pressure (0.7 mbar to 1.0 mbar) and decreased after the optimum value was reached.

The results implied that the number of electron per shot from the UM-DPF2 system and that from the Lee model for a pressure range of 1.5–2.0 mbar were in good agreement. At low pressures (< 1.0 mbar), the number of electrons per shot was low because of the weak current sheet, which failed to provide full support to yield a strong pinch column and produce electron emissions. For pressures higher than 2.0 mbar, the number of electrons per shot was also low because the velocity of the current sheet was impeded by massive particles and the focus information was delayed; hence, the magnitude of electron emission was low. The maximum number of electrons per shot was obtained for Ar gas pressures between 1.5 and 2.0 mbar. The computed results via the Lee model indicated that the number of electrons per shot was also obtained at the same pressure range. Hence, the measured and computed numbers of electrons per shot were in good agreement.

Figure 4.25 shows the plot of the total electron fluence against the pressure of Ar gas that ranges between 0.7 mbar and 2.0 mbar for an Ar plasma focus.

In the measured results, the total electron fluence increased with Ar pressures up to 1.7 mbar; the maximum total electron fluence at 1.7 mbar was found to be

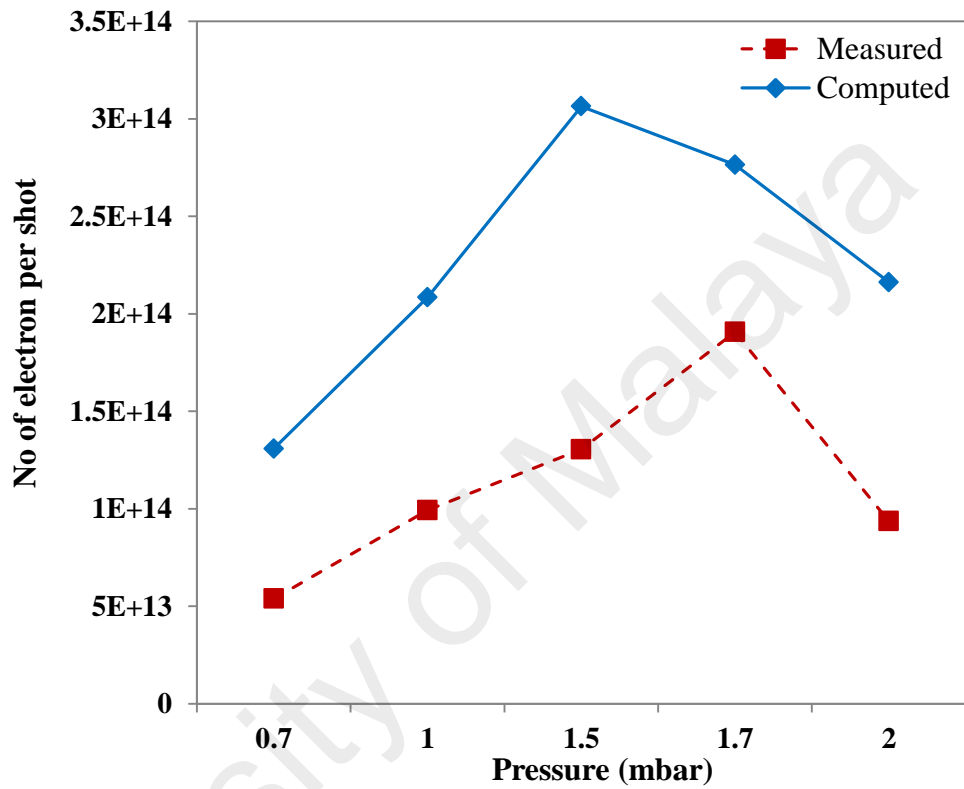


Figure 4.24: Measured and computed number of electron per shot as a function of the pressure from Argon UM-DPF2.

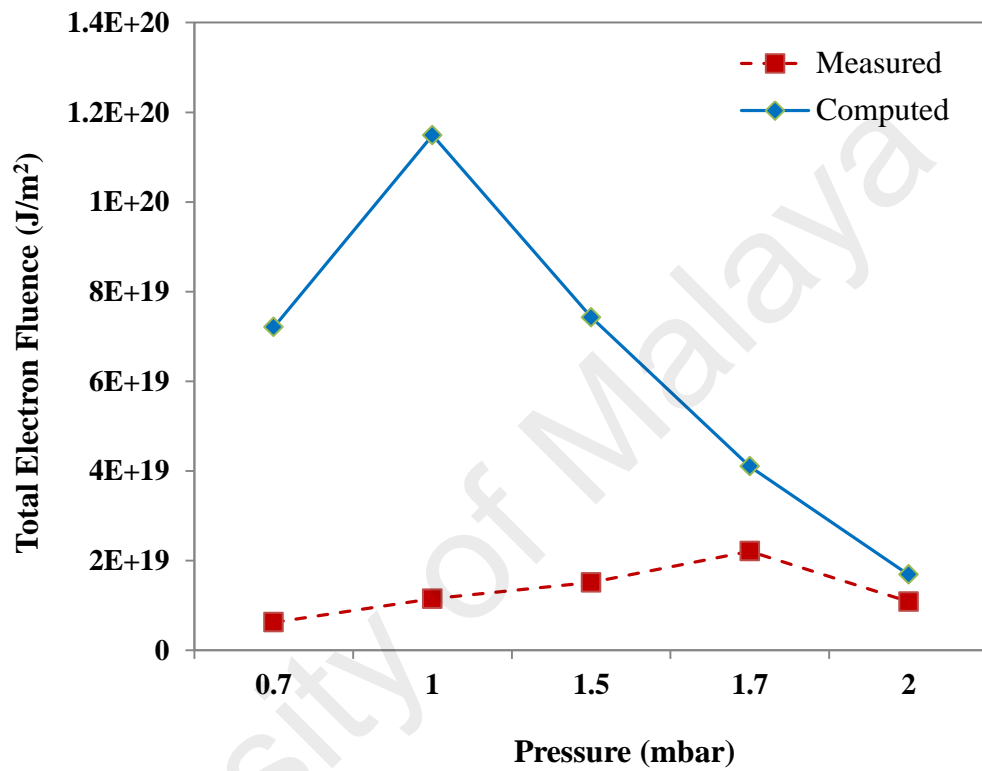


Figure 4.25: Total electron fluence J / m^2 as a function of the pressure from Argon UM-DPF2.

$2.21 \times 10^{19} \text{ J / m}^2$ of Ar gas. Subsequently, the fluence decreased for pressures higher than the optimized value.

In the computed results, the total electron fluence also increased with Ar pressure that ranged from 0.7 mbar to 1.0 mbar. Furthermore, the total electron fluence per m^2 decreased with increasing pressure (> 1.0 mbar). The maximum total electron fluence was $1.14 \times 10^{20} \text{ J / m}^2$ at an Ar pressure of 1.0 mbar.

The total electron fluence values from the system and the Lee model was in good agreement for pressures ranging from 1.5 mbar to 2.0 mbar. At 1.0 mbar, the total electron fluence value with computed yield was higher than that measured yield at 1.5–2.0 mbar because of the ideal environment. In experiments, the electron beam emission was in downward direction and numbers of factors effects on the electron beam emission in the device. Thus, the maximum total electron fluence was obtained for Ar pressures between 1.5 mbar and 2.0 mbar. In the computed (via the Lee model) results, the maximum number of electrons per shot was observed for Ar pressures ranging from 1.5 mbar to 2.0 mbar. The results revealed that the measured and computed total electron fluence were both obtained for Ar pressures between 1.5 and 2.0 mbar.

CHAPTER 5

CONCLUSIONS AND SUGGESTIONS FOR FUTURE WORKS

5.1 Conclusions

The main goal of our project was to conduct an in-depth investigation on the electron beam emission from the UM-DPF2 device within a specific pressure range, as well as on the X-ray emission in the same pressure range. A large number of experiments were carried out using a compact 2.2 kJ low energy plasma focus operated in argon. The charging voltage was 12 kV and the operating pressure was in the range of 0.7–2.5 mbar.

In our UM-DPF2 device, the maximum total X-ray yields were 77 mJ, 47 mJ, and 42 mJ at 1.7 mbar argon gas pressure using pairs of Al foils with respective thicknesses of 20 μm and 100 μm ; 30 μm and 100 μm ; and 40 μm and 100 μm ; respectively. The X-ray yield decreased for pressures higher or lower than the optimum argon pressure. The X-ray yield was high at 1.5–2.0 mbar argon pressure range. The estimated high electron temperature was 7 keV at 1.7 mbar optimum pressure of working argon gas and 12 kV constant voltage.

X-ray line spectrum of the target (lead, copper, and indium) was detected using the spectrometer at 0.7–2.0 mbar Ar pressure. The notable X-ray line spectra of lead ($\text{Pb-L}_{\alpha 2}$), copper, and indium materials were detected at 1.7 mbar Ar pressure. The results were in good agreement with the presence of an energetic electron beam at 1.7 mbar pressure to detect the X-ray line spectrum from the plasma focus region in low energy plasma focus device. Spectrometric results supported the energetic electron

beam emission from the focus region because of instabilities upon collision with the target material. The flux of the electron beam significantly affected the material.

PMT-scintillator was used to observe the radiation emissions including the electron beam from the plasma focus. The average radiation X-ray intensity caused by the electron beam was obtained between 1.0 mbar and 2.0 mbar. The radiation intensity increased at this pressure range because of the bombardment of the electron beam from the plasma focus on the target. The maximum total radiation intensity was recorded at 1.7 mbar.

Faraday cup was used in combination with a photodiode to conclude the electron beam emission from the plasma focus device. The electron beam signals were recorded at 0.7–2.0 mbar. The charge and density of the electron beam were high in the pressure range of 1.5–2.0 mbar of argon gas. The charge and density of the electron beam were $0.31 \mu\text{C}$ and $13.5 \times 10^{16} / \text{m}^3$, respectively at the optimum pressure of 1.7 mbar.

The Lee model (RADPF5.15FIB) was used to compare the results of electron beam emission in the pressure range of 1.5–2.0 mbar of argon gas in the plasma focus device.

The measured maximum soft X-ray yield (Y_{sxr}) was 0.0025 J at 1.7 mbar Ar gas pressure, whereas the computed maximum Y_{sxr} was 0.0020 J at 1.7 mbar pressure. The maximum Y_{sxr} was present at 1.5–2.0 mbar Ar gas pressure range. The computed Y_{sxr} agreed very well with the measured yield within the same pressure range.

The measured and computed results of the number of electrons /shot at 0.7–2.0 mbar pressure range in argon plasma focus were compared. The maximum measured and computed yield of the number of electrons /shot was obtained 1.9×10^{14} /shot and 3.1×10^{14} /shot, respectively at the optimum pressure of 1.7 mbar of Ar gas. The

comparison of the measured and computed yield of numbers of electrons /shot was in the range of 1.5–2.0 mbar pressure of Ar gas, which was a good agreement this pressure range of Ar gas.

The total electron fluence (energy) versus the Ar gas pressure was at 0.7–2.0 mbar pressure range of argon plasma focus. The maximum measured and computed yield of the total electron fluence was obtained $2.21 \times 10^{19} \text{ J / m}^2$ and $1.14 \times 10^{20} \text{ J / m}^2$, respectively at 0.7–2.0 mbar pressure range of argon plasma focus. The total electron fluence from the system and Lee code at 1.5–2.0 mbar pressure range were in good agreement in the UM-DPF2 device.

The investigation is extremely important not only for academic studies but can also serve as a foundation for future direct applications of the electron beam emitted from the low energy plasma focus devices.

5.2 Suggestions for Future Works

Plasma focus devices are alternative electron beam sources. Production of electron yield from the plasma focus when argon gas is used can be enhanced through beam-target fusion. Intense electron beam emission from the plasma focus can be utilized for this purpose.

Studies to enhance electron beam emission using longer electrodes have been suggested [144]. In the current project, the optimum pressure with argon filling was investigated; hence, operation with nitrogen, neon, and their mixtures can be studied in the future.

To improve current understanding about the electron beam production mechanism, the electron beam, X-ray, and ion beam should be investigated

simultaneously in relation to voltage and current signals. Imaging of the plasma focus to identify the zone where the electron beams are emitted can also provide meaningful results.

The XR100T cadmium zinc telluride (CZT) spectrometer can be used to measure the energy spectrum of the electron beams for high-Z material targets in the plasma focus device. This spectrometer has the advantages of increasing the efficiency and detecting electron beam energy up to the MeV range.

Our studies proved that the plasma focus device is a unique source of electron beam emission, and future work is necessary to determine their important dependency parameters by comparing different machines. Once general scaling laws are identified as suitable for such devices, the electron emission can be further optimized in terms of efficiency, spectrum, current, charge, and so on, in the same way that the original fusion design was modified for conversion to powerful X-ray sources.

Several directions for further studies can be easily identified using the same or another set of diagnostics. An experiment can be designed to solve some of the questions raised in our findings. Simultaneous measurement of ion and electron current and spectra, on-axis and off-axis, with the corresponding X-ray measurements in different energy ranges, as well as the interactions inside the beam can also be better understood.

The studies can be further expanded by employing other working gases by modifying the capacitive pulser and/or the focus tube and by using other sets of operating parameters (charging voltage, inductance, and capacitance) or design parameters (electrode and insulator dimensions).

Future studies can also explore the direct use of the electrons emitted by plasma focus for scientific and medical applications. Although different groups have tried to use these electron beams, for instance, for electron lithography, these attempts have been rare and unsystematic. Several possible application fields, such as thin-film deposition, surface coating, medical applications (for instance, cancer treatment), and others can be identified. For medical applications, the energy range is very important to tune up for the specific energy that should be good in the treatment of the cancer cells in the medical application and save the time span of human life by using the low energy plasma focus device as a source of the electron beam. It will be a great source for cancer cell treatment in present medical sciences. For this purpose, more resources are needed to continue the project to optimize the controlled specific energy range of the low energy plasma focus device.

Theoretical explanation and numerical simulation of the plasma processes and mechanisms involved in the initial stage of current sheath breakdown to the final pinch and the plasma turbulence and instabilities are also needed. Simultaneous measurement of different parameters and properties of the plasma, as well as various types of emissions, can be employed. Through these approaches, better correlations between parameters can be deduced, and the various theoretical approaches and hypotheses can be well verified.

The current trend in plasma focus research is moving toward its industrial uses as numerous publications have been related to the electron beam and radiation application. Thus, parametric control of the electron beam and radiation source is sometimes more important than a fundamental understanding of their mechanisms. However, the effects of the electron beam and radiation on targets deserve a systematic investigation by means of simulation and experimentation. Given that the plasma

processes are highly dynamic, problems related to the reliability of using the plasma focus device should be addressed. Interdisciplinary collaboration, especially with professionals from material science, optics and laser, biomedical and engineering domains, can motivate the progress and improve the feasibility of using the plasma focus device as an electron beam energy source for future applications.

As this thesis has explicitly shown, low energy plasma focus device, as an electron beam source, offers a wide research opportunity for both academic studies and future applications in numerous fields.

University of Malaysia

REFERENCES

1. Mather, J., *15. Dense Plasma Focus*. Methods in Experimental Physics, 1971. **9**: p. 187-249.
2. Mather, J., *Investigation of the High-Energy Acceleration Mode in the Coaxial Gun*. Physics of Fluids, 1964. **7**(11): p. S28-S34.
3. Filippov, N., T. Filippova, and V. Vinogradov, *Dense high-temperature plasma in a non-cylindrical Z-pinch compression*. Nucl. Fusion, Suppl., 1962. **8**: p. 577.
4. Artsimovich, L., *Controlled Thermonuclear Reactions (Gordon and Breach, New York, 1964)*. Chap. III , Vol. 150, p. 203.
5. Komel'Kov, V., T. Morozova, and U. Skvortsov. *The investigation of a powerful electric discharge in deuterium*. in *Plasma Physics and the Problem of Controlled Thermonuclear Reactions, Volume 2*. 1959.
6. Soto, L., et al., *Filamentary structures in dense plasma focus: Current filaments or vortex filaments?* Physics of Plasmas, 2014. **21**(7): p. 072702.
7. Moreno, J., et al., *Neutron energy distribution and temporal correlations with hard x-ray emission from a hundreds of joules plasma focus device*. Plasma Physics and Controlled Fusion, 2015. **57**(3): p. 035008.
8. Pavez, C., et al., *Observation of plasma jets in a table top plasma focus discharge*. Physics of Plasmas, 2015. **22**(4): p. 040705.
9. Ceccolini, E., et al., *EBT2 Dosimetry of X-rays produced by the electron beam from PFMA-3, a Plasma Focus for medical applications*. arXiv preprint arXiv:1112.2198 2011.
10. Tonks, L., *Theory of magnetic effects in the plasma of an arc*. Physical Review, 1939. **56**(4): p. 360.
11. Filippov, N., T. Filippova, and V. Vinogradov, *Nucl. Fusion, Suppl. Pt. 2,(1962) 577;* Phys. Fluids, 1962.

12. Soto, L., et al., *Studies on scalability and scaling laws for the plasma focus: similarities and differences in devices from 1 MJ to 0.1 J* This paper was presented as an invited talk at the 29th International Conference on Phenomena in Ionized Gases (ICPIG XXIX) held in Cancun, Mexico on 12–17 July 2009. See stacks.iop.org/PSST/19/3. Plasma Sources Science and Technology, 2010. **19**(5): p. 055017.
13. Soto, L., et al., *Nanofocus: an ultra-miniature dense pinch plasma focus device with submillimetric anode operating at 0.1 J*. Plasma Sources Science and Technology, 2008. **18**(1): p. 015007.
14. Silva, P., et al., *Neutron emission from a fast plasma focus of 400 joules*. Applied physics letters, 2003. **83**(16): p. 3269-3271.
15. Soto, L., et al., *Demonstration of neutron production in a table-top pinch plasma focus device operating at only tens of joules*. Journal of Physics D: Applied Physics, 2008. **41**(20): p. 205215.
16. Silva, P., et al., *A plasma focus driven by a capacitor bank of tens of joules*. Review of scientific instruments, 2002. **73**(7): p. 2583-2587.
17. Milanese, M., R. Moroso, and J. Pouzo, *DD neutron yield in the 125 J dense plasma focus Nanofocus*. The European Physical Journal D-Atomic, Molecular, Optical and Plasma Physics, 2003. **27**(1): p. 77-81.
18. Decker, G. and R. Wienecke, *Plasma focus devices*. Physica B+ C, 1976. **82**(1): p. 155-164.
19. Moreno, C., et al., *Industrial applications of plasma focus radiation*. Brazilian Journal of Physics, 2002. **32**(1): p. 20-25.
20. Bora, B. and L. Soto, *Influence of finite geometrical asymmetry of the electrodes in capacitively coupled radio frequency plasma*. Physics of Plasmas, 2014. **21**(8): p. 083509.
21. Lee, S., et al., *A simple facility for the teaching of plasma dynamics and plasma nuclear fusion*. American Journal of Physics, 1988. **56**(1): p. 62-68.
22. Browne, P., *Acceleration in the plasma focus and in astrophysics*. Laser and Particle Beams, 1988. **6**(03): p. 409-420.

23. Stygar, W., et al., *Particle beams generated by a 6–12.5 kJ dense plasma focus*. Nuclear Fusion, 1982. **22**(9): p. 1161.
24. Neff, W., et al. *The Plasma Focus as Soft X-ray Source for Microscopy and Lithography*. in *1989 Intl Congress on Optical Science and Engineering*. 1989. International Society for Optics and Photonics.
25. Tartari, A., et al., *Improvement of calibration assessment for gold fast-neutron activation analysis using plasma focus devices*. Measurement Science and Technology, 2002. **13**(6): p. 939.
26. Benzi, V., et al., *Feasibility analysis of a Plasma Focus neutron source for BNCT treatment of transplanted human liver*. Nuclear Instruments and Methods in Physics Research Section B: Beam Interactions with Materials and Atoms, 2004. **213**: p. 611-615.
27. Gribkov, V.A., et al., *Operation of NX2 dense plasma focus device with argon filling as a possible radiation source for micro-machining*. Plasma Science, IEEE Transactions on, 2002. **30**(3): p. 1331-1338.
28. Castillo-Mejía, F., et al., *Small plasma focus studied as a source of hard X-ray*. Plasma Science, IEEE Transactions on, 2001. **29**(6): p. 921-926.
29. Nayak, B., et al., *Surface nitriding of graphite substrate by plasma focus device towards synthesis of carbon nitride coating*. Surface and Coatings Technology, 2001. **145**(1): p. 8-15.
30. Rawat, R., et al., *Room temperature deposition of titanium carbide thin films using dense plasma focus device*. Surface and Coatings Technology, 2001. **138**(2): p. 159-165.
31. Bortolotti, A., et al., *Inspection of extended objects with fast neutrons: numerical tests*. Nuclear Instruments and Methods in Physics Research Section B: Beam Interactions with Materials and Atoms, 1992. **63**(4): p. 473-476.
32. Kato, Y. and S. Be, *Generation of soft x rays using a rare gas-hydrogen plasma focus and its application to x-ray lithography*. Applied physics letters, 1986. **48**(11): p. 686-688.
33. Feder, R., et al., *Flash X-ray microscopy with a gas jet plasma source*. Journal of microscopy, 1984. **135**(3): p. 347-351.

34. Martínez, J.F., R. Llovera, and A. Tartaglione, *Ultrafast x-ray introspective imaging of metallic objects using a plasma focus*. *Nukleonika*, 2001. **46**(1): p. S33-S34.
35. Cicuttin, A., et al., *Experimental results on the irradiation of nuclear fusion relevant materials at the dense plasma focus 'Bora' device*. *Nuclear Fusion*, 2015. **55**(6): p. 063037.
36. Inestrosa-Izurieta, M., E. Ramos-Moore, and L. Soto, *Morphological and structural effects on tungsten targets produced by fusion plasma pulses from a table top plasma focus*. *Nuclear Fusion*, 2015. **55**(9): p. 093011.
37. Wang, Z., et al. *Application of ion beam and electron beam by plasma focus device to material processing*. in *High Power Particle Beams (BEAMS), 2008 17th International Conference on*. 2008. IEEE.
38. Roberts, D., *Calculated X-ray continuous spectra of Tokamak plasmas*. *Plasma Physics*, 1982. **24**(4): p. 419.
39. Bernhardt, K. and K. Wieseemann, *X-ray bremsstrahlung measurements on an ECR-discharge in a magnetic mirror*. *Plasma Physics*, 1982. **24**(8): p. 867.
40. Reynolds, S.P., *Microphysics of shock acceleration from observations of X-ray synchrotron emission from supernova remnants*. *Advances in Space Research*, 2004. **33**(4): p. 461-465.
41. Griem, H., A. Kolb, and W. Faust, *Bremsstrahlung from dense plasmas*. *Physical Review Letters*, 1959. **2**(7): p. 281.
42. Shelkovenko, T., et al., *Electron-beam-generated x rays from X pinches*. *Physics of Plasmas*, 2005. **12**(3): p. 033102.
43. Ohzu, A. and K. Ito, *Characteristics of hard x-ray emission from laser-induced vacuum spark discharges*. *Journal of applied physics*, 2003. **93**(12): p. 9477-9482.
44. Bernstein, M.J., D.A. Meskan, and H. Van Paassen, *Space, time, and energy distributions of neutrons and x rays from a focused plasma discharge*. *Physics of Fluids*, 1969. **12**(10): p. 2193-2202.

45. Harries, W., J. Lee, and D. McFarland, *Space and time resolved emission of hard X-rays from a plasma focus*. Plasma Physics, 1978. **20**: p. 963-969.
46. Zakaullah, M., et al., *Effects of anode shape on plasma focus operation with argon*. Plasma Sources Science and Technology, 1996. **5**(3): p. 544.
47. Zakaullah, M., et al., *Influence of magnetic probe presence on current sheath dynamics in plasma focus operation*. Fusion engineering and design, 1997. **36**(4): p. 437-446.
48. Zakaullah, M., et al., *Correlation study of ion, electron and X-ray emission from argon focus plasma*. Physica Scripta, 1998. **57**(1): p. 136.
49. Ng, C.M., S.P. Moo, and C. San Wong, *Variation of soft X-ray emission with gas pressure in a plasma focus*. Plasma Science, IEEE Transactions on, 1998. **26**(4): p. 1146-1153.
50. Beg, F., et al., *Study of x-ray emission from a table top plasma focus and its application as an x-ray backlighter*. Journal of Applied Physics, 2000. **88**(6): p. 3225-3230.
51. Bland, S., et al., *Extreme ultraviolet imaging of wire array z-pinch experiments*. Review of scientific instruments, 2004. **75**(10): p. 3941-3943.
52. Ivanenkov, G., et al., *Microexplosion of a hot point in an X-pinch constriction*. Plasma Physics Reports, 2000. **26**(10): p. 868-874.
53. Edlen, B. and A. Ericson, *Hydrogen-like Spectra of Lithium and Beryllium in the Extreme Ultra-violet*. Nature, 1930. **125**: p. 233-234.
54. Ekefors, E., *Das Bogenspektrum von Stickstoff*. Zeitschrift für Physik, 1930. **63**(7-8): p. 437-443.
55. Händel, S. and I. Sundström, *X-radiation from a flash X-ray discharge column*. Zeitschrift für Physik, 1965. **186**(3): p. 271-276.
56. Cohen, L., et al., *Study of the x rays produced by a vacuum spark*. JOSA, 1968. **58**(6): p. 843-846.

57. Lee, T., *Solar-flare and laboratory plasma phenomena*. The Astrophysical Journal, 1974. **190**: p. 467-479.
58. Hebach, M., et al., *Absolute measurements of the soft X-ray emission from vacuum spark discharges*. Plasma Sources Science and Technology, 1993. **2**(4): p. 296.
59. Fukai, J. and E. Clothiaux, *Mechanism for the Hard—X-Ray Emission in Vacuum Spark Discharges*. Physical Review Letters, 1975. **34**(14): p. 863.
60. Anton, M., et al., *X-ray tomography on the TCV tokamak*. Plasma physics and controlled fusion, 1996. **38**(11): p. 1849.
61. Tartari, A., et al., *Energy spectra measurements of X-ray emission from electron interaction in a dense plasma focus device*. Nuclear Instruments and Methods in Physics Research Section B: Beam Interactions with Materials and Atoms, 2004. **213**: p. 206-209.
62. Choi, P., et al., *Characterization of self-generated intense electron beams in a plasma focus*. Laser and Particle Beams, 1990. **8**(03): p. 469-476.
63. Favre, M., et al., *X-ray emission in a small plasma focus operating with H₂-Ar mixtures*. Plasma Sources Science and Technology, 1992. **1**(2): p. 122.
64. Wong, C.S., et al., *Dynamics of x-ray emission from a small plasma focus*. Malaysian J. Sci, 1996. **17**: p. 109.
65. Serban, A., et al. *Time-resolved Electron Beam and X-ray Emission from a Neon Plasma Focus*. in *27th EPS Conference on Contr. Fusion and Plasma Phys. ECA B*. 2000.
66. Zakauallah, M., et al., *Efficiency of plasma focus for argon K-series line radiation emission*. Plasma Sources Science and Technology, 2000. **9**(4): p. 592.
67. Pouzo, J., et al., *Relativistic electron beams detection in a dense plasma focus*. The European Physical Journal D-Atomic, Molecular, Optical and Plasma Physics, 2002. **21**(1): p. 97-100.
68. Grusdev, V., et al., *Universal plasma electron source*. Vacuum, 2005. **77**(4): p. 399-405.

69. Jakubowski, L. and M. Sadowski, *Measurements of pulsed electron beams emitted from plasma-focus devices*. Problems of Atomic Science. & Technology No. 1, Series: Plasma Physics 10 (2005) 89, 2005. **91**.
70. Neog, N. and S. Mohanty, *Study on electron beam emission from a low energy plasma focus device*. Physics Letters A, 2007. **361**(4): p. 377-381.
71. Neog, N., S. Mohanty, and T. Borthakur, *Time resolved studies on X-rays and charged particles emission from a low energy plasma focus device*. Physics Letters A, 2008. **372**(13): p. 2294-2299.
72. Harries, W.L., J.H. Lee, and D.R. McFarland, *Trajectories of high energy electrons in a plasma focus*. Plasma physics, 1978. **20**(2): p. 95.
73. Nardi, V., et al., *Proceedings of the IAEA Conference on Plasma Physics and Controlled Nuclear Fusion Research, Innsbruck, 1978*. 1979.
74. Piitran, A.C., *Electron and medium energy X-ray emission from a dense plasma focus*. 2002, Ph.D Thesis, National Institute of Education.
75. Choi, P., et al., *Absolute timing of a relativistic electron beam in a plasma focus*. Physics Letters A, 1988. **128**(1): p. 80-83.
76. Lee, P., et al., *Electron lithography using a compact plasma focus*. Plasma Sources Science and Technology, 1997. **6**(3): p. 343.
77. Patran, A., et al., *Spectral study of the electron beam emitted from a 3 kJ plasma focus*. Plasma Sources Science and Technology, 2005. **14**(3): p. 549.
78. Amiraslanov, I., et al., *An X-ray structural study of the complexes of p-aminobenzoic acid with metals*. Journal of Structural Chemistry, 1980. **21**(5): p. 653-658.
79. Mather, J.W., *Formation of a High-Density Deuterium Plasma Focus*. Physics of Fluids, 1965. **8**(2): p. 366-377.
80. Filippov, N., T. Filippova, and V. Vinogradov, *Dense high-temperature plasma in a non-cylindrical z-pinch compression*. Nucl. Fusion, Suppl., 1962. **8**: p. 577

81. Decker, G., W. Kies, and G. Pross, *Experiments solving the polarity riddle of the plasma focus*. Physics Letters A, 1982. **89**(8): p. 393-396.
82. Soto, L., et al., *Characterization of the axial plasma shock in a table top plasma focus after the pinch and its possible application to testing materials for fusion reactors*. Physics of Plasmas, 2014. **21**(12): p. 122703.
83. Auluck, S., *Re-appraisal and extension of the Gratton-Vargas two-dimensional analytical snowplow model of plasma focus. II. Looking at the singularity*. Physics of Plasmas, 2015. **22**(11): p. 112509.
84. Donges, A., et al., *The breakdown phase in a coaxial plasma gun*. Physics Letters A, 1980. **76**(5): p. 391-392.
85. Bruzzone, H. and R. Vieytes, *The initial phase in plasma focus devices*. Plasma physics and controlled fusion, 1993. **35**(12): p. 1745.
86. Nowikowski, J., et al. *Dependence of interelectrode insulating system shape on the PF parameters and experimental verification of 2D snow plow code*. in *9th European conference on controlled fusion and plasma physics, Oxford, 17-21 September 1979*. 1979.
87. Shyam, A. and R. Rout, *Effect of anode and insulator materials on Plasma Focus sheath (pinch) current*. Plasma Science, IEEE Transactions on, 1997. **25**(5): p. 1166-1168.
88. Krompholz, H., et al., *Formation of the plasma layer in a plasma focus device*. Physics Letters A, 1980. **77**(4): p. 246-248.
89. Kies, W., *Power limits for dynamical pinch discharges*. Plasma physics and controlled fusion, 1986. **28**(11): p. 1645.
90. Beg, F.N., et al., *Effect of insulator sleeve material on neutron emission from a plasma focus*. Physica scripta, 1992. **46**(2): p. 152.
91. Zakaullah, M., et al., *Influence of insulator contamination by copper evaporation on neutron yield in a low-energy plasma focus*. Plasma physics and controlled fusion, 1993. **35**(6): p. 689.
92. Bernard, A., et al., *Experimental studies of the plasma focus and evidence for nonthermal processes*. Physics of Fluids, 1975. **18**(2): p. 180-194.

93. Bruzzone, H., et al., *Experimental results of a low energy plasma focus*, in *Energy storage, compression, and switching*. 1976, Springer. p. 255-258.
94. Krompholz, H., et al., *A scaling law for plasma focus devices*. *Physics Letters A*, 1981. **82**(2): p. 82-84.
95. Bostick, W., et al. *Strong turbulence and shock in a plasma coaxial accelerator*. in *Phenomena in Ionized Gases, Tenth International Conference*. 1971.
96. Mather, J., *Methods of Experimental Physics/Ed. by H. Griem and R. Lovberg*. New York: Academic, 1971. **9**.
97. Lee, S., *An energy-consistent snow-plough model for pinch design*. *Journal of Physics D: Applied Physics*, 1983. **16**(12): p. 2463.
98. Tou, T., S. Lee, and K. Kwek, *Nonperturbing plasma-focus measurements in the run-down phase*. *Plasma Science, IEEE Transactions on*, 1989. **17**(2): p. 311-315.
99. Chen, Y. and S. Lee, *Coaxial plasma gun in mode 1 operation†*. *International Journal of Electronics*, 1973. **35**(3): p. 341-352.
100. Bruzzone, H., H. Kelly, and C. Moreno, *The effect of transmission lines and switching action on the electrical signals in a powerful capacitive discharge*. *Plasma Science, IEEE Transactions on*, 1990. **18**(4): p. 689-694.
101. Toepfer, A., D. Smith, and E. Beckner, *Ion heating in the dense plasma focus*. *Physics of Fluids*, 1971. **14**(1): p. 52-61.
102. Schmit, J. and K. Creath, *Extended averaging technique for derivation of error-compensating algorithms in phase-shifting interferometry*. *Applied Optics*, 1995. **34**(19): p. 3610-3619.
103. Lee, P. and A. Serban, *Dimensions and lifetime of the plasma focus pinch*. *Plasma Science, IEEE Transactions on*, 1996. **24**(3): p. 1101-1105.
104. Clause, A., L. Soto, and A. Tarifeno-Saldivia, *Influence of the Anode Length on the Neutron Emission of a 50 J Plasma Focus: Modeling and Experiment*. *Plasma Science, IEEE Transactions on*, 2015. **43**(2): p. 629-636.

105. Bhuyan, H., et al., *Comparative study of soft x-ray emission characteristics in a low energy dense plasma focus device*. Journal of applied physics, 2004. **95**(6): p. 2975-2981.
106. Bernstein, M., C. Lee, and F. Hai, *Time Correlations of X-Ray Spectra with Neutron Emission from a Plasma-Focus Discharge*. Physical Review Letters, 1971. **27**(13): p. 844.
107. Gullickson, R. and R. Barlett. *X-ray analysis for electron beam enhancement in the plasma focus device*. in *Presented at 23d Ann. Conf. on Appl. of X-ray Analysis, Denver, 7 Aug. 1974*.
108. Johnson, D.J., *Study of the x-ray production mechanism of a dense plasma focus*. Journal of Applied Physics, 1974. **45**(3): p. 1147-1153.
109. Bernstein, M.J., *Acceleration Mechanism for Neutron Production in Plasma Focus and z-Pinch Discharges*. Physics of Fluids, 1970. **13**(11): p. 2858-2866.
110. Gribkov, V., et al., *Plasma dynamics in PF-1000 device under full-scale energy storage: I. Pinch dynamics, shock-wave diffraction, and inertial electrode*. Journal of Physics D: Applied Physics, 2007. **40**(7): p. 1977.
111. Patran, A.C., *Electron and medium energy X-ray emission from a dense plasma focus*. 2002, Ph.D Thesis.
112. Peacock, N., M. Hobby, and P. Morgan. *Measurements of the Plasma Confinement and Ion Energy in the Dense Plasma Focus*. in *Plasma Physics and Controlled Nuclear Fusion Research 1971. Vol. I. Proceedings of the Fourth International Conference on Plasma Physics and Controlled Nuclear Fusion Research*. 1971.
113. Smith, J.R., et al., *Operation of a plasma focus device as a compact electron accelerator*. Physics of Fluids, 1985. **28**(7): p. 2305-2307.
114. Krauz, V., R. Salukvadze, and E. Khautiev, *Energy spectra of ion beams formed in plasma focus*. 1985.
115. Filippov, N., T. Filippova, and V. Vinogradov, *Nucl. Fusion, Suppl. Pt. 2,(1962) 577;* Phys. Fluids, 1965. **8**: p. 366.

116. Gribkov, V., S. Isakov, and A. Romanov, *On harmonics of epithermal infrared radiation of a plasma focus*. 1984.
117. Gribkov, V., *Energy Storage, Compression, and Switching* ed W Bostik et al. 1976, New York: Plenum.
118. Decker, G., et al., *Plasma layers of fast focus discharges-schlieren pictures experimentally taken and computer simulated*. *Plasma physics and controlled fusion*, 1985. **27**(5): p. 609.
119. Lee, S., *Energy balance and the radius of electromagnetically pinched plasma columns*. *Plasma Physics*, 1983. **25**(5): p. 571.
120. Liu, M. and S. Lee. in *1998 ICPP and 25th EPS Conf. on Fusion and Plasma Physics, Praha, 29 June-3 July. ECA 1998*.
121. Lee, S., *Laser and Plasma Technology*, edited by S. Lee, BC Tan, CS Wong, and AC Chew. World Scientific, Singapore, 1985. **37**: p. 64.
122. Spitzer, L., *Physics of fully ionized gases*. 1956: Intersci Pub. LTD., London
123. Lee, S., et al., *High rep rate high performance plasma focus as a powerful radiation source*. *Plasma Science, IEEE Transactions on*, 1998. **26**(4): p. 1119-1126.
124. Früngel, F.B., *High Speed Pulse Technology: Voltage measuring with voltage divider*. Vol. 2. 1965: Academic Press.
125. Huddleston, R.H. and S.L. Leonard, *Plasma Diagnostic Techniques (Academic, New York, 1965)*. 1965: p. 14.
126. Lee, S., et al., *Singapore J. Phys*, 1984. **1**: p. 75.
127. Serban, A., *Anode geometry and focus characteristics*. 1995, Ph.D Thesis, Nanyang Technological University.
128. Rogowski, W. and W. Steinhaus, *Measuring the magnetomotive force*. *Arch, für Elek*, 1912. **13**: p. 141.

129. Hutchinson, I.H., *Principles of plasma diagnostics*. 2 ed. 2002: Cambridge university press.
130. Van Paassen, H.L.L., *A time-resolved ross filter system for measuring x-ray spectra in z-pinch plasma focus devices*. *Review of Scientific Instruments*, 1971. **42**(12): p. 1823-1824.
131. Siegbahn, K., *Alpha-Beta and Gamma-Ray Spectroscopy*, ed. K. Siegbahn. Vol. 1. 1965, Amsterdam: North-Holland Publishing Company.
132. Ross, P., *A new method of spectroscopy for faint x-radiations*. *J. Opt. Soc. Am*, 1928. **16**(6): p. 433-436.
133. Kirkpatrick, P., *On the theory and use of Ross filters*. *Review of Scientific Instruments*, 1939. **10**(6): p. 186-191.
134. Kirkpatrick, P., *Theory and use of Ross filters. II*. *Review of Scientific Instruments*, 1944. **15**(9): p. 223-229.
135. Donaldson, T., *Theory of foil-absorption techniques for plasma X-ray continuum measurements*. *Plasma Physics*, 1978. **20**(12): p. 1279.
136. Corallo, D., D. Creek, and G. Murray, *The X-ray calibration of silicon pin diodes between 1.5 and 17.4 keV*. *Journal of Physics E: Scientific Instruments*, 1980. **13**(6): p. 623.
137. Victoreen, J.A., *The Calculation of X-Ray Mass Absorption Coefficients*. *Journal of Applied Physics*, 1949. **20**(12): p. 1141-1147.
138. Henke, B.L., R. White, and B. Lundberg, *Semiempirical Determination of Mass Absorption Coefficients for the 5 to 50 Angstrom X-Ray Region*. *Journal of Applied Physics*, 1957. **28**(1): p. 98-105.
139. Hirano, K., et al., *A time-resolved soft X-ray camera system with rapid data processing and its application to a pinched-plasma experiment*. *Japanese journal of applied physics*, 1990. **29**(4R): p. 779.
140. Zakaullah, M., et al., *Low-energy plasma focus as a tailored x-ray source*. *Journal of fusion energy*, 2000. **19**(2): p. 143-157.

141. Zakaullah, M., et al., *Comparative study of ion, x-ray and neutron emission in a low energy plasma focus*. Plasma Sources Science and Technology, 1998. **7**(2): p. 206.
142. Burkhalter, P., et al., *Quantitative x-ray emission from a DPF device*. Review of scientific instruments, 1992. **63**(10): p. 5052-5055.
143. Sadowski, M., et al., *Filamentary structure of the pinch column in plasma focus discharges*. Physics Letters A, 1984. **105**(3): p. 117-123.
144. Khan, M.Z., S.L. Yap, and C.S. Wong, *The impact of plasma interference profile (PIP) on argon discharge in plasma focus device*. International Journal of Physical Sciences, 2013. **8**(8): p. 286-294.
145. Khan, M.Z., et al., *Effect of cathode designs on radiation emission of compact diode (CD) device*. Journal of Fusion Energy, 2013. **32**(1): p. 34-41.
146. Khan, M.Z., S.L. Yap, and C.S. Wong, *Estimation of electron temperature and radiation emission of a low energy (2.2 kJ) plasma focus device*. Indian Journal of Physics, 2014. **88**(1): p. 97-102.
147. Jeffery, A. and T. Taniuti, *Magnetohydrodynamic Stability and Thermonuclear Confinement*, in Academic Press, New York. 1996.
148. Kondoh, Y. and K. Hirano, *Numerical study of an ion acceleration in az-pinch type plasma focus*. Physics of Fluids, 1978. **21**(9): p. 1617-1622.
149. Gary, S.P., *Ion acceleration in a plasma focus*. Physics of Fluids, 1974. **17**(11): p. 2135-2137.
150. Van Paassen, H., R. Vandre, and R.S. White, *X-Ray Spectra from Dense Plasma Focus Devices*. Physics of Fluids, 1970. **13**(10): p. 2606-2612.
151. Herold, H., et al., *Progress in plasma focus operation up to 500 kJ bank energy*. Plasma Physics and Controlled Nuclear Fusion Research 1988 Vol. 2, 1988: p. 587.
152. Beckner, E., E. Clothiaux, and D. Smith, *Dominant source of soft X radiation from coaxial discharge tubes*. Physics of Fluids, 1969. **12**(1): p. 253-254.

153. Tartari, A., et al., *Feasibility of X-ray interstitial radiosurgery based on plasma focus device*. Nuclear Instruments and Methods in Physics Research Section B: Beam Interactions with Materials and Atoms, 2004. **213**: p. 607-610.
154. Mohanty, S.R., et al., *Development of multi faraday cup assembly for ion beam measurements from a low energy plasma focus device*. Japanese journal of applied physics, 2005. **44**(7R): p. 5199.
155. Karkari, S., S. Mukherjee, and P. John, *Properties of a differential pressure pseudospark device*. Review of Scientific Instruments, 2000. **71**(1): p. 93-99.
156. Sadowska, E., et al. *High Temp. Mat. in Proc. 6 No. 1, (2002) 23*.
157. Bhuyan, H., et al., *Magnetic probe measurements of current sheet dynamics in a coaxial plasma accelerator*. Measurement Science and Technology, 2003. **14**(10): p. 1769.
158. Pearlman, J. and J. Riordan, *X-ray lithography using a pulsed plasma source*. Journal of Vacuum Science and Technology, 1981. **19**(4): p. 1190-1193.
159. Porter, J., et al., *Demonstration of population inversion by resonant photopumping in a neon gas cell irradiated by a sodium Z pinch*. Physical review letters, 1992. **68**(6): p. 796.
160. Hammer, D., et al., *X-pinch soft x-ray source for microlithography*. Applied physics letters, 1990. **57**(20): p. 2083-2085.
161. Zakaullah, M., et al., *Imaging of fusion reaction zone in plasma focus*. Physics of Plasmas, 1999. **6**(8): p. 3188-3193.
162. Zakaullah, M., et al., *Enhanced copper K-alpha radiation from a low-energy plasma focus*. Applied Physics Letters, 2001. **78**(7): p. 877-879.
163. Lee, S., *Radiative dense plasma focus computation package: RADPF*. See <http://www.intimal.edu.my/school/fas/UFLF/File1RADPF.htm>, <http://www.plasmafocus.net/IPFS/modelpackage/File1RADPF.htm>, 2011.
164. Lee, S., et al., *Numerical experiments on plasma focus neon soft x-ray scaling*. Plasma Physics and Controlled Fusion, 2009. **51**(10): p. 105013.
165. Zakaullah, M., et al., *Characteristics of X-rays from plasma focus operated with neon gas*. Plasma Sources Science and Technology, 2002. **11**: p. 377-382.

166. Zakauallah, M., et al., *Scope of plasma focus with argon as a soft X-ray source*. Plasma Science, IEEE Transactions on, 2002. **30**(6): p. 2089-2094.
167. Wong, D., et al., *Soft X-ray optimization studies on a dense plasma focus device operated in neon and argon in repetitive mode*. Plasma Science, IEEE Transactions on, 2004. **32**(6): p. 2227-2235.
168. Neog, N., S. Mohanty, and E. Hotta, *Anode length optimization in a modified plasma focus device for optimal x-ray yields*. Journal of applied physics, 2006. **99**(1): p. 013302.
169. Roomi, A., et al., *The Effect of Applied Voltage and Operating Pressure on Emitted X-Ray from Nitrogen (N₂) Gas in APF Plasma Focus Device*. Journal of fusion energy, 2011. **30**(5): p. 413-420.
170. Rico, L., et al., *Crystallization of amorphous zirconium thin film using ion implantation by a plasma focus of 1kJ*. Applied Surface Science, 2007. **254**(1): p. 193-196.
171. Rico, L., et al., *Oxygen ion implantation in Strontium Bismuth Tantalate thin films*. Brazilian journal of physics, 2006. **36**(3B): p. 1009-1012.
172. Lee, S., et al., *Soft x-ray yield from NX₂ plasma focus*. Journal of Applied Physics, 2009. **106**(2): p. 023309.
173. Al-Hawat, S., et al., *Model parameters versus gas pressure in two different plasma focus devices operated in argon and neon*. Journal of fusion energy, 2012. **31**(1): p. 13-20.
174. Akel, M. and S. Lee, *Practical optimization of AECS PF-2 plasma focus device for argon soft X-ray operation*. Journal of fusion energy, 2012. **31**(2): p. 122-129.
175. Lee, S. and S. Saw, *Plasma focus ion beam fluence and flux—scaling with stored energy*. Physics of Plasmas, 2012. **19**(11): p. 112703.

APPENDIX

LIST OF PUBLICATIONS AND CONFERENCE PAPERS PRESENTED

LIST OF PUBLICATIONS

- Paper 1:** Khan, M. Z., Yap, S. L., Yaqoob, I., Naresh, K. N., Lim, L. K., & Wong, C. S. (2014). Low-Energy Plasma Focus Device as an Electron Beam Source. *The Scientific World Journal*, 2014.
- Paper 2:** Khan, M. Z., Yap, S. L., & Wong, C. S. (2014). Estimation of electron temperature and radiation emission of a low energy (2.2 kJ) plasma focus device. *Indian Journal of Physics*, 88(1), 97-102.
- Paper 3:** Khan, M. Z., Yap, S. L., & Wong, C. S. (2014). Imperative function of electron beams in low energy plasma focus device. *Pramana: Journal of Physics*. (Accepted).
- Paper 4:** Khan, M. Z., Yap, S. L., & Wong, C. S. (2013). The impact of plasma interference profile (PIP) on argon discharge in plasma focus device. *International Journal of Physical Sciences*, 8(8), 286-294.
- Paper 5:** Khan, M. Z., Yap, S. L., Khan, M. A., & Zakaullah, M. (2013). Effect of cathode designs on radiation emission of compact diode (CD) device. *Journal of Fusion Energy*, 32(1), 34-41.
- Paper 6:** Khan, M. Z., Yap, S. L., & Wong C. S. (2013). Variation of Radiation Emission with Argon Gas Pressure in UM Plasma Focus with the Hollow Anode. *Open Journal of Applied Sciences*, 3, 194.

LIST OF CONFERENCE PAPERS

- C. Paper 1:** Khan, M. Z., Yap, S. L. & Wong, C. S. (2014, March). Study on electron beam in a low energy plasma focus. In *FRONTIERS IN PHYSICS: 4th International Meeting* (Vol. 1588, pp. 185-190). AIP Publishing.
- C. Paper 2:** Khan, M. Z., Yap, S. L., & Wong, C. S. (2014, March). Comparative study of radiation emission without and with target in a 2.2 kJ plasma focus device. In *4TH INTERNATIONAL CONFERENCE ON MATHEMATICS AND NATURAL SCIENCES (ICMNS 2012): Science for Health, Food and Sustainable Energy* (Vol. 1589, pp. 225-229). AIP Publishing.

University of Malaya